Kazimierz Peszyński
Editor

Developments in Machinery Design and Control

Vol. 4

University Press
University of Technology
and Agriculture in Bydgoszcz

Kazimierz Peszyński
Editor

Developments
in Machinery Design and Control

Vol.
4

University Press
University of Technology and Agriculture in Bydgoszcz

Editors' office address
Developments in Machinery Design and Control
University of Technology and Agriculture, Department of Control and Machinery Design
ul. Prof. S. Kaliskiego 7, 85–791 Bydgoszcz, Poland
phone *+48 52 3408238, +48,* fax *+48 52 3408245,* e-mail *kazimierz.peszynski@atr.bydgoszcz.pl*

ISBN 83-89334-82-8

University Press of University of Technology and Agriculture
Ks. A. Kordeckiego 20, 85-225 Bydgoszcz, phone +48(52) 3749482, 3749426
e-mail: wydawucz@atr.bydgoszcz.pl http://www.atr.bydgoszcz.pl/~wyd

---

1st edition. 100 copies. Author's sheets 7.1. Printed sheets 8.3. 3rd class printing paper.
Submitted and printing completed in December 2005. Order No 12/2005
Printed in: Small Typography of University of Technology and Agriculture in Bydgoszcz,
Ks. A. Kordeckiego 20

Editors note

'Development in Machinery Design and Control' is a periodical publication issued annually since 2002. Herewith we provide the reader with the fourth volume. The publication is designed as a forum for the researchers of designing in general and designing control systems in machine technology and process technology to share their scientific experience. Our journal publishes original scientific papers as well as interesting reviews of essential engineering achievements, short information on new books available and conferences held.

The publication is open for the authors mostly dealing with the problems of machinery designing, computer aided engineering, aspects of calculation and experiments in verifying the design, especially with numerical methods and verifying the design due to fatigue. There are also welcome papers on the automatic control in open and closed loop, mostly state-of-the-art plant and process modeling, computer aided control and modern technology to perform control processes.

To provide those willing to contribute a paper with more details about the profile of the publication, here are Table of Contents of the three volumes published so far.

Contents of vol. 1 (2002)

Contents of vol. 2 (2003)

Contents of vol. 3 (2004)

CONTENTS

University Press
University
of Technology
and Agriculture
in Bydgoszcz

DEVELOPMENTS IN MACHINERY DESIGN AND CONTROL
Vol. 4 (2005) 9 – 18
Scientific Journal

Mária Čarnogurská[1]
Technical University of Košice, Department of Power Engineering
Vysokoškolská 4, 042 00 Košice, Slovak Republic

MODELLING OF WIND TURBINE BLADE LOAD AT DIFFERENT WIND SPEEDS

Abstract: The results of modeling the air flow through wind-plant rotor which consists of 3 blades, are analyzed in the article. In the view of different air-flow velocities ($3 \div 20\,\mathrm{m \cdot s^{-1}}$), information about forces distribution on the blade is the results of modeling. Such information is essential for blade rigidity analysis. The conclusions concern the results of the solution of stress and deformation state of rotor blade carried out with Finite Elements Method (FEM).

Keywords: FEM, aerodynamic characteristics, blade strength calculation

NOMENCLATURE

- c_T – coefficient of axial strength of wind motor (WM), –
- c_M – coefficient of torque of WM, –
- c_P – coefficient of efficiency of WM, –
- D – diameter of rotor, m
- $\mathrm{d}Q$ – elementary tangential force in the plane of rotation for radius r, N
- $\mathrm{d}R$ – resulting elementary aerodynamic force for radius r, N
- $\mathrm{d}X$ – elementary resistance force for radius r, N
- $\mathrm{d}Y$ – elementary uplift force for radius r, N
- M – torque, $\mathrm{N \cdot m}$
- n – rotor revolutions of WM, $\mathrm{s^{-1}}$
- P – performance of the wind motor, W
- r_i – radius of computation cross-section, m
- R – resulting force acting on the rotor, N
- r – rotor radius, m
- T – axial force acting on the rotor, N
- u_0 – peripheral speed, $\mathrm{m \cdot s^{-1}}$
- V_0 – speed of air current running on the blade element, $\mathrm{m \cdot s^{-1}}$
- W_1 – resulting flowing speed of the blade element, $\mathrm{m \cdot s^{-1}}$

[1]Corresponding author. *Tel.:* 421-55-602 4359, *fax:* +421-55-602-2452
E-mail address: Maria.Carnogurska@tuke.sk (M. Čarnogurská)

w_1 – resulting induced speed, $m \cdot s^{-1}$
α – start up angle of the blade for r radius, °
β_1 – angle of air current flowing in to the given blade element, °
φ – angle of setting of a given blade cross-section to radius r, °
λ_0 – high speediness, –
ω – angular velocity, 1/s

1. INTRODUCTION

The three blade rotor of wind turbine of a diameter $D = 10$ m analyzed in this paper is designed for small wind power plants. Its part is a multi pole generator of a net electric power of approx. 15 kW. The wind turbine is designed for localities with minor wind-power potential. The assumed level of rotor axis over the ground is 30 m and the average long-term air velocity at the height of rotor axis is $V_0 = 5$ $m \cdot s^{-1}$ up to 9 $m \cdot s^{-1}$.

2. BLADE DESCRIPTION AND ROTOR OPERATION

Basic dimensions of the rotor blade are shown in Fig. 1. Blade profile depending on the radius marked as cross-section 10 is NACA 23012 that continuously transfers into profile NACA 23018 in the cross-section 3. Under each cross-section 3 to 10 in Fig. 1. indicates the angle of setting φ between the plane of rotation and profile chords in individual elementary cross-sections. For details, see Fig. 2. Besides the angle of setting, the distribution of all the elementary forces and direction of forces action, also start up angle of air-flow on blade element α and resulting flowing speed of blade element W_1 are indicated.

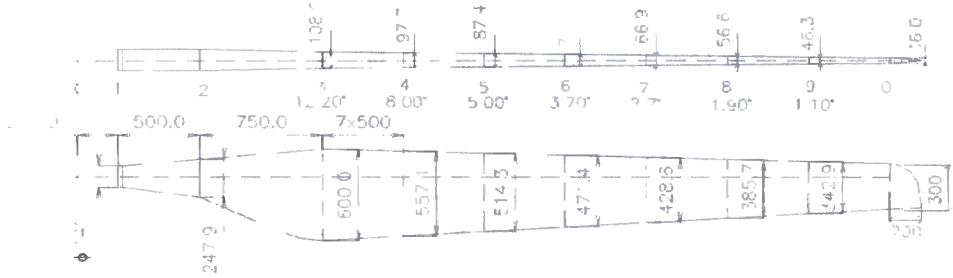

Fig. 1. Geometry of wind motor (WM) rotor blade

The limit arc of the blade exceeds the nominal radius of the propeller by about 200 mm where a transition into the symmetrical profile with a zero angle of setting φ is assumed. This position represents the working position of the blade. The parking position is characteristic by the fact that the turning of the propeller blade in the cross-section 10 is 60°.

3. ROTOR OPERATION DESCRIPTION

The active control system following wind identification $3\ m \cdot s^{-1}$ will set the blade into a working position. The blade will operate in this position in a range of immediate wind speed $V_0 = 3 m \cdot s^{-1}$ up to $9\ m \cdot s^{-1}$ with linear gain of revolutions n from 0.55 r.p.s (at the wind speed $V_0 = 3\ m \cdot s^{-1}$) to the value of 1.86 r.p.s (at wind speed $V_0 = 9 m \cdot s^{-1}$). In the working position the coefficient of axial force c_T on the propeller blade between the cross-sections 3 up to 9 will be approximately 0.75. Fig. 3 is the course of axial force coefficient c_T for various setting angles φ of the propeller blade depending on high speediness λ_0. The high speediness gives the ratio of peripheral speed u_0 at the tip of the blade to the wind velocity V_0 and is determined according to Eq. (1)

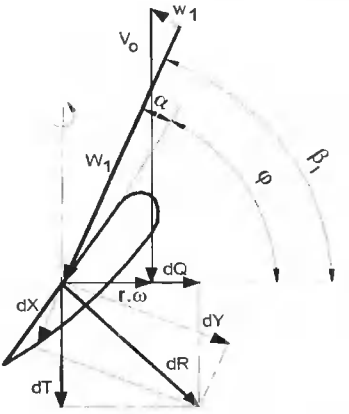

Fig. 2. Distribution of forces on the blade [1]

$$\lambda_0 = \frac{u_0}{V_0} = \frac{\pi \cdot D \cdot n}{V_0} \tag{1}$$

Peripheral speed at the height of the blade is determined according to Eq. (2)

$$u_0 = r \cdot \omega, \tag{2}$$

where

$$\omega = 2 \cdot \pi \cdot r \cdot n \tag{3}$$

This speed on the height of blade increases with the distance from the axis of rotation.

In the case of wind speed change and to reach the same high speediness, it is necessary to change rotor revolutions. The analyzed rotor has a projected high speediness $\lambda_0 = 5.75$.

Among the basic relations for the calculation of aerodynamic forces and moments of forces acting on the rotor of wind motor are relations defining power in a form [4, 5]

$$P = (1/8) \cdot c_P \cdot \rho \cdot \pi \cdot D^2 \cdot V_0^3 \tag{4}$$

for axial force

$$T = (1/8) \cdot c_T \cdot \rho \cdot \pi \cdot D^2 \cdot V_o^2 \tag{5}$$

for torque

$$M = (1/16) \cdot c_M \cdot \rho \cdot \pi \cdot D^3 \cdot V_o^2 \tag{6}$$

Following the overrun of wind speed $V_0 = 9\ \mathrm{m \cdot s^{-1}}$, the control system will increase the setting angle φ in a way to obtain about $2\,\mathrm{r.p.s}$ at $V_0 = 12\ \mathrm{m \cdot s^{-1}}$ blade revolutions and to obtain a net electric power of the blade about $15\,\mathrm{kW}$. Up to wind speed $V_0 = 20\,\mathrm{m \cdot s^{-1}}$ the propeller blade will be readjusted depending on the wind speed always in a way to make the power input to the propeller constant. Following the overrun of the wind speed of $20\ \mathrm{m/s}$ the setting angle φ at the cross-section 10 will be readjusted into the position of $60°$ and the propeller will be braked. It will be unbraked only in the case of a drop of $V_0 < 15\ \mathrm{m \cdot s^{-1}}$.

4. ANALYSIS OF BLADE LOADING

For the calculation of basic aerodynamic characteristics of rotor, Zhukovski's vortical (eddy) theory was used. By means of this theory (for the selected setting angle $\varphi = 0°$ and in the selected cross-sections – distances r_1 from the axis of rotation) the elementary coefficients of axial force and efficiency of blade dc_T and dc_P were calculated. For the calculation for a given geometry of the blade according to Fig. 1., it was required to achieve constant circulation on the blade. This requirement will not be met during the start or stop of the rotor.

The coefficient of axial force c_T, coefficient of efficiency c_P and coefficient of torque c_M, can be gained by the integration of their elementary values calculated in given cross-sections of the blade.

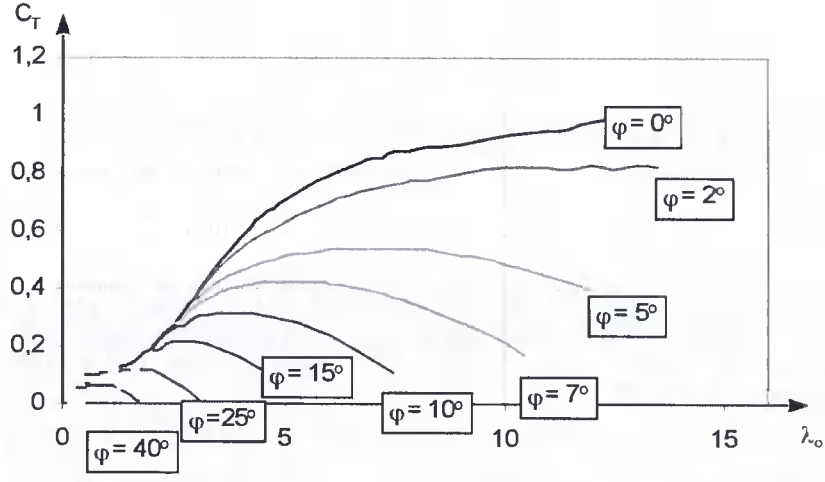

Fig. 3. Dependence of axial force coefficient on blade angle setting [2]

The processes of given coefficients are given in Figs. 3 to 5.

The resulting axial force T, rotor output P and its torque M can be gained by the multiplication of given coefficient by rotor geometric dimensions and parameters of the environment.

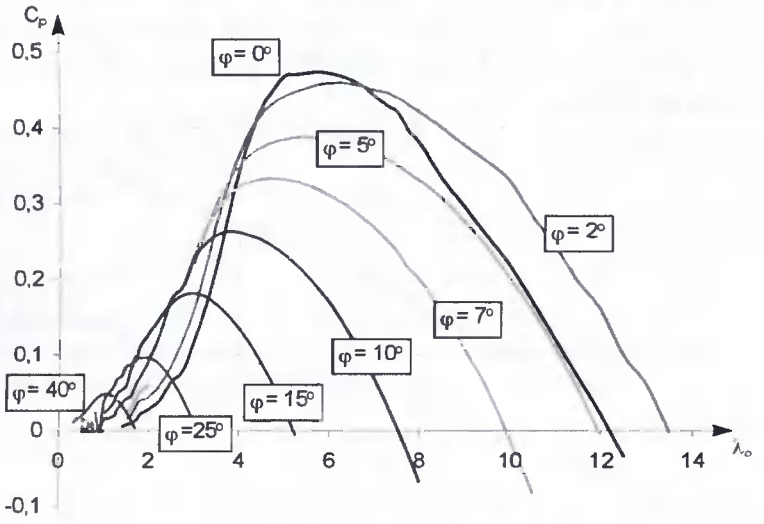

Fig. 4. Dependence of output coefficient on blade setting angle [2]

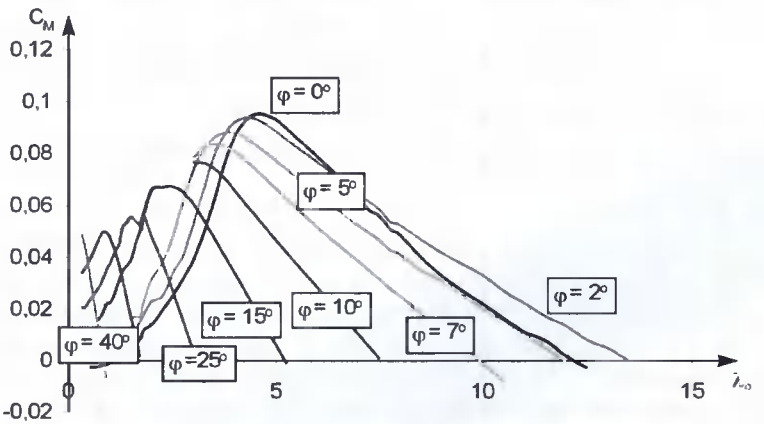

Fig. 5. Dependence of torque coefficient on blade angle setting [2]

With the help of Eq. (6), the elementary tangential force dQ was determined in all the examined distances from the axis of rotation according to Eq. (7):

$$dQ = \frac{dM}{r_i} \tag{7}$$

The elementary resulting aerodynamic force is determined in individual distances from the axis of rotation according to Eq. (8).

$$dR = \sqrt{dT^2 + dQ^2} \tag{8}$$

The resulting force R, from which there was examined the static effect on the blade, represented an integral value of elementary resulting forces dR along the blade. Its course, related to one blade of rotor depending on wind speed, is shown in Fig. 6. It is the process of resulting force which with a distance from the axis of rotation increases for all modes of rotor operation besides the mode at wind speed $20\ m \cdot s^{-1}$ when the blade is in parking position.

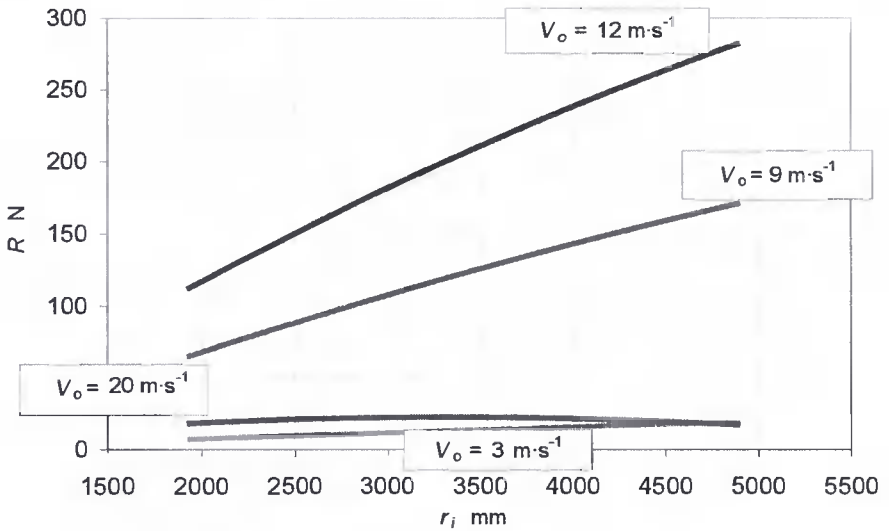

Fig. 6. Course of resulting force on the blade

The basic working position of the blade remains unchanged for wind speeds $3\ m \cdot s^{-1}$ to $9\ m \cdot s^{-1}$ and therefore the rotor blade load state was analyzed at a maximum wind speed, i.e. $9\ m \cdot s^{-1}$.

The geometric model of blade for structural analysis of stress and blade deformation at the effect of wind at speed $9\ m \cdot s^{-1}$ was created by SOLID elements with a quadratic base function. For the calculation, the *Finite Elements Method (FEM)* was applied. The method is based on the use of numerical mathematics methods. As means of interpretation, software package COSMOS/M, version 2.6 was used.

The computational model of blade is made of a final number of elements 6 610 to which a total of 12 080 node points was assigned.

Boundary conditions of solution

The boundary conditions of solution were, besides the proper pressure acting on the blade in a normal direction, assigned also with the effects of centrifugal force and gravitational acceleration.

The material properties were included into the solution separately for the metal beam (girder) and separately for the blade case and its internal reinforcement made of epoxy-fiber glass. The beam is made from material 12 021.1 for which the yield point is

$\mathrm{Re} = 235\,\mathrm{MPa}$. With the safety coefficient $n = 1.5$, the permissible strength for the metal beam $\sigma_{dov} = 157\ \mathrm{MPa}$. For epoxy-fibre glass, the permitted strength $\sigma_{dov} = 98\ \mathrm{MPa}$. The other material properties are given in Table 1.

Table 1. Material properties

Properties		Steel 12021.1	Epoxy fibre-glass	
Elasticity modulus	E MPa	$2.06 \cdot 10^5$	$0.048 \cdot 10^5$	
Poisson's number	μ	0.28	0.28	0.43
Density	ρ kg·m^{-3}	7850	1950	

For the examination of blade rigidity, its least suitable position during rotation, when the centrifugal and gravitational force have the same direction, was selected. It is a position when the tip of the blade is directed straight to the ground.

5. RESULTS OF SOLUTION AND DISCUSSION

The static load due to such forces and pressure caused at wind speed $9\,\mathrm{m \cdot s^{-1}}$ a reduced strength in the metal beam of the value of $98.807\,\mathrm{MPa}$ (Fig. 7). This strength considers the minimum value of Poisson's number for epoxy-fibre glass part of the blade $\mu = 0.28$. In the case of Poisson's number $\mu = 0.43$, the strength gained in the metal girder assumes the value of $104.8\,\mathrm{MPa}$. In the epoxy-fiber glass part of the blade, the reduced von Misses strength did not exceed the value of $30\,\mathrm{MPa}$.

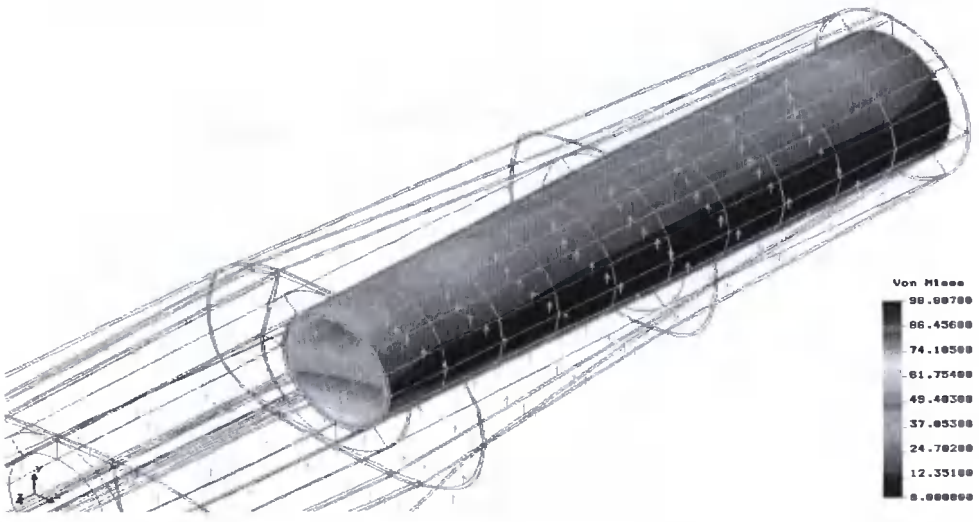

Fig. 7. Course of strength in a metal girder

In the global assessment of the blade, made from metal and epoxy-fiber glass, reduced von Misses strength represents the value of 75.57 MPa and, based on that, we can state that the blade corresponds to the load at the wind speed of $V_0 = 9\ m \cdot s^{-1}$ (Fig. 8) as for its rigidity.·

The shift of the blade tip from the plane of rotation $x - z$ reaches the value of $\delta = 651.24$ mm (Fig. 9). The proposed rotor of wind motor will thus be applicable for field installation as for wind static effects, the centrifugal force at given rotor revolutions and gravitational force.

Fig. 8. Course of strength in blade epoxy- fibreglass part

The blade has good strength tolerance in case of a possible increase in the strength against such effects as hoarfrost on the blade in winter season and partly also rotor vibration.

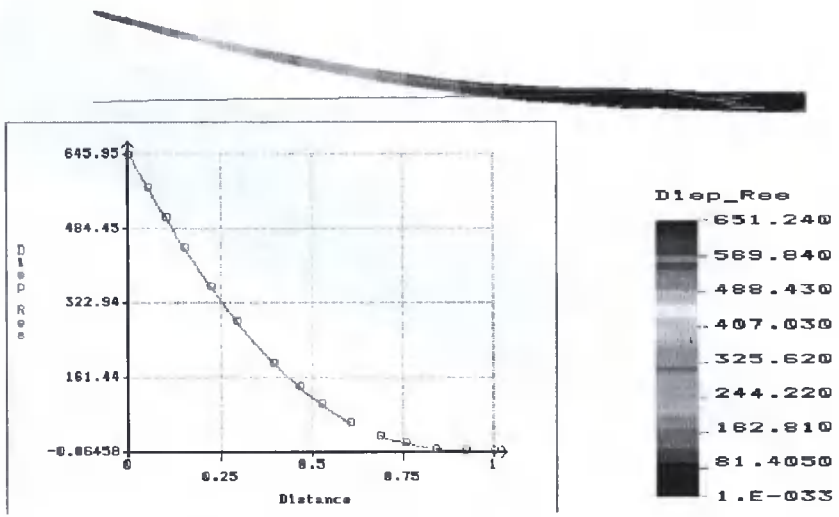

Fig. 9. Shift of the blade tip from the place of rotation *x-z*

6. SUMMARY

The results from the solution of rigidity analysis of the wind power plant rotor blade by numeric mathematical methods show an option to calculate blade load by modern computational methods, e.g. using COSMOS/M. So far no static blade computation has been made with complicated analytical procedures. Here the solutions applied were preferred rather than those which involved experimental research on reduced scale physical models. The advantage of this procedure was that it also took into account the dynamic effect of the wind. Unfortunately, there has been, so far, no equipment available in Slovakia that would be suitable for experimental research.

The results obtained using the Finite Elements Method make it possible to, in case of unfavorable results, propose a change in the blade shape and to repeat the computation. It is how we can optimize the blade shape in a way that it would be, as for its rigidity, suitable for given load conditions.

ACKNOWLEDGEMENT

The contribution was developed within the framework of grant project VEGA No. 1/9385/02.

REFERENCES

[1] Rozehnal D., 2000. Aerodynamic loading of wind motor with a horizontal rotation axis. Větrná energie 2, 13-15.

[2] Čarnogurská M., Rozehnal D., 2003. Aerodynamic characteristics of wind power plant's rotor with a blade profile of type NACA. Proc. from the 2nd conference Small water systems and alternative sources of power, DT Košice, 199-204.

[3] COSMOS/M, User's Guide, Release 2.6, California, USA.

[4] Johnson G.L., 1985. Wind energy system. Prentice-Hall, New Jersey.

[5] Le Gouriér's D., 1982. Wind power plants, theory and design. Pergamon Press Toronto-Sydney-Frankfurt.

[6] Malcho M., Jandačka J., Kapusta J., Lábaj J., 2001. Optimization of air line of ventilation shaft using the CFD method. Acta Mechanica Slovaca 3, 569.

[7] Čarnogurská M., Peszyński K., 2004. Numeryczne modelowanie naprężeń łopatki turbiny wiatrowej. Międzynarodowa konferencja procesorów energii ECO – €URO – ENERGIA, Bydgoszcz, Poland, 333-340.

Review by prof. Józef Flizikowski

University Press
University
of Technology
and Agriculture
in Bydgoszcz

DEVELOPMENTS IN MACHINERY DESIGN AND CONTROL
Vol. 4 (2005) 19 – 26
Scientific Journal

Kazimierz Dzierżek[1]
Bialystok Technical University, Department of Automatic and Robotic
Wiejska 45C, 15-351 Bialystok, Poland

BASIC PRINCIPLES OF VISUAL APPLICATIONS CREATED IN THE INTOUCH SOFTWARE

Abstract: The article presents one of the most popular program for the visualization of the industrial processes. In this article author discusses the program functions and components. Moreover, author proposes a way of creating a selected visual application.

Keywords: industrial process, control, visualization

1. INTRODUCTION

In industrial processes there is often a necessity of a permanent supervision over the process parameters and alarming in case of damage states. Such possibilities are presently provided by the programs meant to visualize industrial processes. Only a few years ago there was a number of devices which were to control the process parameters. Nowadays they are being replaced by the computer with a special program for visualization installed. Complicated and huge control sets are being replaced by the PLC controller. It is vital that an adequate software should by chosen. Similarly, the ability to program with all the specific details of the program is also essential.

2. CHARACTERISTIC FEATURES OF THE INTOUCH SOFTWARE

The InTouch software is a part of the Factory Suite industrial software by Wonderware. The Wonderware company was established in the USA in 1987. It was the first to offer a software for the industry working under control of the Microsoft Windows operational system. The application of the environment, which was not popular and common, could have turned out to be a failure. We can see now that the decision has been right. The first version of the Wonderware InTouch appeared in 1989. From the very beginning it was popular in the industry since it operated in the graphic environment just as Windows had. Therefore creating and operation of the application created in InTouch were very easy. Since 1996 Wonderware Corporation has been offering a software package for the industry FactorySuite. Presently it is the FactorySuite 2000 version which consists of the following components:
- InTouch (the software for the visualization of the industrial processes),
- Industrial SQL Server (the actual industrial data),

[1]Corresponding author. *Tel.:* +48-85-746-9233; *fax:* +48-85-746-9206
E-mail address: kazde @pb.bialystok.pl (K. Dzierżek)

– InTrack (tracing and management of the production realization),
– InBatch (elastic management of the batch processes),
– InControl (controlling the industrial processes).

Besides the above mentioned components, the FactorySuite 2000 package is equipped with the communication programs to the numerous controllers (I/O servers), Productivity Pack (the Symbol Factory library, wizards' generators, OLE connector) as well as the software for remote application tracing the actual time with the help of the Internet.

The advantage of the FactorySuite package is that the data exchange between the I/O server and InTouch is very quick since the I/O server sends and receives only the changed data (not all the data as it is in case of other visual programs).

The InTouch package has the following modules installed:

– SQL Access (which allows to exchange data),
– CPC Pro (the statistic control of the process module),
– DDE communication module (which allows to communicate with other Windows applications, e.g. allowing to create reports in Microsoft Word or Microsoft Excel),
– logging module to the file data (which writes historical data on the file),
– Web Server (which allows to publishing the InTouch applications on the Internet).

There are windows in the InTouch package which inform us about damage states, that is about exceeding of the given parameters. They are four alarm levels in the InTouch: High, Low, HiHi (very high), and LoLo (very low). There are set up separately for each variable during the variables creation on the variables. Figure 1 presents a window of defining the variables and setting the alarms. This window can also be used for setting the insensitivity level for possible interference (Deadband, or a limit of sensitivity to the changes) and activating the data logging to the file.

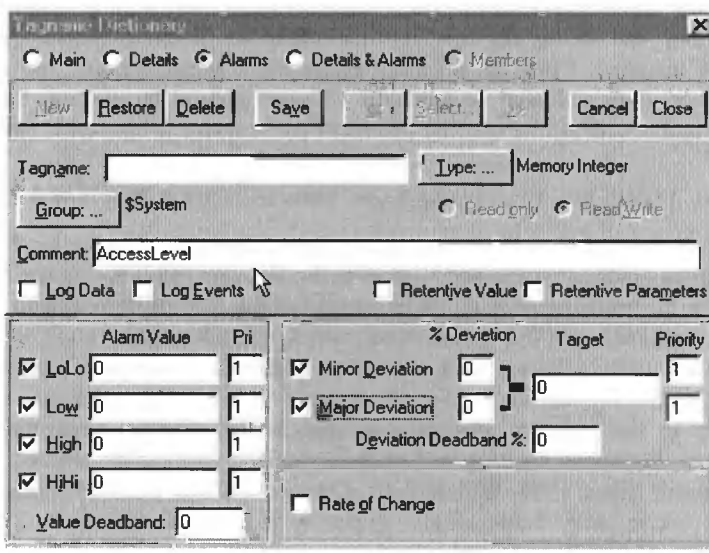

Fig. 1. Variables defining and setting up the alarms

After the location in the wizard window of the Alarm Display, alarm texts appear on the screen. After the script has undergone necessary modification, alarms can be sent in the

graphic or sonic form. They can also be sent through the Internet to a letterbox or in the form of SMS. Figure 2 presents an example text field with the alarms.

MM/DD HH:MM:SS	EVT Type	Pri	Name	GroupName	Value/Limit
11/01 23:58:09	ALM HI	1	poz1	$System	41/ 40
11/01 23:58:11	ALM HIHI	1	poz2	$System	33/ 32
11/01 23:59:11	ALM HI	1	poz	$System	61/ 60

Fig. 2. The fragment of window with text alarms

The InTouch is also equipped with the function which enables us to log data on the file. The choice of the variables undergoes under the same procedure as in the case of alarms while creating variables. It takes place through marking the Log Data option in the windows shown in Fig. 1. Additionally an option of historical logging from menu Special/Configure/Historical logging can be used. The data logged to the file can be seen while putting the HistTrend wizard from the Trends group in the application window.

3. DESIGN OF THE PROCESS OF GRAPHICS IN INTOUCH

After the InTouch has been started, a window of Manager application opens. Here we can name a new application and define its resolution. In order to read the application we must start the Window Marker program. Next we create windows, or in other words, basic objects where graphic elements can be drawn. Figure 3 presents a window WindowMarker where the new application windows are created.

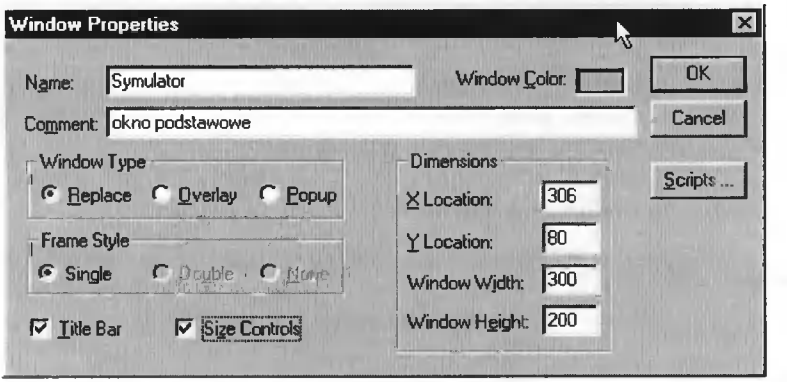

Fig. 3. Creating a new window in the InTouch

While creating a new window we name it and define its color, size and type (Replace – closes the adjoining windows, Overlay – the window does not influence a state of the adjoining windows, Popup – the window always remaining on the top). Next we define the position of the window in relation to the left upper corner of the screen and its size. Marking the Size Controls index, one can change the size of the window with a mouse while creating an application, the Title Bar index turns on the title belt in the window.

After the windows have been created in WindowMarker, one should start drawing objects while they are going to be visualized. The first stage of creating applications requires drawing of bigger objects and inserting small elements. Graphics in the InTouch can be created by drawing simple graphic objects (a rectangle, an ellipse and

other objects) or by inserting push-buttons and bitmaps created with the help of other programmes. Symbol Factory library of the graphic objects is added to the InTouch software whose symbols may also be used to create graphics. The Factory Symbol library can be installed by additional starting of the ProductivityPack installation. This visualization has totally been created with the use of this library. Figure 4 presents example symbols from the Symbol Factory library.

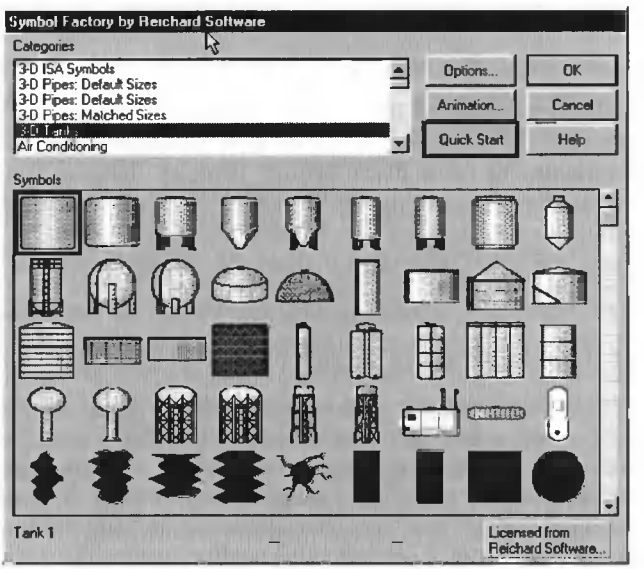

Fig. 4. Symbol Factory library

By creating the graphics in the InTouch one can also use a number of ready wizards, such as: measurers, lamps, push-buttons, switches, sliders, clocks, frames, panels and Windows Control windows.

4. APPLICATION PROGRAMMING IN THE INTOUCH

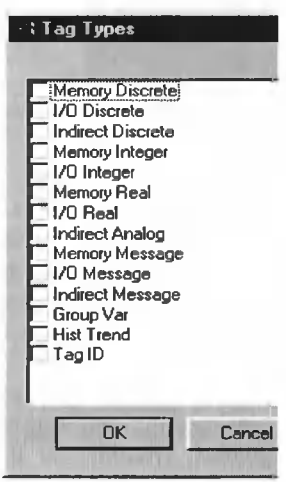

Fig. 5. Tag types

After the application of graphics has been finished, one should define the variables. It is done by opening the Tagname Dictionary window of the Special menu (Fig. 5). In the InTouch there are variables of the following types: Memory (variables of the memorial type), I/O (variables which write/record/read the values in other programs), Indirect (indirect variables), special variables (group, historical trend, on identifier of the variable). One should keep in mind that after the variable have been defined, changes should be confirmed with the help of the save button.

The next stage of the application programming requires the creation of animation links between the objects and the variables. When we click on a graphic object twice, we enter the object and define its arrangements. In case of wizards we can attribute a variable to the object and define

its colors. In case of the drawings from the Symbol Factory library and the manually drawn objects imported from other application, the way of animation is more complex. After the double click with the left key of the mouse on the graphic object, there unrolls the menu presented in Fig. 6. According to the object, we can choose one or more animation connections. In most of the animation connections we attribute the variables to the objects; the exceptions are the Action animation connection (scripts can be made in it) and Shown and Hide Window (they are for opening and closing pointed windows). The animation links of the Touch Links group are for introducing the values, the rest is for showing the information generated by the program.

Besides the animation connections in the InTouch one can also define scripts of the following types:

- Application Scripts (scripts referring to the whole application),
- Windows Scripts (referring to the given window),
- Key Scripts (realized after pushing the key or a key combination on the keyboard),
- Condition Scripts (conditional scripts, realized once or cyclically after meeting a defined condition),
- Data Change Scripts (scripts realized after the change of the attributed variables values),
- Quick Functions (scripts that can be generated in other scripts and animation connections).

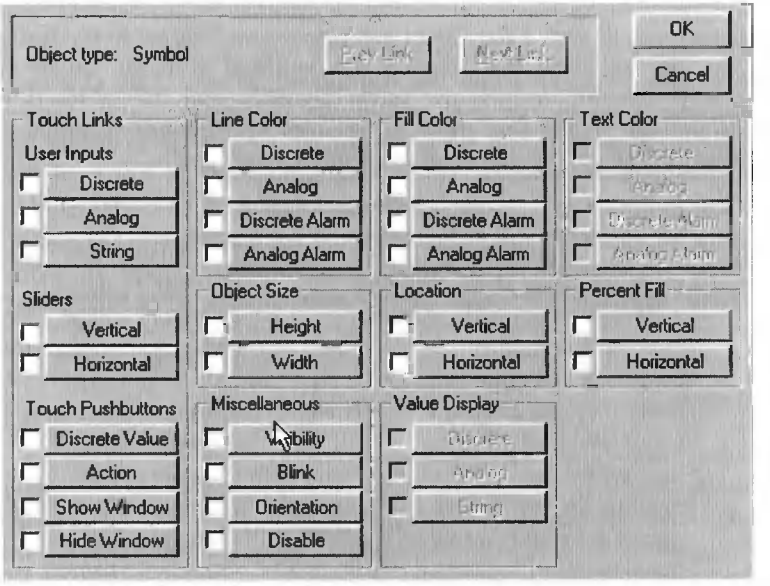

Fig. 6. Animation connection of the graphic objects with the variables

5. VISUALIZATION OF THE TWO-LIQUID MIXING PROCESS

An example application created in the Wonderware InTouch is the visualization of the two-liquid mixing process. Here the way of creating this application is presented.

In the application Manager window the 'two-liquid mixing' application was created with 1024x768 resolution. After starting the WindowMarker the windows from

Table1 were created. In the Menu window the push-buttons were placed and inserted and the animation links presented in Fig. 7 were inserted.

Fig. 7. 'Menu' Window

Next Date and Time window of the Menu push-button were started as well as the wizards of the clock (Digital Time Clock) and date (Digital Date) from the Clocks library. The clock was linked together with the $Hour and $Minute system variables while the date – with the $DateString system variable. For the push-button a Show Window - Menu animation link was created.

Table 1. Windows in the 'two liquid mixing' application

Name of the window	Type	X margin	Y margin	X size	Y size
Date and time	Popup	0	0	1024	80
Basics	Overlay	0	79	1024	580
Menu	Popup	0	660	1024	68
Auto	Overlay	0	79	1024	580
Alarms	Overlay	0	79	1024	580

Then the containers, as well a the valves and pipes were inserted to the Basic window, according to Fig. 8a. Next the drawing was enriched with the extractions in the containers, level sensors, opening the valves signaling and 'the water flowing out', according to Fig. 8b. As the next step, the variables were defined according to Table 2 and the animation links to the particular elements were set up.

Table 2. Variables definition

variable	variable description	variable type	min	max
Pozaz	a given level in the A container	Memory Integer	0	50
Pozbz	a given level in the B container	Memory Integer	0	50
Poza	level in A container	Memory Integer	0	50
Pozb	level in B container	Memory Integer	0	50
Pozc	level in C container	Memory Integer	0	100
Czasz	a given time of mixing	Memory Real	0	100
Czas	time of mixing	Memory Real	0	100
z1	opening the entry valve of A container	Memory Discrete		
z2	opening the entry valve of B container	Memory Discrete		
z3	opening the trigger valve of a container	Memory Discrete		
z4	opening the trigger valve of b container	Memory Discrete		
z5	opening the trigger valve of c container	Memory Discrete		
z6	mixing	Memory Discrete		
z1a	an accessory to z1	Memory Discrete		
z2a	an accessory to z2	Memory Discrete		
z3a	an accessory to z3	Memory Discrete		
z4a	an accessory to z4	Memory Discrete		
z5a	an accessory to z5	Memory Discrete		

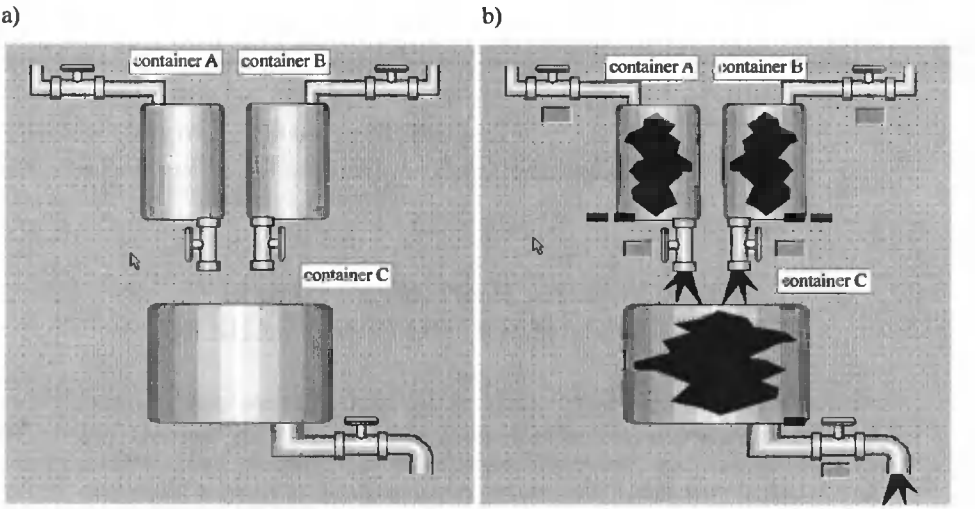

Fig. 8. Visualization of the two liquids mixing process: a) an initial drawing, b) the final view

6. CONCLUSIONS

To present the principle of the application created in the InTouch, a process of two-liquid mixing was used. The use of the process with a small number of inputs and outputs enabled us to present the phenomena in a simple way. Nevertheless that application enabled us to observe the course of the real process (e.g. the process of making fruit juice out of concentrate and water). To make it possible, one should configured I/O server as well as change the types of the variables from Memory Discrete on the I/O Discrete giving them names of the access to the controller and choosing a communication record. Many examples of the process visualization are presented in bulletins specialized in automatics published by Astor in Krakow.

ACKNOWLEDGEMENT

The paper was developed as part of the Rector's project no W/WM/3/2005 realized at Białystok Technical University.

REFERENCES

[1] InTouch software, 2000. Biuletyn Automatyki 2.
[2] Materiały szkoleniowe InTouch, Cz. I. Tworzenie i serwisowanie aplikacji.
[3] Materiały szkoleniowe InTouch, Cz. II. Zagadnienia zaawansowane.
[4] InTouch – Pierwsze kroki, 2003. Astor Kraków.
[5] InTouch – Podręcznik użytkownika, 2005. Astor Kraków.
[5] Peszyński K., Siemieniako F., 2002. Regulacja i sterowanie, podstawy, przykłady. Wyd. Uczeln. ATR Bydgoszcz.

Review by prof. Janusz Sempruch

University Press
University
of Technology
and Agriculture
in Bydgoszcz

DEVELOPMENTS IN MACHINERY DESIGN AND CONTROL
Vol. 4 (2005) 27 – 40
Scientific Journal

Zdzisław Gosiewski, Arkadiusz Mystkowski[1]
Bialystok Technical University, Department of Automatic and Robotic
Wiejska 45C 15-351 Bialystok, Poland

ROBUST CONTROL OF ONE AXIS OF SHAFT SUPPORTED MAGNETICALLY

Abstract: This paper presents a robust control of magnetic suspension of shaft. The dynamics of magnetic suspension systems are characterized by their instability and uncertainty of plant. Therefore except modeling of plant we determined a model of parametrical uncertainty. The uncertainty is modeled on additive. The uncertainty parameters we assumed current stiffness k_i and displacement stiffness k_s. The performance of closed loop system, limits of signals and disturbances influence are determined with the weighting functions. Three weighting functions are designed: $W_e(s)$ – penalizing error signal e, $W_u(s)$ – penalizing input signal u, and $W_y(s)$ – penalizing output signal y. For this functions and uncertainty model we assigned augmented control model. For augmented control system we assigned robust controller. The robust controller was assured high quality of control despite of uncertainty model of plant, disturbances in systems, limits of signals and high dynamics of system. Next the H_∞ closed loop system is compared with standard PID closed loop system. Finally simulation results show effectiveness of control system as good initial responses/transient responses and robustness of designed robust controller.

Keywords: parametric uncertainty, additive uncertainty, weight functions, H_∞ controller

1. INTRODUCTION

The active magnetic suspension system is a non-contact suspension of a shaft. That means there are no friction forces and no mechanic wear in kinematic pairs. A dynamic development of mechatronic systems like magnetic suspensions needs new advanced control methods. Standard control methods are not able to take into account all factors which influence the static and dynamic quality of the closed-loop system. The robust control allows us to achieve a good control performance in spite of disturbances and uncertainty of the plant. Particularly the robust control method can be used to control the nonlinear and unstable systems [7]. The limits of signals can be considered in robust stable systems. In the paper the robust control is applied for a magnetic bearing system.

In our considerations we assumed that the rotor was supported in two radial magnetic bearings and one axial bearing [3]. Each radial bearings controls motion of

[1]Corresponding author. *Tel.:* +48-85-746-9231; *fax:* +48-85-746-9231
E-mail address: mystek@pb.bialystok.pl (A. Mystkowski)

rotor in two directions. We assumed that the control system can be designed independently for each control direction. In this work the plant model and uncertainty model of plant was shown. The control law was designed for only one axis direction of shaft. The mass of rotor was reduced to one point. Here also the manually tuned PID controller was designed. Then the performances of PID and H_∞ controllers were compared. In the augmented system we considered the additive uncertainty model. The performances of closed-loop system were defined. For robust control purpose, the weight functions were designed. The input and output signals of the system were shaped be properly chosen weight functions.

2. CONTROL PLANT

The control plant is a rotor supported in electromagnetic field of two radial magnetic bearings. The open-loop model of magnetic bearings system for each axis of control is given as follows [3]:

$$\begin{aligned} \dot{\mathbf{x}} &= \mathbf{A}_c\mathbf{x} + \mathbf{B}_c\mathbf{u}, \\ \mathbf{y} &= \mathbf{C}\mathbf{x}, \end{aligned} \tag{1}$$

where:

$\mathbf{x}$ – state vector, $\mathbf{u}$ – control vector, $\mathbf{y}$ - output vector,

$$\mathbf{A}_c = \begin{bmatrix} 0 & 1 & 0 & 0 \\ v_1 & 0 & v_{21} & -v_{22} \\ 0 & -v_{31} & -v_{41} & 0 \\ 0 & v_{32} & 0 & -v_{42} \end{bmatrix}, \quad \mathbf{B}_c = \begin{bmatrix} 0 & 0 \\ 0 & 0 \\ v_{51} & 0 \\ 0 & v_{52} \end{bmatrix}, \quad \mathbf{X} = \mathbf{I},$$

$$v_1 = \frac{k_{s1} + k_{s2}}{m_r}, v_{21} = \frac{k_{i1} + k_{i2}}{m_r}\frac{x_o + x_z}{2x_o}, v_{22} = \frac{k_{i1} + k_{i2}}{m_r}\frac{x_o - x_z}{2x_o}, v_{31} = \frac{k_{i1}}{L_{s1} + L_{o1}},$$

$$v_{32} = \frac{k_{i2}}{L_{s2} + L_{o2}}, v_{41} = \frac{R_1}{L_{s1} + L_{o1}}, v_{42} = \frac{R_2}{L_{s2} + L_{o2}}, v_{51} = \frac{k_{w1}}{L_{s1} + L_{o1}}, v_{52} = \frac{k_{w2}}{L_{s2} + L_{o2}},$$

x_o – air gap [m], x_z – mass displacement of the shaft from the center of magnetic bearing to operating point [m], K – design constant of magnetic bearing, u – voltages [V], R – resistance of coils [Ω], L_s, L_o – inductance losses and inductances of air gap [H], k_i –current stiffness [N·A^{-1}], k_s – displacement stiffness [N·m^{-1}], m – mass of rotor reduced to bearing plane [kg], A – radial surface of pole piece [m^2], N – number of coils. The index $\{_1\}$ and $\{_2\}$ describes upper and lower coils.

The operating point is described by parameters:

$$x = x_z, \quad i_{z1} = \frac{x_o - x_z}{x_o} i_0, \quad i_{z2} = \frac{x_o + x_z}{x_o} i_0. \tag{2}$$

The linearized model of the plant is described by following transfer function [3]:

$$G(s) = \frac{\dfrac{2k_i}{m}}{(L_s + L_0)s^3 + Rs^2 - (L_s + L_0)\dfrac{2k_s}{m}s - R\dfrac{2k_s}{m} + L_0\dfrac{2k_s}{m}s}. \tag{3}$$

Nominal Model of the Plant

The model of plant with nominal parameters is called a nominal model. The values of nominal parameters are calculated for some operation point. The nominal model has to reflect the real plant as exactly as possible. The uncertainty model should be smaller for good control performances. When the model of the plant well corresponds to real plant, the uncertainty model is small.

We have assumed that in magnetic bearings system the uncertain parameters are: k_i and k_s. In our case the nominal values are: $k_{i0} = 280$ [N·A^{-1}] and $k_{s0} = 2{,}3\ 10^6$ [N·m^{-1}]. For the following nominal data ($m = 22$ [kg], $R = 0.5$ [Ω], $L_s = 0$ [H], $L_0 = 0.05$ [H]) the nominal model of the plant is given as follows:

$$G_0(s) = \frac{25{,}5}{0{,}05s^3 + 0{,}5s^2 - 104550} \tag{4}$$

Figure 1 shows the simulation scheme for nominal model of active magnetic suspension for one axis.

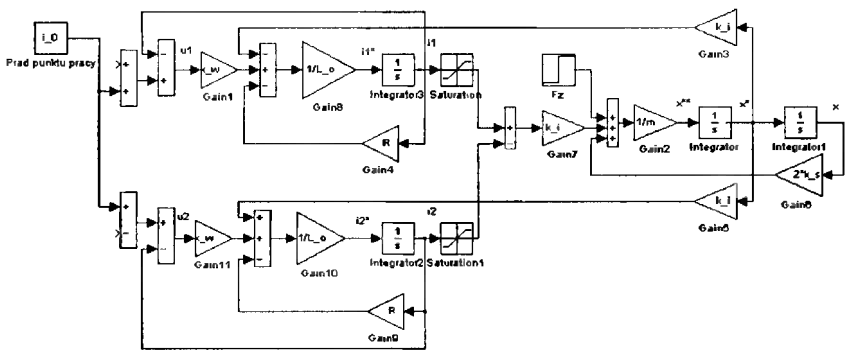

Fig. 1. Nominal model of active magnetic suspension

3. DESIGN OF THE UNCERTAINTY MODEL IN MAGNETIC BEARINGS SYSTEM

The robust controller should assure good performances when nominal model does not exactly reflect the real plant. Because all the states of process control cannot be forecast, the uncertainty model is needed. Also, when external disturbances have high dynamics (wide frequency spectrum), the uncertainty model is necessary. So the robust controller was designed based not only on the nominal model of plant. The robust control with uncertainty modeling is especially useful when parameters of real plant change.

3.1. PARAMETRIC UNCERTAINTY

For robust control purposes, we have to define how nominal model differs from the real plant at particular frequencies. We also have to assure the required bandwidth of the closed-loop system. The size of the model variation is defined by uncertainty of parameters. The position of shaft x_z in air gap x_0 causes changes of induction in upper and lower coils [3]:

$$L_{o1} = \frac{K_1}{2(x_o - x_z)}, \quad L_{o2} = \frac{K_2}{2(x_o + x_z)}, \tag{5}$$

The values of parameters k_i and k_s are as follows:

$$k_i = \frac{K}{2}\frac{i_0}{x_0^2} = L_0\frac{i_0}{x_0^2}, \; k_s = \frac{K}{2}\frac{i_0^2}{x_0^3} = L_0\frac{i_0^2}{x_0}. \tag{6}$$

The values of uncertain parameters are shown in Table 1.

Table 1. The values of uncertain parameters

Parameter	Nominal value	Deviation	
		Min.	Max.
x_0 [m]	$0.5\cdot10^{-3}$	$-0.25\cdot10^{-3}$	$0.25\cdot10^{-3}$
L [H]	0.05	0.03	0.1
k_i [N/A]	280	162	540
k_s [N/m]	$2.3\cdot10^{6}$	$0.8\cdot10^{6}$	$2.9\cdot10^{6}$

For minimum and maximum values of uncertain parameters, the model of plant is given in the form:

$$G(s)_{\min} = \frac{14.7}{0.05s^3 + 0.5s^2 - 36364}, \; G(s)_{\max} = \frac{49}{0.05s^3 + 0.5s^2 - 131820} \tag{7}$$

Figure 2 shows amplitude-frequency characteristics of the plant with minimum and maximum values of uncertain parameters k_i and k_s.

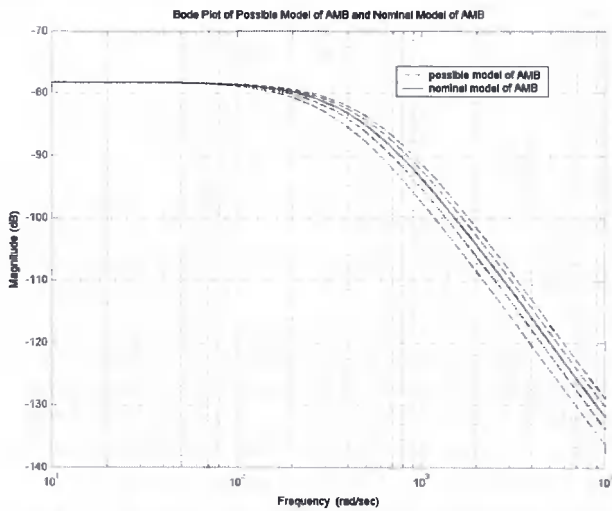

Fig. 2. Amplitude-frequency plot of the plant with uncertain parameters k_i and k_s

The uncertainty model of parameters k_i and k_s is given in the form [12]:

$$\begin{aligned} k_i &= k_{i0} + W_{k_i}\delta_i \quad \text{for } |\delta_i| \le 1, \\ k_s &= k_{s0} + W_{k_s}\delta_s \quad \text{for } |\delta_s| \le 1, \end{aligned} \tag{8}$$

where W_{k_i}, W_{k_s} – weight functions of uncertain parameters k_i and k_s.

The simulation model of robust control with uncertain parameters k_i and k_s was shown in Fig. 3.

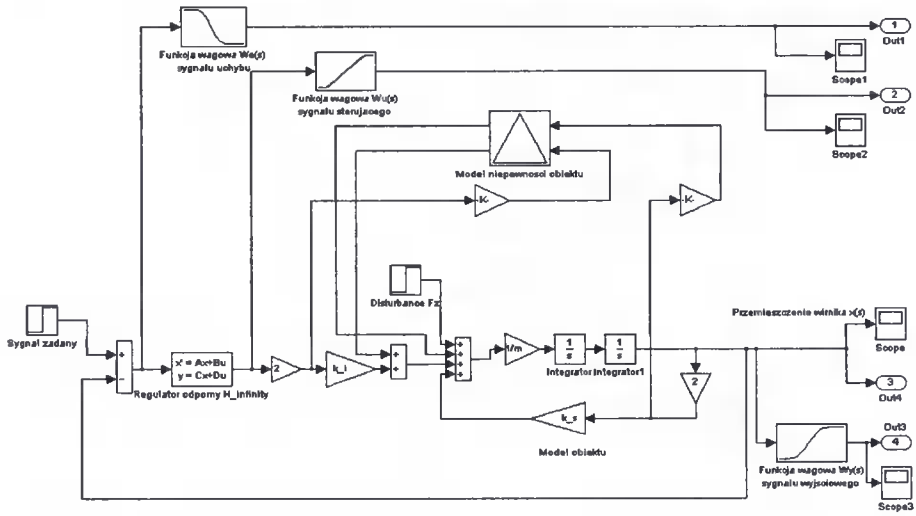

Fig. 3. Simulation model of H_∞ closed-loop system with parametric uncertainty

3.2. ADDITIVE UNCERTAINTY

For the nominal model of the magnetic bearing system described by equation (3), the model of additive uncertainty is given as follows [13]:

$$\Delta_a(s) = G(s) - G_0(s) . \tag{9}$$

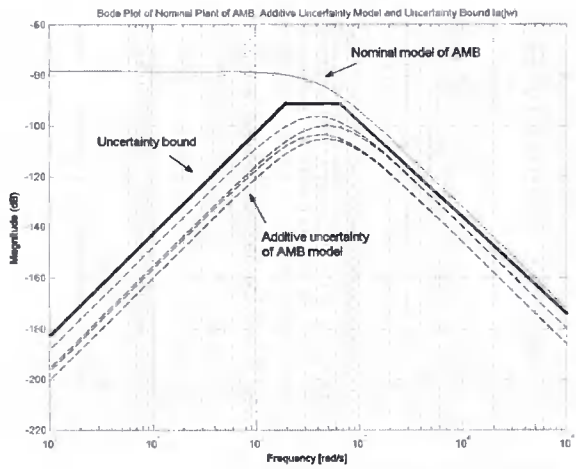

Fig. 4. Amplitude-frequency plot of the nominal model, additive uncertainty $\Delta_a(j\omega)$ and boundary function $l_a(j\omega)$

The frequency information about additive uncertainty model is needed. The spectral transfer function of additive uncertainty is given in the form:

$$|\Delta_a(j\omega)| = |G(j\omega) - G_0(j\omega)| \le l_a(j\omega), \forall \omega. \tag{10}$$

The maximum value of additive uncertainty is limited by boundary function $l_a(j\omega)$. Fig. 4 shows amplitude-frequency plot of additive uncertainty function $\Delta_a(j\omega)$ and boundary function $l_a(j\omega)$.

Fig. 5 shows H_∞ closed-loop system with additive uncertainty model.

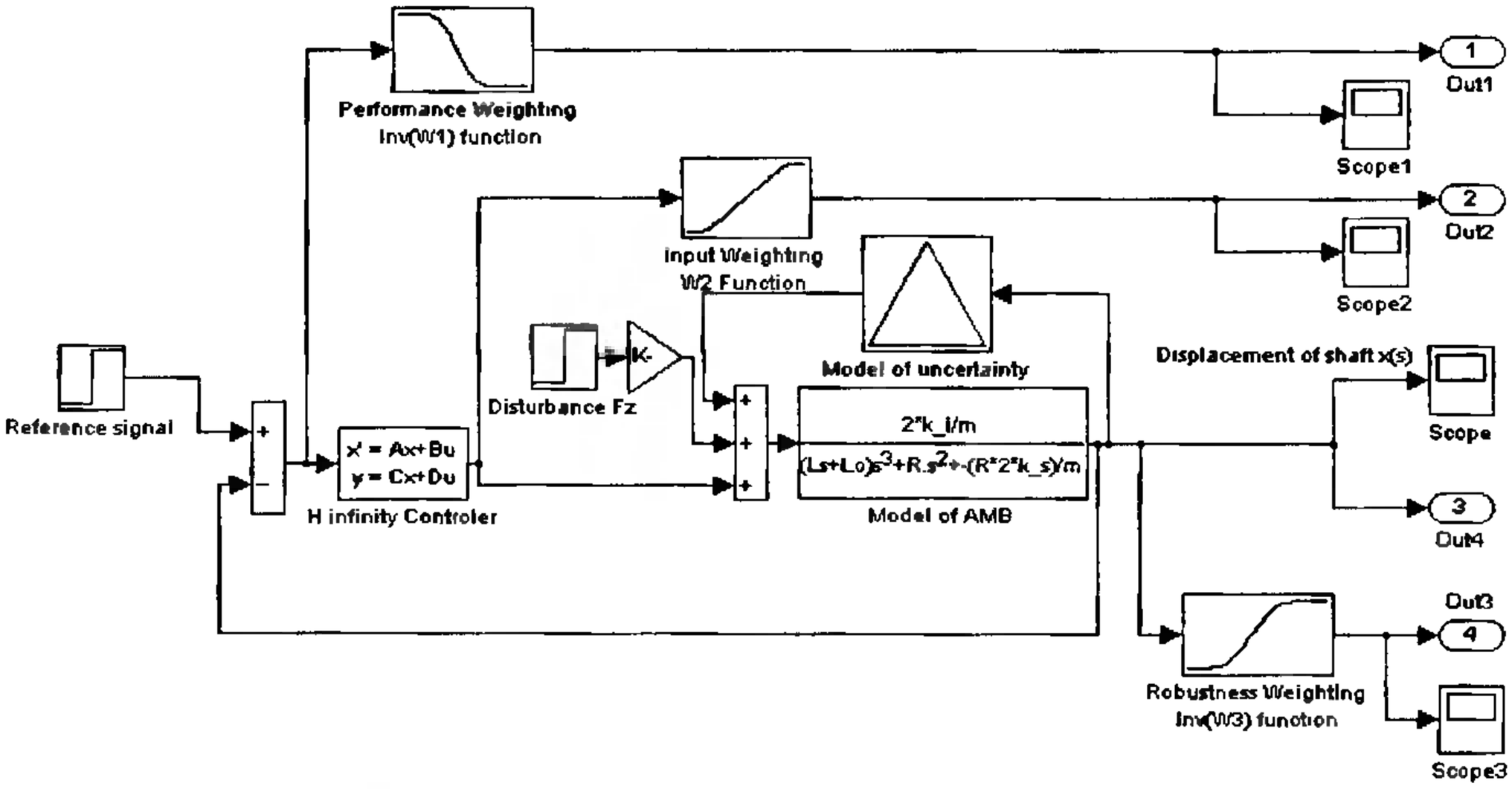

Fig. 5. H_∞ closed-loop system with the additive uncertainty model

4. DESIGN PROCESS OF THE CONTROL SYSTEM

4.1. Weight functions

The performance of the robust control system depends on the properties of chosen weight functions. The weight functions describe the influence of particular signals on the control system. In the paper input weight function $W_u(s)$, robustness weight function $W_y(s)$, and performance weight function $W_e(s)$ are designed:

$$W_e(s) = \frac{0.33s^2 + 577.4s + 250000}{s^2 + 100s + 2500}$$

$$W_y(s) = \frac{10s + 30000}{s + 60000} \tag{11}$$

$$W_u(s) = \frac{s + 666.7}{0.01s + 1000}$$

The robustness weight function $W_y(s)$ was designed based on complementary sensitivity function $T(s) = G_0(s)K(s)S(s)$. The input weight function $W_u(s)$ was assigned based on control function $R(s) = K(s)(I + G_0(s)K(s))^{-1}$. The performance weighting function $W_e(s)$ was selected based on sensitivity function $S(s) = (I + G_0(s)K(s))^{-1}$. Fig. 6 shows amplitude-frequency plots of weighting functions.

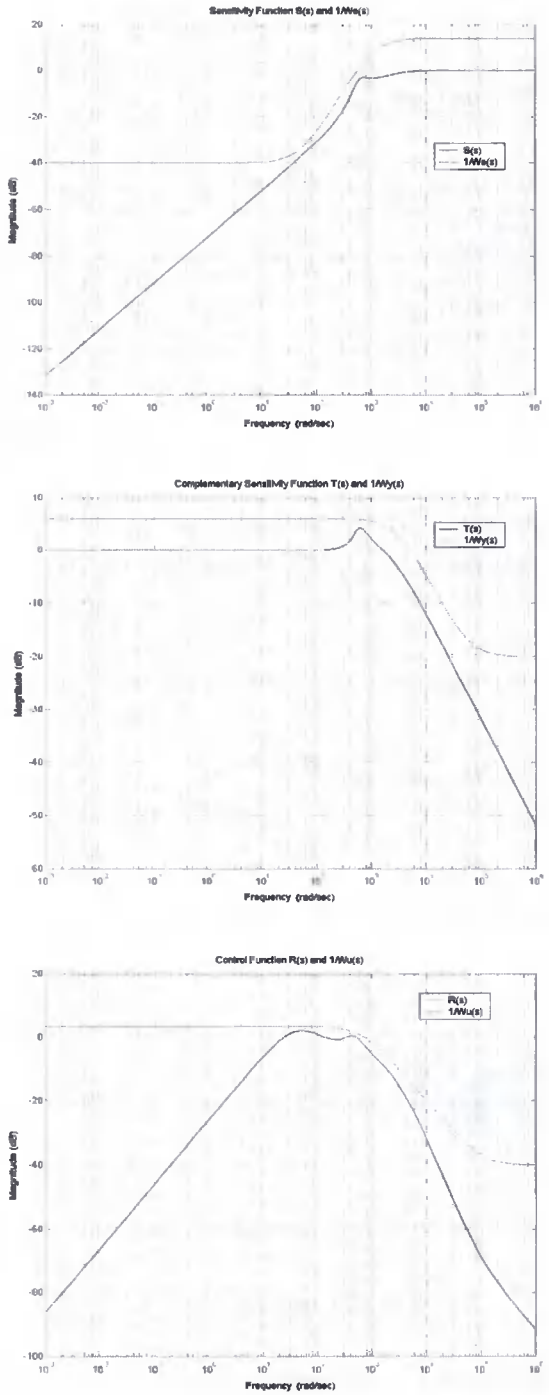

Fig. 6. Amplitude-frequency plots of weight functions: $W_u(s)$, $W_e(s)$ and $W_y(s)$

Fig. 7 shows simulation model of H_∞ closed-loop system with weight functions.

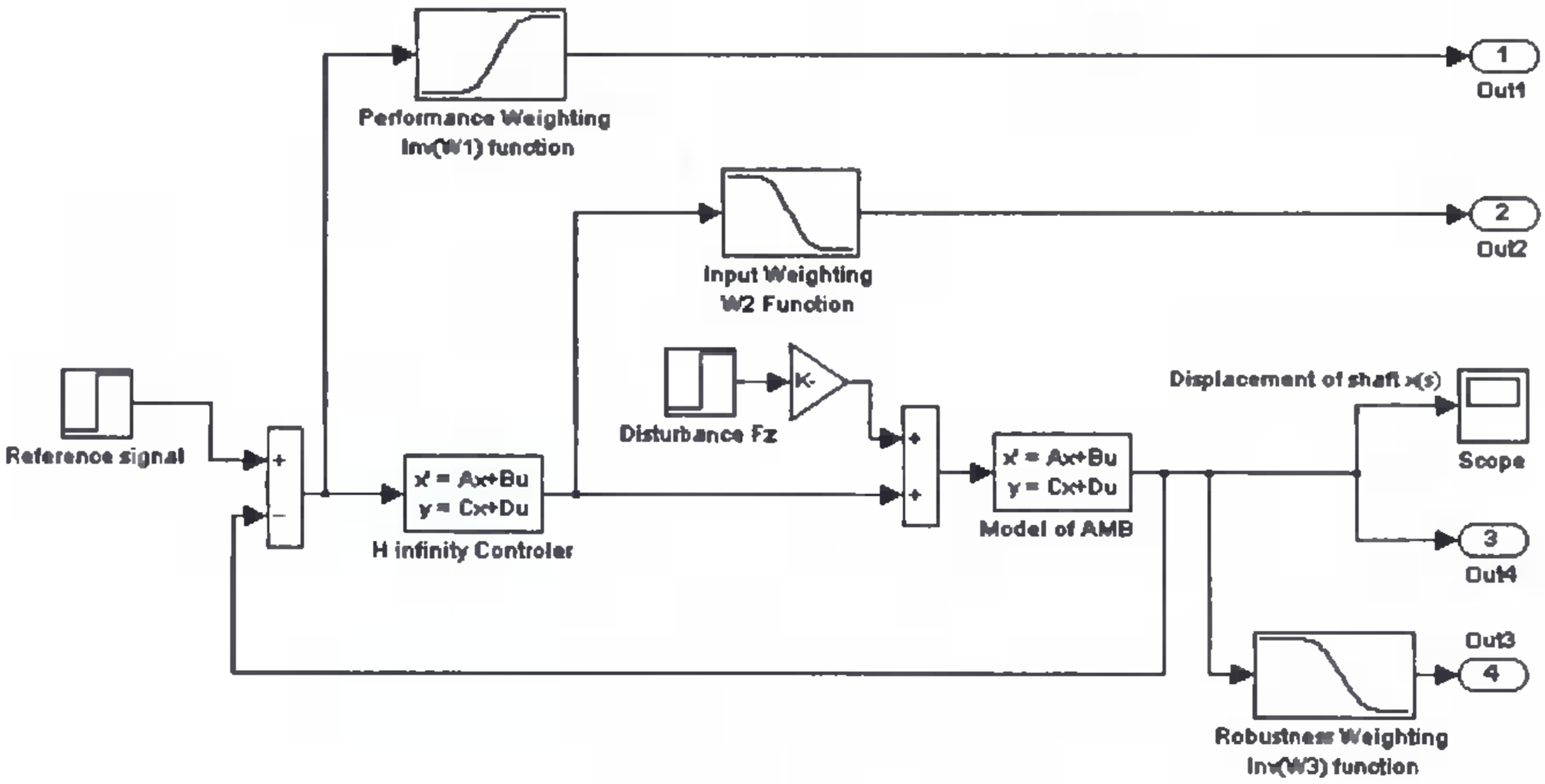

Fig. 7. Simulation model of H_∞ closed-loop system with weight functions

Fig. 8 shows amplitude-frequency plot of functions $S(s)$ and $T(s)$ with uncertainty of the plant.

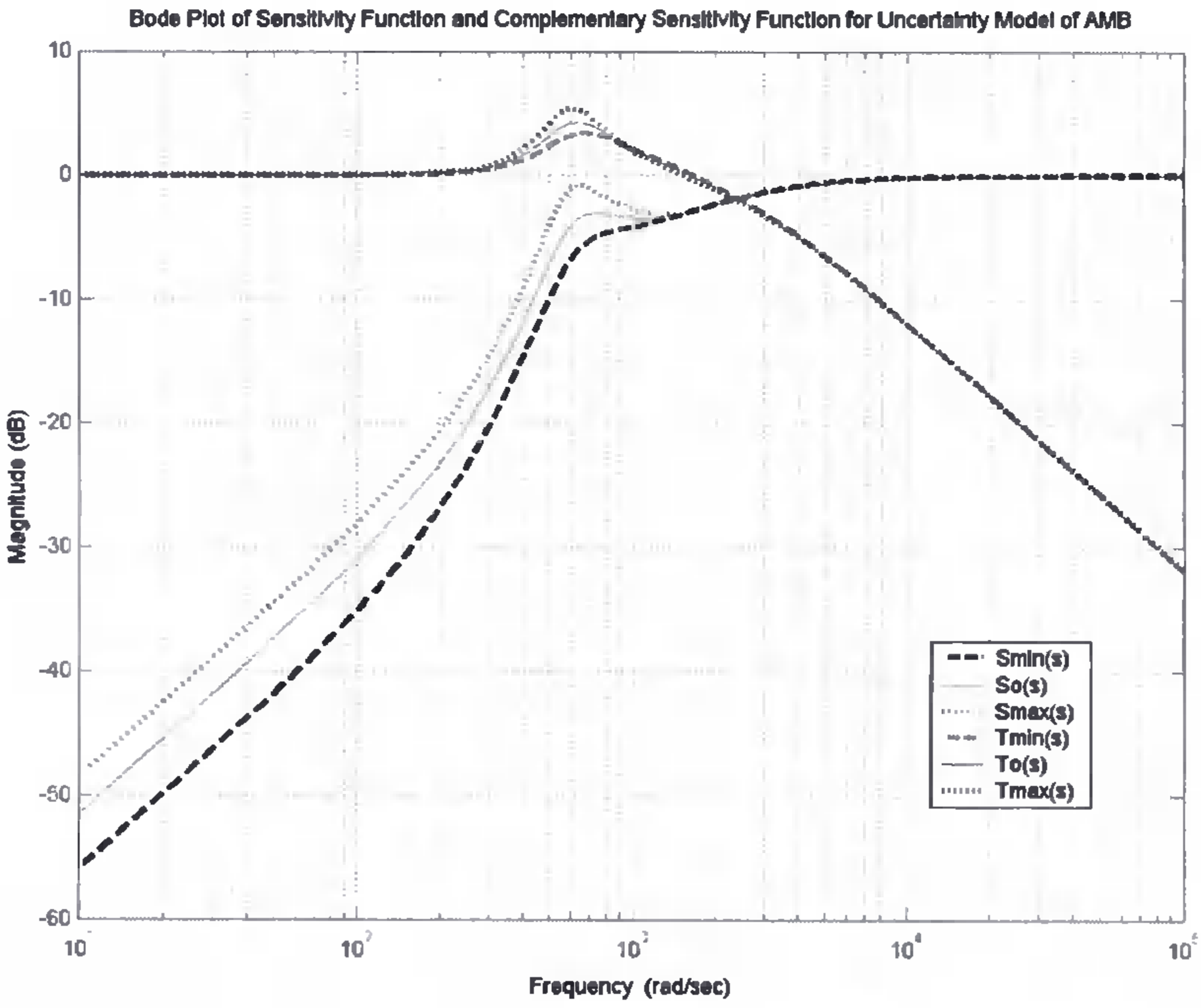

Fig. 8. Amplitude-frequency plot of functions $S(s)$ and $T(s)$ with uncertainty of the plant

The weighting functions limit the output and input signals of control system. The output signal (displacement of the shaft) is limited to 50% of air gap x_0=0,5 [mm]. The input signal (current control) is limited to 0÷10 [A].

Fig. 9 shows current control signals in upper and lower coils of magnetic bearings. The disturbance signal is a step load force F=800 [N].

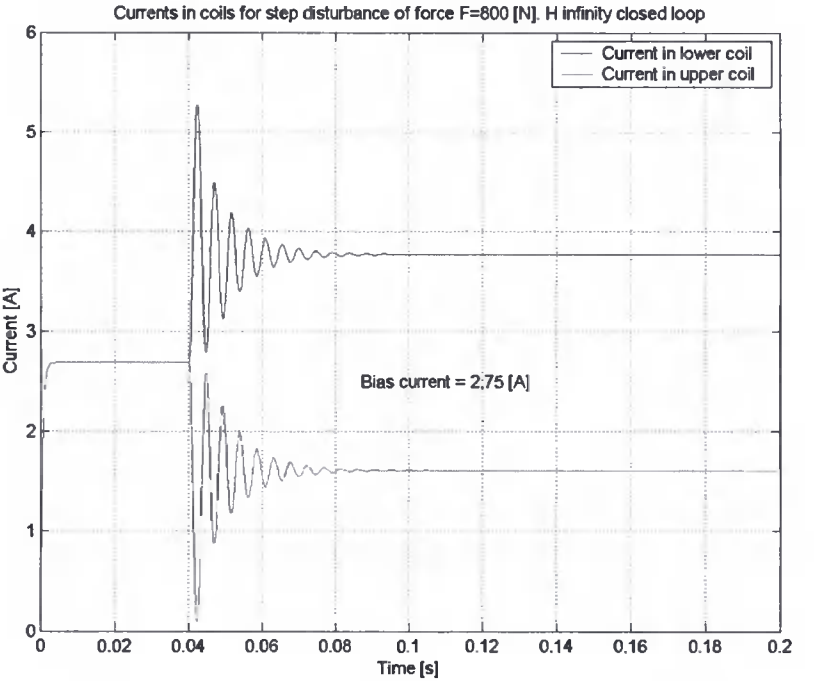

Fig. 9. Current control signals in upper and lower coils of magnetic bearings for step disturbance force F = 800 [N]

4.2. Design process of PID controller

The design process of robust controller is based on PID controller. The standard, manually tuned PID controller can be described by the following transfer function:

$$K(s) = \frac{(k_d s^2 + k_p s + k_i)}{s}. \tag{12}$$

For the magnetic suspension system, we have designed PID controller which is given by the following transfer function:

$$K(s) = \frac{100.6\, s^2 + 56150 s + 30900000}{s}. \tag{13}$$

Fig. 10 shows pole-map of PID closed-loop system and open-loop system.

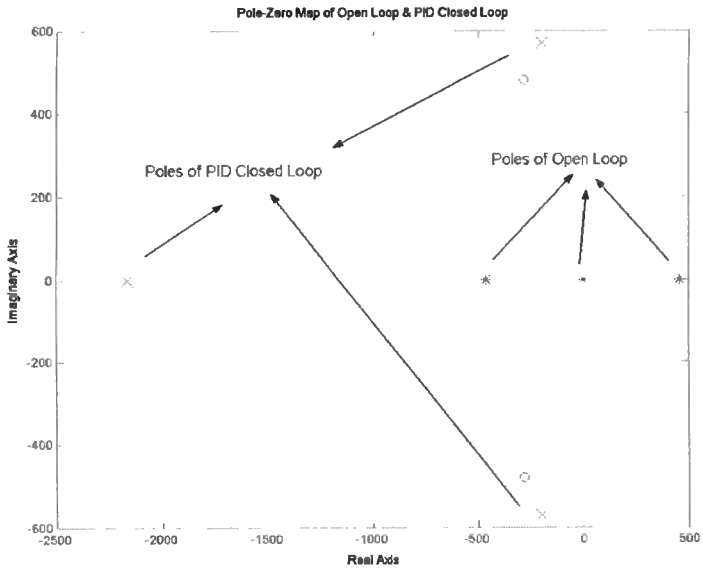

Fig. 10. Pole-map of PID closed-loop and open-loop systems

Fig. 11 shows Bode plot of PID closed-loop system.

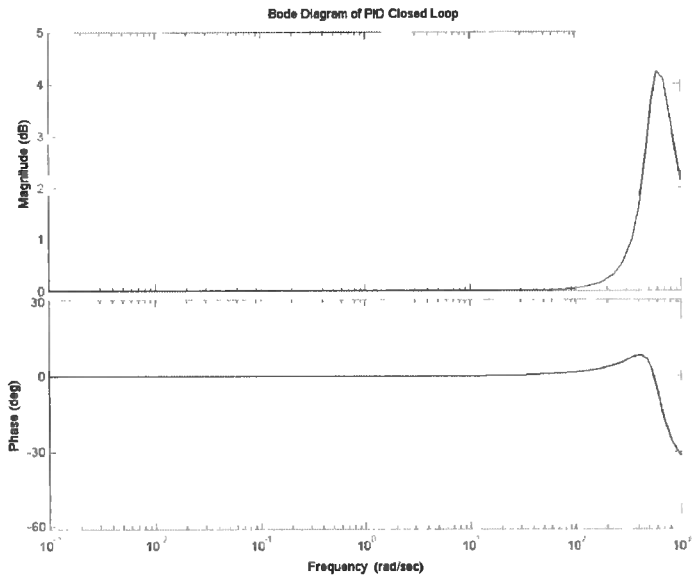

Fig. 11. Bode plot of PID closed-loop system

The displacement of the shaft with disturbance in a form of step force $F = 600$ [N] was presented in Fig. 12.

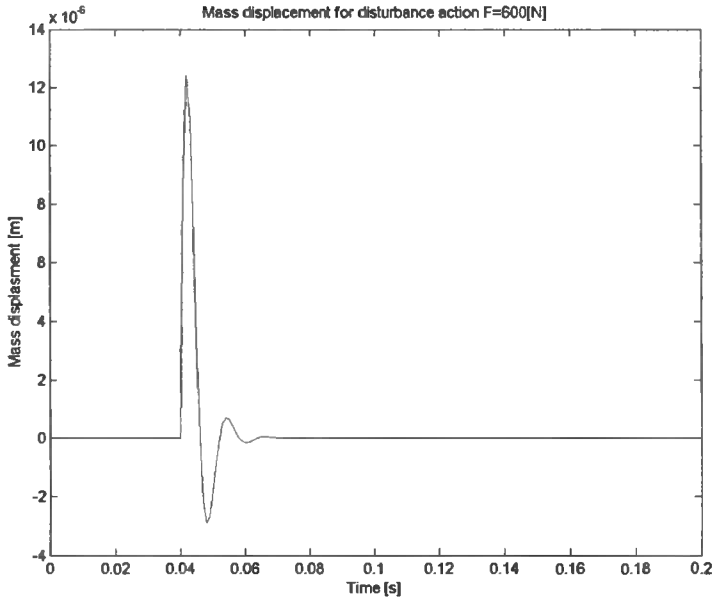

Fig. 12. Step response of PID closed-loop system for force F = 600 [N]

4.3. Design process of H_∞ controller

The robust control problem is to find stable controller K, which minimizes the following norm [1]: $\|F(G,K)\|_\infty = \sup_{\omega \in R} |F(G,K)(j\omega)|$. Fig. 13 shows a diagram of standard robust closed-loop system.

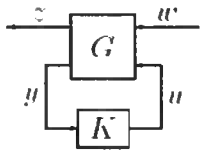

Fig. 13. Diagram of the robust closed-loop system: w – reference signal, u – control signal, z – output signal define H_∞ norm, y – measurement signal

For the robust controller the design process of the augmented model is necessary. The augmented model includes the model of the plant, uncertainties, and weight functions. In practice, the H_∞ robust control problem is to find controller K that fulfils the following condition [2]:

$$\|F(P,K)\|_\infty < \gamma \tag{14}$$

where γ is minimal value of the optimization factor.

The stability of the robust closed-loop system is described as follows [2]:

$$\forall \Delta \in H^\infty, \|r^{-1}\Delta\|_\infty < 1, \text{ if } \|rF(P,K)\|_\infty \le 1 \tag{15}$$

where r is boundary function of uncertainty function: $\|\Delta(j\omega)\| < r(j\omega)$. For exactly modeled process, the norm $\|r(j\omega)\|$ should be as small as possible.

The transfer function of H_∞ controller is given in the form:

$$H_\infty(s) = \frac{4\cdot10^5 s^5 + 8\cdot10^{17}s^4 + 5\cdot10^{22}s^3 + 4\cdot10^{25}s^2 + 1\cdot10^{28}s + 1\cdot10^{30}}{s^6 + 4\cdot10^7 s^5 + 5\cdot10^{12}s^4 + 1\cdot10^{17}s^3 + 7\cdot10^{20}s^2 + 7\cdot10^{22}s + 1\cdot10^{24}} \tag{16}$$

Fig. 14 shows step response and impulse response of PID and H_∞ closed-loop systems.

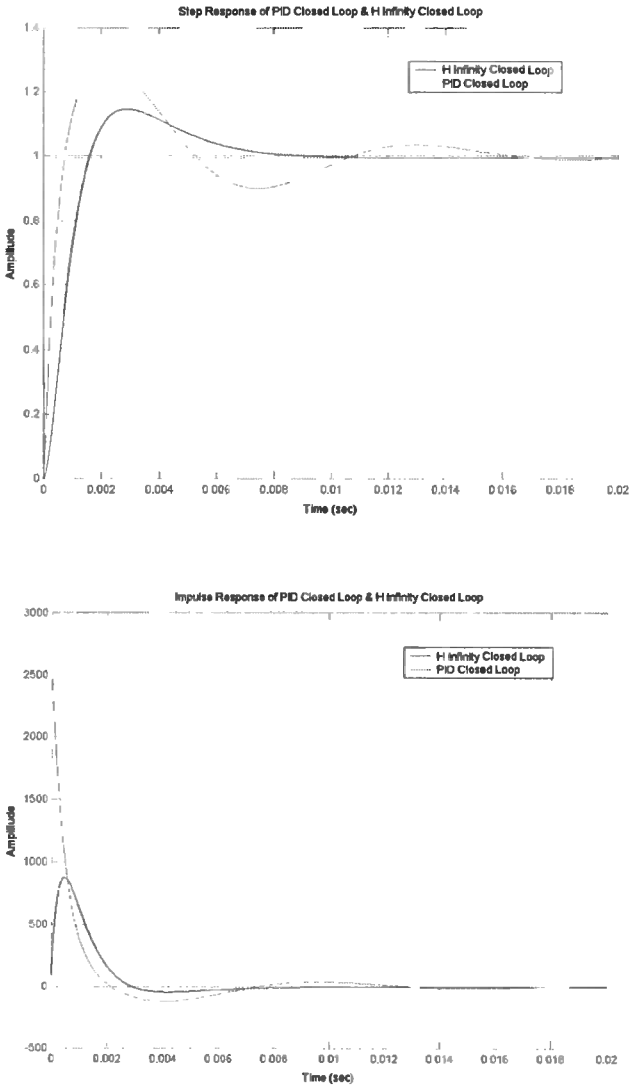

Fig. 14. Step response and impulse response of PID and H_∞ closed-loop systems

The H_∞ closed-loop system has a shorter control time and smaller overshot than PID closed-loop system. The H_∞ closed-loop systems for the uncertainty model of the plant is presented in Fig. 15.

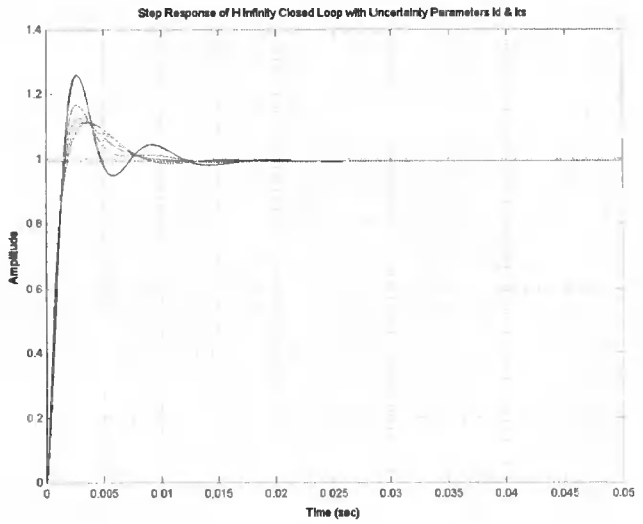

Fig. 15. Step response of H_∞ closed-loop systems with the uncertainty model of the plant

Although the uncertainty model is included in H_∞ closed-loop system, the H_∞ controller achieves better control performances than PID controller. The H_∞ controller is robust in comparison with PID.

5. CONCLUSIONS

In the paper the robust control method of the magnetic bearings system was investigated. The uncertainty model of the plant was derived. We considered the parametric uncertainty, which was included in the robust control system as additive uncertainty. The input and output signals in closed-loop system and disturbances were limited by weight functions. The H_∞ robust controller was designed and H_∞ closed-loop system was investigated. Then PID and H_∞ closed-loop systems are compared. The H_∞ controller achieves better performances than PID controller. The H_∞ closed-loop system is robust stable despite uncertainty. The designed H_∞ closed-loop system assures the wide bandwidth up to 1000 Hz.

REFERENCES

[1] Zhou K., Doyle J.C., 1998. Essentials of Robust Control. Prentice Hall New York.
[2] Zhou K., Doyle J.C., Glover K., 1997. Robust and Optimal Control. Prentice Hall New York.
[3] Gosiewski Z., Falkowski K., 2003. Wielofunkcyjne łożyska magnetyczne. Biblioteka Naukowa Instytutu Lotnictwa Warszawa.
[4] Doyle J.C., Francis B., Tannenbaum A., 1990. Feedback Control Theory. Macmillan Publishing Co. New York.

[5] Franklin G.F., David J., 1997. Feedback Control of Dynamic Systems. Prentice Hall New York.
[6] Lantto E., 1999. Robust Control of Magnetic Bearings in Subcritical Machines. Helsinki University of Technology (dissertation).
[7] Antila M., 1998. Electromechanical Properties of Radial Active Magnetic Bearings. Helsinki University of Technology (dissertation).
[8] Balas G., Chiang R., Packard A., Safonov A., 2005. Robust Control Toolbox. MathWorks.
[9] Tewari A., 2004. Modern Control Design with Matlab and Simulink. Wiley-IEE Press New York.
[10] Smith R.S., 1995. Model Validation for Robust Control: An Experimental Process Control Application. University of California, Santa Barbara.
[11] Namerikawa T., Seto H., 2001. H∞ DIA Control for robust performance of magnetic suspension systems. University of Technology, Nagaoka, 940-2188.
[12] Namerikawa T., Fujita M., 2001. Uncertainty structure and μ-Synthesis of a magnetic suspension system, University of Technology, Kanazawa, T.IEE, 121C(6), 198-234.

Review by prof. Wojciech Tarnowski

University Press
University
of Technology
and Agriculture
in Bydgoszcz

DEVELOPMENTS IN MACHINERY DESIGN AND CONTROL
Vol. 4 (2005) 41 – 49
Scientific Journal

Henryk Holka[1]

University of Technology and Agriculture, Department of Applied Mechanics
ul. Prof. S. Kaliskiego 7, 85–791 Bydgoszcz, Poland

EFFECT OF SUPPORT STRUCTURE RECEPTANCE ON MECHANISMS OPERATION

Abstract: The paper provides an analysis of the effect of the support rigidity on the operation of mechanisms founded on this structure. Cam mechanism was used as the example for analysis. The system was described with differential equations and then system responses were determined.

Keywords: cam mechanism, dynamic receptance, rigidity matrix, vibrations

1. INTRODUCTION

Many mechanical devices are founded on a high-receptance foundation; chemical and cement installations where different machinery aggregates are installed on multi-level steel structures, etc. If the operation frequency of these devices coincides with the resonance frequency of the support, then the operation can be disturbed.

The analysis covered by the present paper involved cam mechanism. The receptance system was described with the dynamic receptance recorded in the experiment, while the dynamic rigidity of the support – by reversing the receptance matrix. It was shown that the system, depending on the foundation rigidity, can give different responses. The solution to the equations was looked for different parameter configurations of the system analyzed.

2. PHYSICAL MODEL OF CAM MECHANISM AND EQUATION OF MOTION

The physical model of the system cam – cam follower is given in Fig. 1. As it seen from the figure, the cam is founded on the receptant structure. The rigidity of the structure can be changed. It is also possible to change the rigidity of spring k_1. The equation of motion for the system was derived by uncoupling respective elements of the mechanism.

Equations of motions (1a), (1b), (1c), and (1d) are:

$$m_1\ddot{x}_1 + c\dot{x} + k_1(h_1 + x) + N(t) = 0 \tag{1a}$$

$$m_2\ddot{x} - R(t) - N(t) - m_2 a\omega^2 \cos t\omega t = 0 \tag{1b}$$

[1] Corresponding author. *Tel.:* +48-52-340-82-92; *fax:* +48-52-340-82-50
E-mail address: holka@atr.bydgoszcz.pl (H. Holka)

$$R(t) = Z(h_2 - y) \quad \text{and} \quad h_2 = h_1 \frac{k_1}{Z} \tag{1c}$$

$$y = x + a(1 - \cos \omega t) \tag{1d}$$

where: m_1, m_2 – cam follower and cam mass,
k_1 – cam follower spring rigidity,
a – wheel eccentricity,
$Z(i\omega)$ – dynamic system rigidity,
h_1, h_2 – initial k1 spring and receptant support deflection

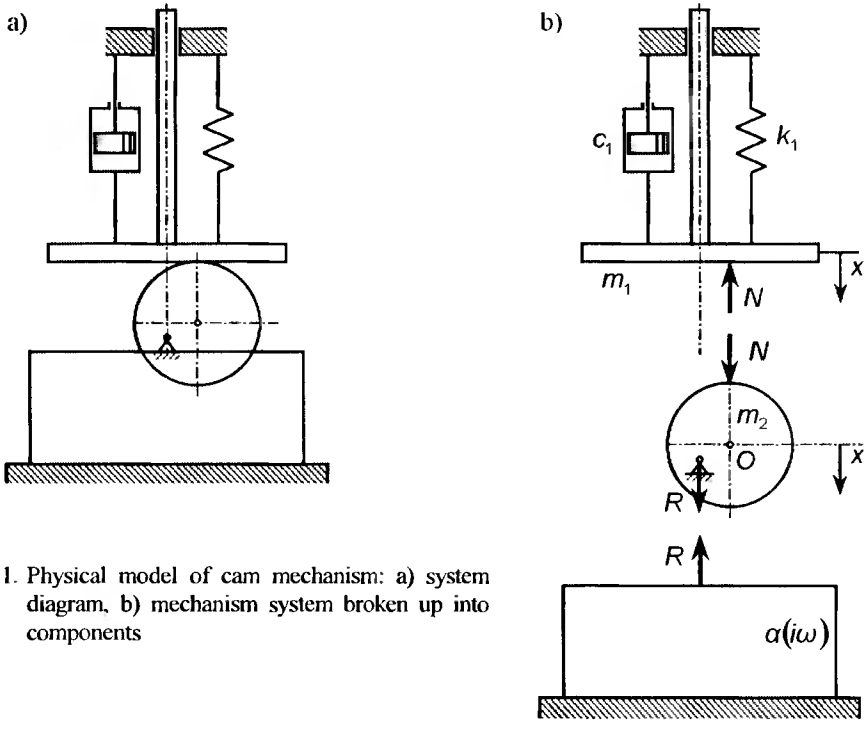

Fig. 1. Physical model of cam mechanism: a) system diagram, b) mechanism system broken up into components

Having eliminated internal forces N and R from equation (1), a dynamic equation of cam mechanism movement by one degree of freedom was obtained.

$$(m_1 + m_2)\ddot{x} + c\dot{x} + (k_1 + z)x = \left[m_2 a \omega^2 + Z(i\omega) \cdot a\right] \cos \omega t - Z(i\omega) \cdot a \tag{2}$$

For the system with multi-degrees of freedom, the rigidity matrix is the inverse matrix against the receptance matrix

$$\left[Z_{ij}(i\omega)\right] = \left[\alpha_{ij}(i\omega)\right]^{-1}, \tag{3}$$

and its elements are obtained not as a result of direct measurement but having inversed the receptance matrix $\alpha(i\omega)$. The receptance matrix of the receptant structure can be calculated analytically, or if it is difficult due to the structure complexity from the experiment.

In this paper receptance matrix was determined experimentally.

Only for the system of the 1. degree of freedom $Z(i\omega)=\frac{1}{\alpha(i\omega)}$.

The right side of the equation (2) consists of two components. If the system is linear, we can write:

$$(m_1+m_2)\ddot{x}_1+c\dot{x}_1+(k_1+Z)x_1=-Z(i\omega)\cdot a \tag{4a}$$

$$(m_1+m_2)\ddot{x}_2+c\dot{x}_2+(k_1+Z)x_2=P(t) \tag{4b}$$

$$P(t)=(m_2a\omega^2+Za)\cos\omega t \tag{4c}$$

$$x=x_1+x_2 \tag{4d}$$

Solving (4a), we obtain:

$$x_1=-\frac{Z(i\omega)\cdot a}{k_1+Z(i\omega)}=-\gamma\cdot a, \tag{5}$$

$$\gamma=-\frac{Z^{i\omega}\cdot a}{k_1+Z(i\omega)}, \tag{5a}$$

and it is a static deflection dependent on the dynamic deflection $Z(i\omega)$.

Solving the equation (4b), we assume that, the vector of input functions has the following form:

$$P(t)=(m_2a\omega^2+Z\cdot a)e^{i\omega t}=E+iF \tag{6}$$

where: E – amplitude of the real part of the input function,

F – amplitude of the imaginary part of the input function.

We assume the response in the following form:

$$X_2=X_2e^{(\omega t+\varphi i}=\bar{x}e^{i\omega t}=A+B \tag{7}$$

where: φ is the phase shift angle and A and B are real and imaginary parts of response module respectively.

Angle φ is calculated from the relationship $\varphi=\operatorname{arctg}\frac{B}{A}$.

It was also assumed that the matrix of dynamic rigidity $Z(i\omega)$ is a complex number.

$$Z(i\omega)=G+iH. \tag{8}$$

Substituting (6, 7, 8) to (4b), we obtain:

$$\left[-(m_1+m_2)\omega^2+i\omega c+k_1+G+iH\right](A+iB)=(m_2a\omega^2+G+iH)(E+iF) \tag{9}$$

Comparing real and imaginary parts, we obtain:

$$\begin{bmatrix}-\omega^2(m_1+m_2)+k_1+G & -\omega^2C+H\\ \omega C & -\omega^2(m_1+m_2)+k_1+G\end{bmatrix}\begin{Bmatrix}A\\B\end{Bmatrix}=\begin{bmatrix}m_2a\omega^2+G & -H\\ H & m_2a\omega^2+G\end{bmatrix}\begin{Bmatrix}E\\F\end{Bmatrix} \tag{10}$$

To simplify notation, the square matrix at the amplitude vector was marked as $[\mathbf{Q}]$, and matrix at the inputs vector as $[\mathbf{R}]$.

The following is obtained:

$$[\mathbf{Q}]\begin{Bmatrix} A \\ b \end{Bmatrix} = [\mathbf{R}]\begin{Bmatrix} E \\ F \end{Bmatrix}. \tag{11}$$

After premultiplication of the above equation by $[\mathbf{Q}]^{-1}$, assuming that the matrix is nonsingular, we obtain:

$$\begin{Bmatrix} A \\ b \end{Bmatrix} = [\mathbf{Q}]^{-1}[\mathbf{R}]\begin{Bmatrix} E \\ F \end{Bmatrix} \tag{12}$$

and finally:

$$X = \sqrt{A^2 + B^2}\,, \tag{13}$$

and the angle of phase shift is calculated as $\varphi = \operatorname{arctg}\dfrac{B}{A}$.

Assuming that dumping in the system is low, imaginary parts of the equation (10) disappear, and the response is given almost immediately:

$$X_2 = \frac{m_2\omega^2 + Z}{-\omega^2(m_1 + m_2) + k_1 + Z} \cdot a\cos\omega t = \lambda a\cos\omega t \tag{14}$$

Coefficient λ assumes then the following form:

$$\lambda(\omega) = \frac{m_2\omega^2 + Z}{-\omega^2(m_1 + m_2) + k_1 + Z} \tag{15}$$

Finally the response (4d):

$$x = \lambda a\cos\omega t - \gamma a\,. \tag{16}$$

Analyzing the formula (16), one can see that $Z(i\omega) \to \infty$ (very rigid support) $\lambda \to 1$ (equation 15) and $\gamma \to 1$, (equation 5).

So we receive response (16):

$$x = a(\cos\omega t - 1) \tag{17}$$

Let us consider the case when the support rigidity is much higher than k_1, $z >> k_1$. We can differentiate here three cases depending on frequency ω.

1. Case of low frequencies $\omega \approx 0$

We obtain:

$$\lambda = \gamma = \frac{Z(\omega)}{k_1 + Z(\omega)} < 1 \tag{18}$$

and hence:

$$x = \lambda \cdot a(\cos\omega t - 1) \tag{19}$$

Since $\lambda < 1$, then amplitude (19) is smaller than amplitude (17).

2. Case of mean frequencies $\omega^2 \approx \dfrac{k_1}{m_1}$

In this case

$$\lambda = \frac{m_2\omega^2 + Z}{-m_2\omega^2 + Z} > 1 \text{ and } \gamma = \frac{Z}{k_1 + Z} < 1 \tag{20}$$

The response:

$$x = a(\lambda \cos \omega t - \gamma) \tag{21}$$

3. Case of high frequencies

From formula (15) we can see that $\lambda << 1$, as:

$$\left|\omega^2 m_2\right| \leq \left|-\omega^2 m_1 - \omega^2 m_2 + k_1\right| \tag{22}$$

and finally the response assumes the form (16) where amplitude x is lower than $\underset{z\to\infty}{x}$:

$$X < \underset{Z\to\infty}{X} \tag{23}$$

3. CALCULATION RESULTS

To illustrate the theoretical calculation, simulations were made for specific data. Two foundation stiffness values $Z(\omega)$ and three different spring stiffness values k_1 were assumed. Dynamic stiffness $Z(\omega)$ was determined by reversing dynamic receptance $\alpha(\omega)$ which was defined experimentally. The dumping measurement was disregarded as considered low. For such assumed data, coefficients λ and γ for different combinations k_1 $Z(\omega)$ were calculated and, finally, response X was found.

The set of formulas:

$$x = \lambda a \cos \omega t - \gamma a$$

$$\lambda(\omega) = \frac{m_2\omega^2 + Z}{-\omega^2(m_1 + m_2) + k_1 + Z}$$

$$\gamma = \frac{Z(\omega) \cdot a}{k_1 + Z(\omega)}$$

The following combination were taken under consideration:

	$Z_1(\omega)$	$Z_2(\omega)$
k_1'	λ_1', γ_1'	λ_2', γ_2'
k_1''	λ_1'', γ_1''	λ_2'', γ_2''

where:

$m_1 = 0.15$ kg; $m_2 = 0.3$ kg, $k_1' = 4500$ N·m^{-1}; $k_1'' = 7500$ N·m^{-1}; $a = 0{,}03$ m.

The results are given in figures Fig. 2 – Fig. 10.

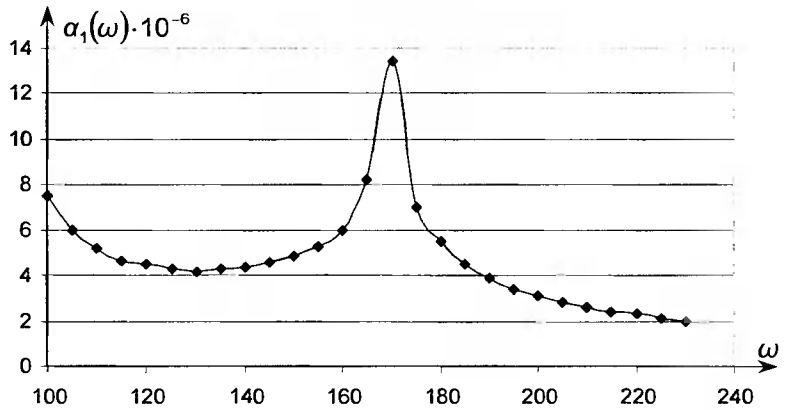

Fig. 2. Foundation dynamic receptance $\alpha_1(\omega)$

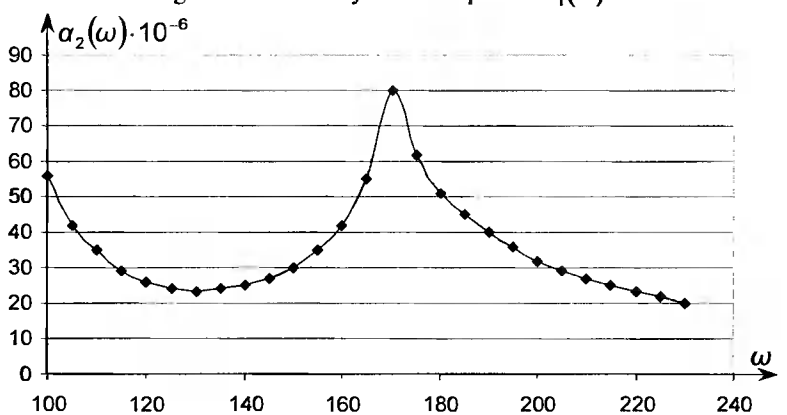

Fig. 3. Foundation dynamic receptance $\alpha_2(\omega)$

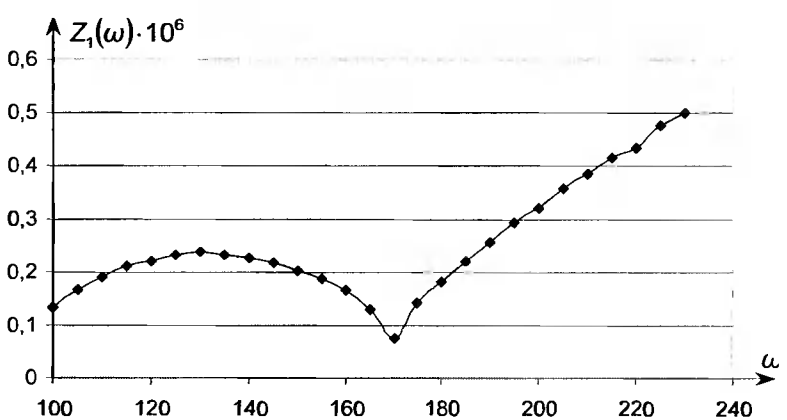

Fig. 4. Foundation dynamic stiffness $Z_1(\omega)$

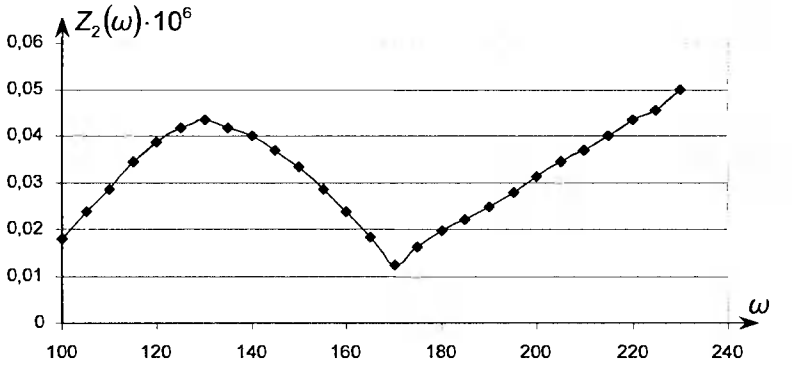

Fig. 5. Foundation dynamic receptance $Z_2(\omega)$

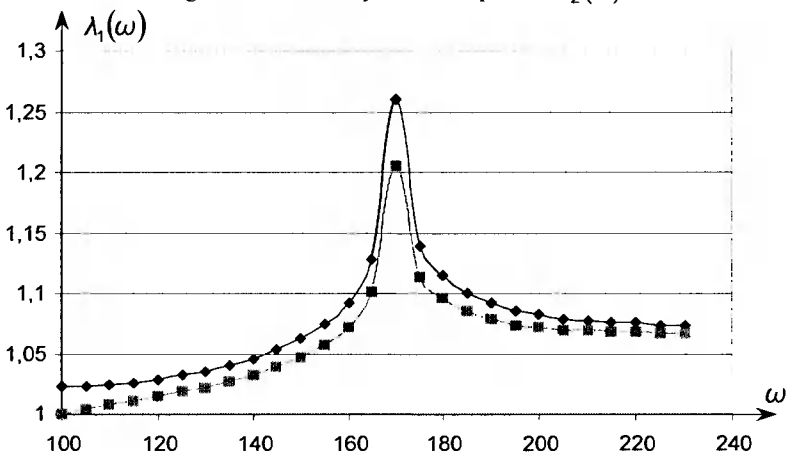

Fig. 6. Coefficients $\lambda'_1(\omega)$ and $\lambda''_1(\omega)$

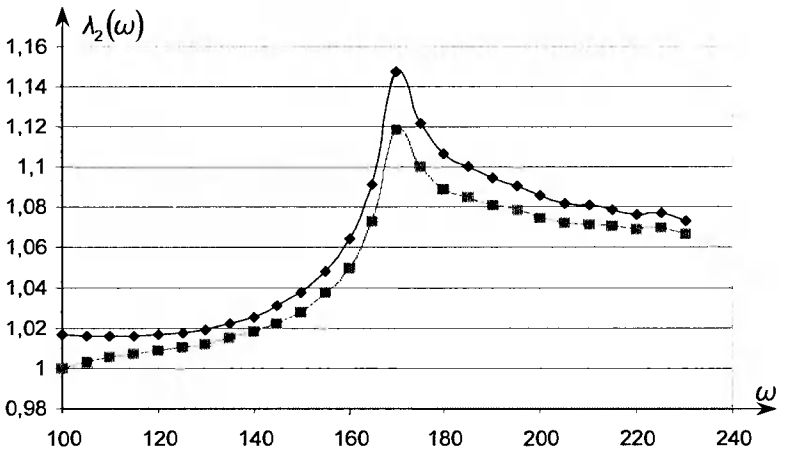

Fig. 7. Coefficients $\lambda'_2(\omega)$ and $\lambda''_2(\omega)$

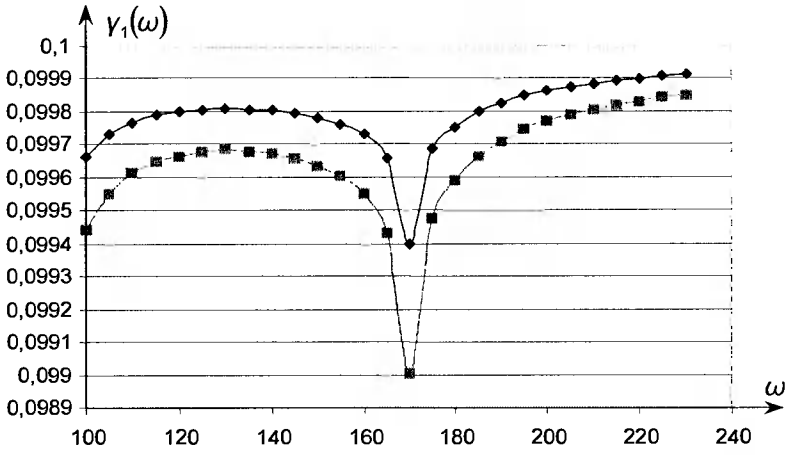

Fig. 8. Coefficients $\gamma_1'(\omega)$ and $\gamma_1''(\omega)$

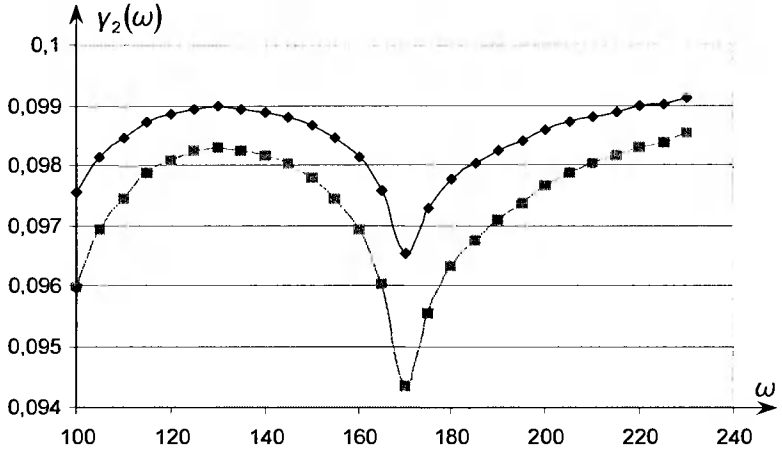

Fig. 9. Coefficients $\gamma_2'(\omega)$ and $\gamma_2''(\omega)$

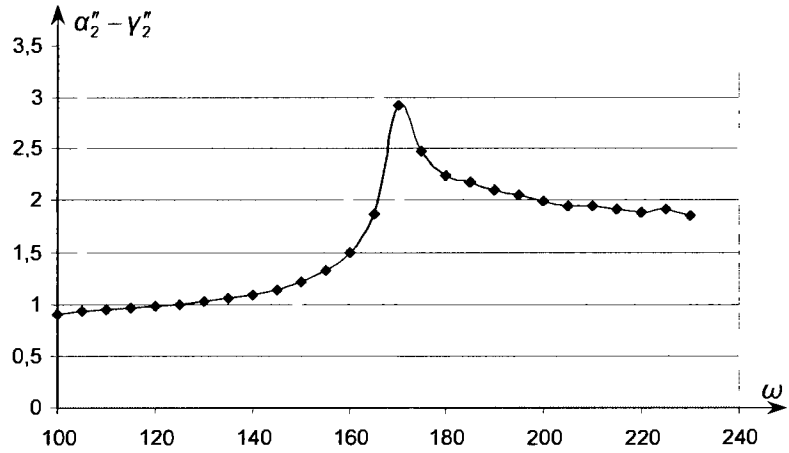

Fig. 10. Coefficients difference $\alpha_2'' - \gamma_2''$

4. CONCLUSIONS

When designing dynamic systems, founded on flexible foundation, the effect of the foundation can be very essential.
Sensitivity of the system to cam follower resonance frequency is low.
Effect of the flexible support is considerable when the system operates in the range of its resonance frequency.

REFERENCES

[1] Uhl T., 1977. Wspomaganie komputerowe CAD, CAM. WNT Warszawa.
[2] Awrejcewicz J., 2000. Drgania układów ciągłych. WNT Warszawa.
[3] Bishop R.E.W., 1972. Macierzowa analiza drgań. WNT Warszawa.

Review by prof. Franciszek Siemieniako

University Press
University
of Technology
and Agriculture
in Bydgoszcz

DEVELOPMENTS IN MACHINERY DESIGN AND CONTROL
Vol. 4 (2005) 51 – 56
Scientific Journal

Wojciech Korpal[1], Wojciech Weiner

University of Technology and Agriculture. Faculty of Technology and Chemical Engineering
85-326 Bydgoszcz, Seminaryjna 3, Poland

MULTILEVEL VIBRATION SIFTER

Abstract: The paper presents a multilevel vibration sifter concept and design. It shows a long spiral path of the material in the sieve from the central batch to the chute. A comparative study of the sifting process, operation time and effectiveness are reported. The sifter design has been implemented in the production process.

Keywords: sifter, sifting, grain motion on the sifter

1. INTRODUCTION

Operations involving loose and grain products often require dividing the material into fractions. Contemporary sifters show stable characteristics, are usually large in size and are difficult to operate.

The present paper provides analysis of most common solutions as were as presents a new sifter design.

2. DESIGN OF THE NEW SIFTER

Fig. 1 shows the cross-section of the new type of vibration sifter.

The device consists of cylindrical sieve segments positioned vertically. The lowest segment is located on the base with pneumatic suspension. Each sieve segment includes the housing with grain or loose material chute, sieve and a perforated element. Cleaning elements can be placed between the perforated element and the sieve. A lower conical part of each segment ends up with grain or loose material chute of a lower segment.

The drive can be equipped with the following drives:

- engine placed centrally in a lower segment with unbalanced masses,
- pair of vibrators placed on one of the segments.

The power of the engine, vibrators and degree of unbalancing can be chosen in a wide range. The pneumatic suspension with changeable characteristics is essential for this new solution. The suspension can be made as toroidal element or as multi-chamber group of elements of different shape, e.g. spherical.

A wide range of practicable drives and suspensions allows for the most adequate selection of parameters of sifter, depending on the specific needs.

---

[1]Corresponding author. *Tel.:* +48-52-374-90-56; *fax:* +48-52-374-90-05
E-mail address: korpal@atr.bydgoszcz.pl (W. Korpal)

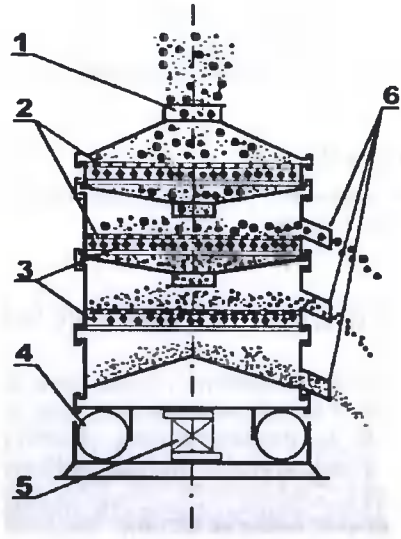

Fig. 1. New sifter design: 1 – batch, 2 – sifts, 3 – cleaning elements, 4 – engine mounting, 5 – engine, 6 – grain or loose material chute

The movement of the sifter can be horizontal and vertical. It can also make turns and swinging moves. The opportunity to affect the characteristics of the suspension makes an optimal selection of respective movement components possible, e.g. an opportunity to eliminate the vertical component.

Thanks to the compact design, the sifter can be also used for separating suspended matter.

The new sifter model on the research stand is given in Fig. 2.

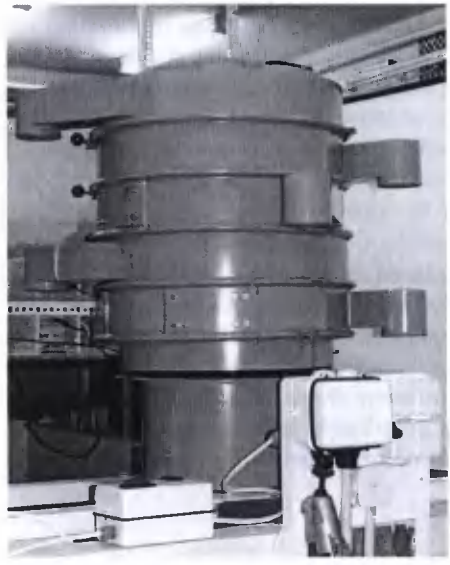

Fig. 2. Sifter model examined

3. RESEARCH PERFORMING

To perform the research, the research stand was made. An original research method was also developed. The special apparatus set based on laser and digital techniques was designed. The measurement method showed versatility and comprehensiveness of the results obtained.

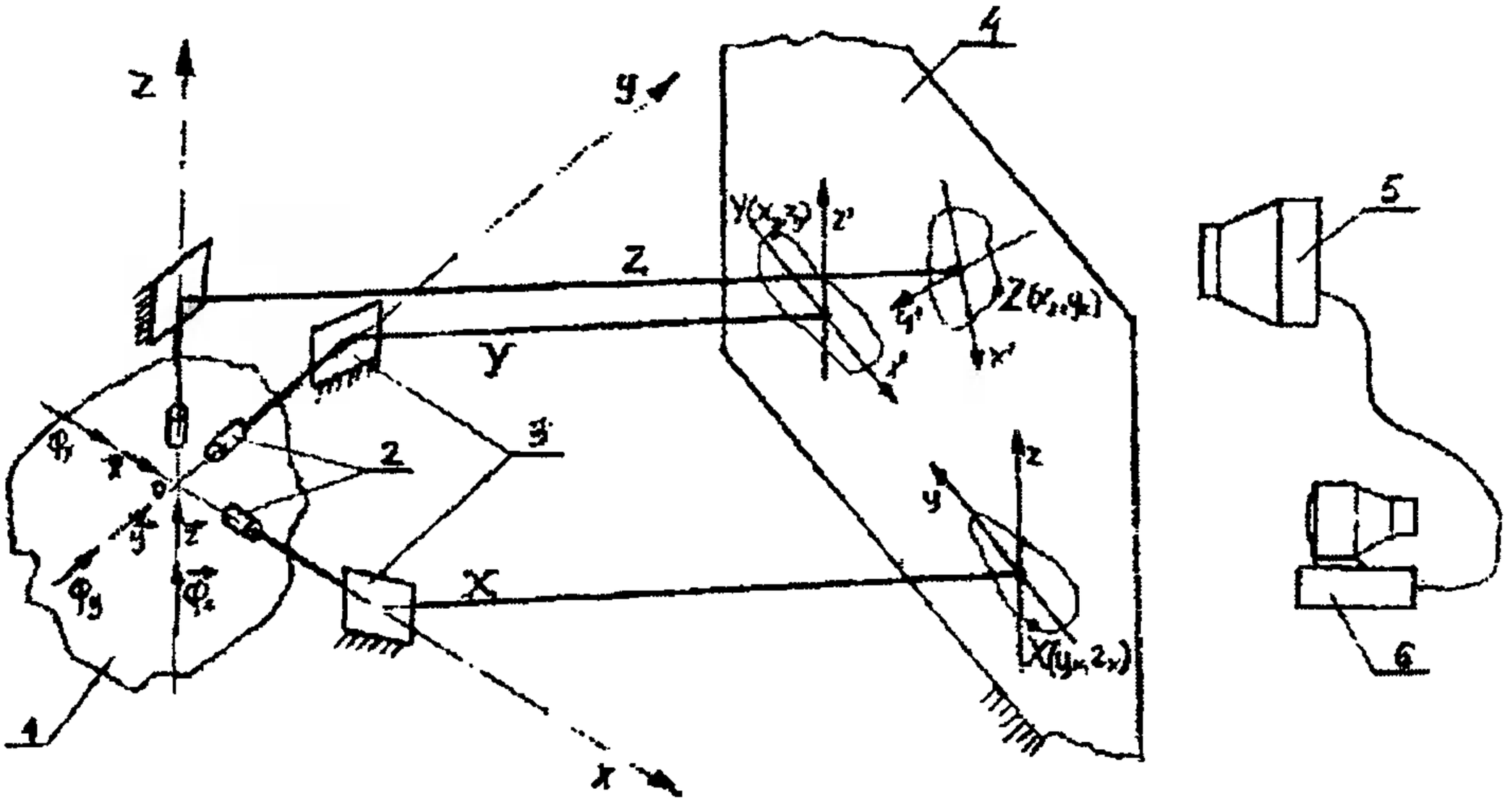

Fig. 3. Model to measure movement shifts using semiconductor laser diodes: 1 – sifter, 2 – laser diodes, 3 – mirrors, 4 – screen, 5 – camera, 6 – computer

The research of the grain movement on the sieve, was performed on the same research stand. The digital image of the movement captured was analyzed by computer, based on special computer software. The aim of this research was to develop a model of sifter operation which made it possible to simulate the choice of operation parameters, depending on specific conditions of the process and the raw material sifted. The method of sifter movement parameters measurement is based on a set of lasers, rays of which draw the curves on the screen which correspond to the relocation of axis of a selected coordinate system depending on the solid movement in the sifter.

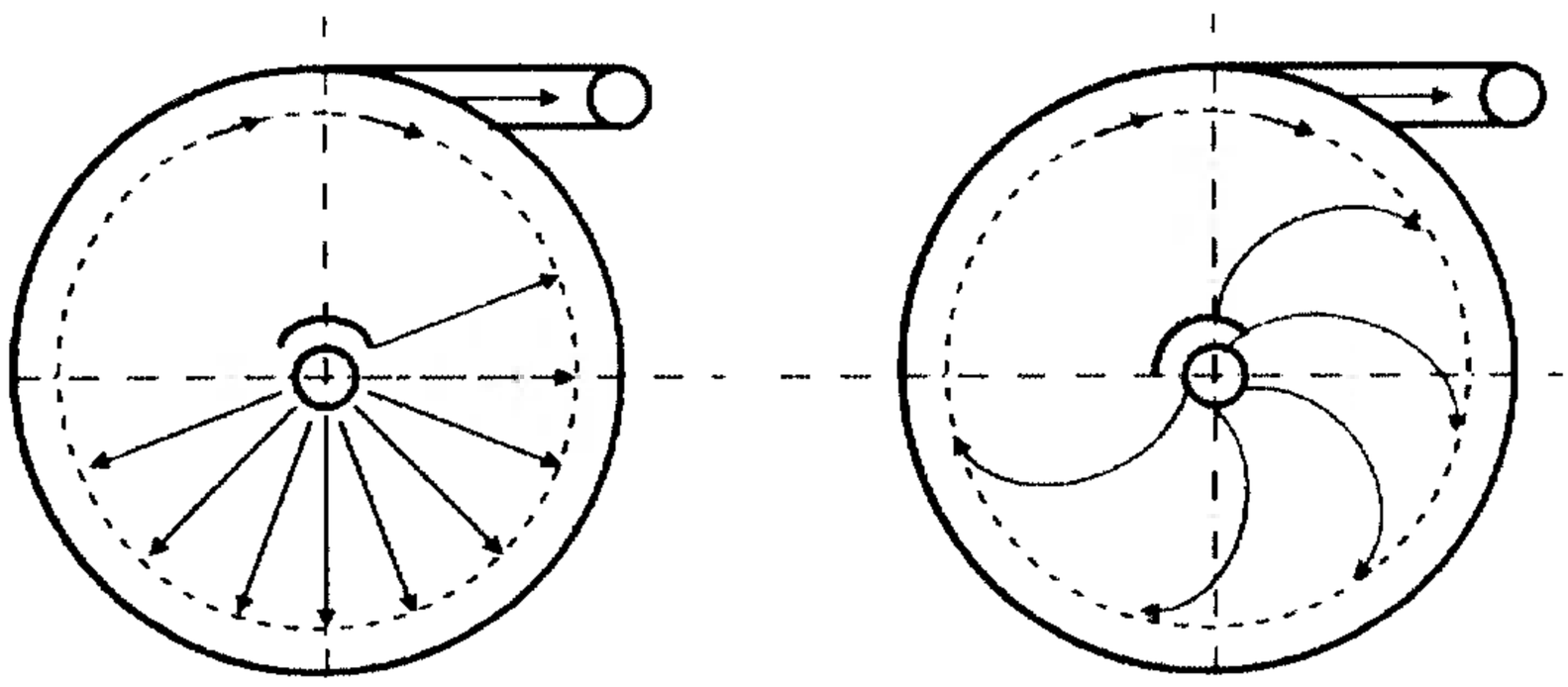

Fig. 4. Grain movement on the sieve

The results obtained allowed formulating assumptions to provide typical examples of dynamical relations in sifter, factoring in the design details, maintenance and ergonomics.

The aim of this research stage researches was to obtaining centrifugally-circumferential movement of the material, from the central batch to the chute placed tangential to the circuit. The movement on the spiral seems to be most advantageous. The research on the movement of the material on the sieve was performed on a special shield with a net of polar coordinates.

Figs 4 and 5 present expected and performed raw material movement on the sifter.

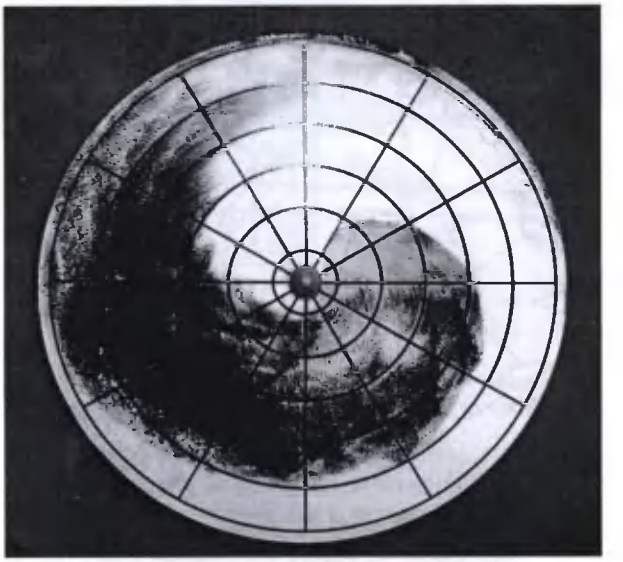

Fig. 5. Real movement of the material sifted

To facilitate movement of the grain special grain guides were used on chute cones (Fig. 6).

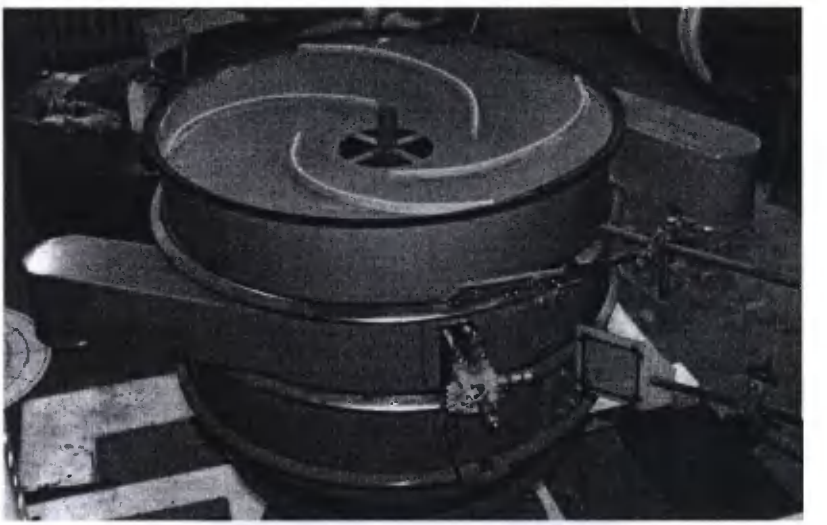

Fig. 6. Grain guides were used on chute cones

Table 1. Sifting effectiveness and productivity

Sample number	Sample kind	Sample sifting time [s]	Content of impurities			Mean impurities share [%]	Instantaneous productivity [kg/s]	Mean productivity [kg/s]
			initial [g]	during sifting [g]	share [%]			
1	Radial motion	380	5005	4760	95.1	94 2	0.132	0.135
2	Radial motion	373	5007	4690	93.7		0.134	
3	Radial motion	363	5002	4695	93.9		0.139	
4	Spiral motion	415	5001	4989	99.8	99.3	0.119	0.119
5	Spiral motion	421	5004	4944	98.8		0.119	
6	Spiral motion	427	5003	4967	99.3		0.118	
7	Double radial motion	748	5002	4990	99.8	99.4	0 067	0.067
8	Double radial motion	761	5006	4985	99.6		0.066	
9	Double radial motion	731	5004	4949	98 9		0.069	

4. TESTS PERFORMED

To verify the concept presented, tests were performed involving specially prepared mixture with 90% wheat grain and 10% 'impurities' in a form of rape grain.

The effectiveness and sifting time were evaluated at different sifter settings (radial and spiral movements of the raw material on the sifter). The velocity of the charge input was controlled to ensure that a layer of grains 10 mm thick remained directly under the charge input on the sifter. The time till the last grains left the sifter was measured. Then rape grains were weighed, evaluating the mixture separation effectiveness.

The weight of the samples sifted was 50 kg each (45 kg of wheat and 5 kg of rape). The results are given in Table 1.

As a result of the tests, a considerably higher sifting effectiveness was observed for forced spiral raw material motion on the sifter (99.3%), as compared with the radial motion (94.2%). It comes from a much longer path of single grains on the sifter. However, it is connected with an about 12% decrease in the process productivity.

Applying the radial motion of the sifted mixture, a comparable effectiveness was recorded after a double sifting.

5. CONCLUSIONS

The state of the art suggests the following conclusions:

- the angle of setting the power unit affects the kind of movement on sieves and effectiveness of the process itself,
- the new sifter design facilitates dividing different loose materials,
- the new device offers a wide range of flexibility of movement components,
- the sifter designed is simpler and more compact, as well as cheaper than those currently used,
- due to its compactness, the device can be used for dividing suspensions.

REFERENCES

[1] Błasiński H., 1988. Maszyny i aparatura technologiczna przemysłu spożywczego. Wyd. Politechniki Łódzkiej Łódź.
[2] Grochowicz J., 1994. Maszyny do czyszczenia i sortowania ziarna. WAR Lublin.
[3] Wodziński P., 1994. Przesiewanie, przesiewacze. Wyd. Politechniki Łódzkiej Łódź.
[4] Patent P-334105. Urząd Patentowy RP.

Review by prof. Józef Grochowicz

University Press
University
of Technology
and Agriculture
in Bydgoszcz

DEVELOPMENTS IN MACHINERY DESIGN AND CONTROL
Vol. 4 (2005) 57 – 66
Scientific Journal

Zbigniew Kuszyński, Kazimierz Peszyński[1]
University of Technology and Agriculture, Department of Control and Machinery Design
ul. Prof. S. Kaliskiego 7, 85–791 Bydgoszcz, Poland

MODELING SELECTED RESISTANCE ELEMENTS OF THE PNEUMATIC SUSPENSION SYSTEM

Abstract: The paper presents the pneumatic suspension system modeling. The preliminary analysis was based on the basic module which consists of the flexible and stiff vessels. Further an analysis is provided, defining the energy losses due to constant resistance. It is through that resistance that the flow between the two vessels occurs. Additionally an experimental identification method of more complex pneumatic resistance properties has been developed.

Keywords: pneumatic suspension, pneumatic resistance, modeling

1. INTRODUCTION

The aim of the present paper was to determine the operation properties of typical elements of the pneumatic suspension system of the carriage from the point of view of its mathematical model. Finally the authors intended to build the suspension system model based on the theory of pneumatic cascades [5]. The basic parameter of the pneumatic cascade is the resistance of input pipe and the vessel volume. The present paper covers methods of determining the resistance of typical elements of the suspension system being an unknown element of the pneumatic cascade. Based on the required properties of the cascades and the knowledge of the resistance, one can select an appropriate volume of the cascade vessel, which will ensure correct dynamic properties of the suspension system.

A typical basic suspension system module consists of pneumatic spring and leveling valve [1]. Two such modules form a typical set of accessories of bogies. They are joined to each other with a double non-return valve which protects against excessive pressure differences in pneumatic springs matting with each other, located transverse symmetrically to the carriage axis. Suspension deflection results in a decreased distance between the mounting points, which causes a turn of control lever and opening the flow between the supply vessel and the pneumatic spring. It allows for filling the two chamber cascade with air, and the lifting the carriage body until the distance between the upper and the lower mounting points returns to the reference value. If the distance between the mounting points increases (a decreased carriage load), than the control lever turns in the opposite direction and the pneumatic spring is connected with the surroundings and, as a result, empting the air from the chamber cascade, which lasts

[1] Corresponding author. *Tel.* +48-52-340-8238; *fax:* +48-52-340-8245
E-mail address: peszyn@atr.bydgoszcz.pl (K. Peszyński)

until the distance between the mounting points returns to the reference value. It is the so-called compensation system at the constant height.

The application of the control system results not only in a return to reference height of the carriage body but also a change in the amount of the air accumulated in the spring, and thus a change in the spring stiffness practically proportionally to the carriage body weight. It means that control system adjusts the spring properties in such a way that a change in the carriage body weight does not result in a change in self-frequency of the system. It is a very important advantage of pneumatic suspensions. However it makes it impossible to define the spring characteristics in a traditional way as a ratio of the acting force to the deflection caused by it.

The characteristics of the pneumatic springs is a function defining the relationship between the forces acting at the spring ends (at the axial loads) and the pressure in flexible chamber and its active area.

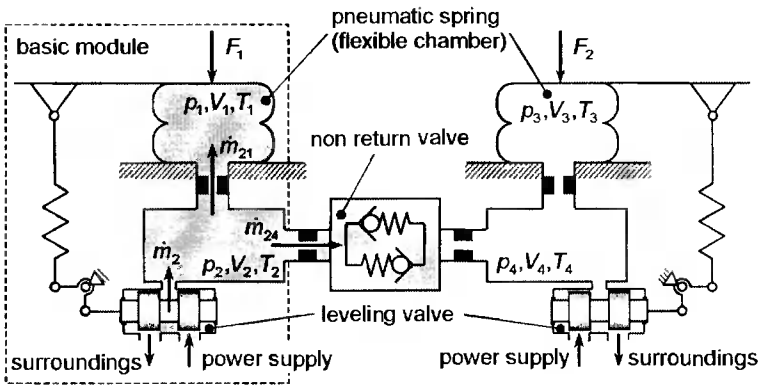

Fig. 1. Basic modules of pneumatic suspension system

In simple cases of load and deflection of the chamber according to its axis of symmetry (with the assumption that the flexible chamber is axi-symmetric), the equation of forces equilibrium assumes the form of:

$$F_1 = \frac{\pi}{4} D_e^2 (p_1 - p_0) \tag{1}$$

where: D_e – the active (effective) diameter of the flexible chamber determined by the parallel coordinate of the coating for which a condition is met that all the vectors of coating strain are parallel to the assumed cross-section,

p_1 – absolute air pressure in the pneumatic spring (in its flexible chamber),

p_o – atmospheric pressure.

Active diameter determines the so-called active (effective) area A_e of pneumatic spring:

$$A_e = \frac{\pi}{4} D_e^2 \tag{2}$$

The term of active (effective) area, in that sense, is frequently used in practice and in case of axi-symmetric loads, it allows defining the spring stiffness in this direction as a derivative of the force after displacement:

$$c_z = \frac{dF_1}{dz} = \frac{dp_1}{dz} A_e + (p_1 - p_o)\frac{dA_e}{dz} \tag{3}$$

If $A_2 = \text{const}$, then spring stiffness is as follows:

$$c_z = \frac{dp_1}{dz} A_e \tag{4}$$

In order to define the pressure derivative with respect to the axial deflection of flexible chamber of the spring, a polytropic change of state is assumed during a change in the volume and a constant air mass accumulated in the spring:

$$\frac{dp_1}{dz} = \frac{nA_e p_1}{V_1} \tag{5}$$

where: n – polytropic exponent,

V_1 – volume of flexible chamber.

If the system contains additional stiff chambers, the following applies:

$$c_z = \frac{nA_e p_1}{V_1 + \sum_{i=1}^{k} V_i} \tag{6}$$

where: V_i – volume of stiff chamber with index i,

k – number of stiff chambers connected with flexible chamber.

Equation (6) applies if we assume that the flow between chambers is non-restricted. In fact equation (6) determines static stiffness of the system in stable state because the actual stiffness depends also on pneumatic resistances between chambers. In the case analyzed, defining resistance between chambers 1 and 2 is possible based on the common formula (constant resistance). It is more difficult to determine the resistance between chamber 2 and chamber 4 due to its complicated structure.

2. MATHEMATICAL MODEL OF RESISTANCE BETWEEN CHAMBERS 1 AND 2

For the purpose of the theoretical analysis of flow phenomena in the resistance analyzed (Fig. 2), there was assumed a model of flow through pneumatic resistance given in Fig. 2. It was assumed that local losses are decisive. The assumption is justifiable in the cases of resistances of a sudden change in the cross-section whose length l does not exceed $10d_{min}$, where d_{min} is a minimum diameter of the resistance channel cross-section.

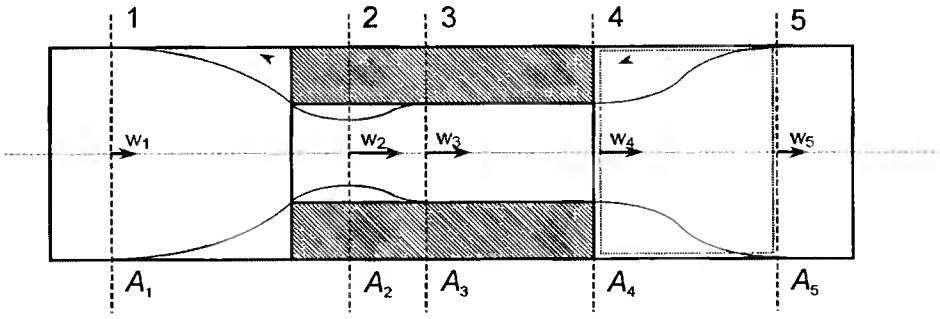

Fig. 2. Model of flow through pneumatic resistance

2.1. SUDDEN NARROWING OF THE CROSS-SECTION

Upon a sudden narrowing of the pipe cross-section, the stream gets narrow (accelerates) between cross-sections 1 and 2, and gets wider (decrease its velocity) between cross-sections 2 and 3. The cross-sections areas are, respectively, A_1, A_2, A_3.

Cross-section A_2, which is a consequence of fluid inertia, is referred to in Latin as 'vena contracta'. The losses during flow acceleration, namely the losses between cross-sections 1 and 2 are low and account for about 20% of the total losses which occur during the flow through the narrowing. The other 80% of losses which occur during late flow, namely between cross-section 2 and 3, can be calculated from the following formula:

$$p_{str2-3} = \frac{\rho(w_2 - w_3)^2}{2} \tag{7}$$

Velocity w_2 is not known but it can be calculated if we know the contraction coefficient μ, which is:

$$\mu = \frac{A_2}{A_3} = \frac{w_3}{w_2} \tag{8}$$

From formulas (7) and (8) we can obtain the following:

$$p_{str2-3} = \left(\frac{1}{\mu} - 1\right)^2 \frac{\rho {w_3}^2}{2} = \zeta_{2-3} \frac{\rho w_3^2}{2} \tag{9}$$

where $\zeta_{2-3} = \left(\frac{1}{\mu} - 1\right)^2$ is local loss coefficient.

Coefficient ζ_{2-3} can be calculated if we know the contraction coefficient μ.

Losses between cross-sections 1 and 2 can be expressed with the general formula:

$$p_{str1-2} = \zeta_{1-2} \frac{\rho w_2^2}{2} \tag{10}$$

The total losses between cross-sections 1 and 3 are obtained from equations (9) and (10)

$$p_{str1-3} = \zeta_{1-2} \frac{\rho w_2^2}{2} + \left(\frac{1}{\mu} - 1\right)^2 \frac{\rho {w_3}^2}{2} = \left[\frac{\zeta_{1-2}}{\mu^2} + \left(\frac{1}{\mu} - 1\right)^2\right] \frac{\rho w_3^2}{2} \tag{11}$$

Losses p_{str1-3} can be expressed as follows:

$$p_{str1-3} = \zeta_{1-3} \frac{\rho w_3^2}{2} \tag{12}$$

From equations (11) and (12) we can obtain:

$$\zeta_{1-3} = \frac{\zeta_{1-2}}{\mu^2} + \left(\frac{1}{\mu} - 1\right)^2 \tag{13}$$

From the experiments conducted for Reynolds' high numbers [4] we can see that coefficients μ and ζ_{1-3} do not depend on Re, however they depend on the ratio of cross-sections A_3 / A_1. In the special case when the fluid flows through the pipe from a big vessel, namely when $A_3 / A_1 \approx 0$, the experiments show that $\mu = 0.617$, $\zeta_{1-3} = 0.5$, and $\zeta_{1-2} = 0.04$. By substituting these values to equation (13) $\zeta_{1-3} \approx 0.105073 + 0.385325 \approx 0.5$ to equation (13) one can observe that the first part is slightly over 20% of the value of ζ_{1-3}, which confirms the data given above.

Applying the equation (13) is more difficult as ζ_{1-2} and μ must be known. In practice, a simplified formula is used:

$$\zeta_{1-3} = 0.5\left(1 - \frac{A_3}{A_1}\right) \tag{14}$$

2.2. SUDDEN ENLARGEMENT OF THE CROSS-SECTION

The considerations have been based on the assumption that there are no pressure losses due to friction (much lower than the local losses). The stream does not change it cross-section suddenly, and so from both sides of line 4 approximately static pressure p_4 applies. In cross-section 5 static pressure p_5 occurs, however with no loses, there would be static pressure p_5'.

The pressure p_{str} is only a local loss. Theoretically determining this loss is possible using equations of motion, Bernoulli equation, and continuity of flow. Assuming that even velocity fields w_4 and w_5 in each cross-section 4 and 5, based on the equation of motion (momentum conservation) for the control area determined with the rectangle between lines 4 and 5, Fig. 2, we can formulate:

$$\dot{m}(w_4 - w_5) = A_4(p_5 - p_4) \tag{15}$$

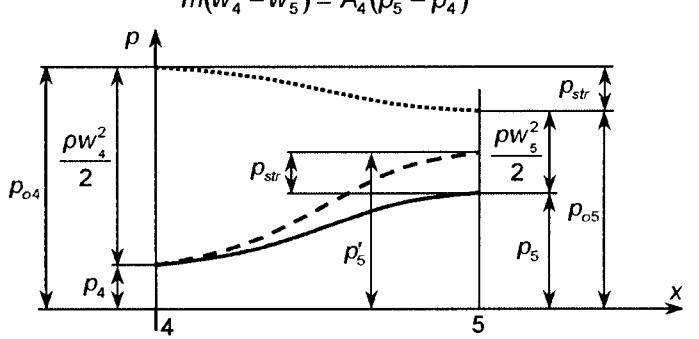

Fig. 3. Sudden enlargement of the cross-section – assumed pressure distribution

Bernoulli equation, considering the pressure loss p_{str}, assumes the following form, according to Fig. 3:

$$p_{o4} = p_{o5} + p_{str} \tag{16}$$

or

$$\frac{\rho w_4^2}{2} + p_4 = \frac{\rho w_5^2}{2} + p_5 + p_{str} \tag{17}$$

Equation of continuity is as follows:

$$\dot{m} = \rho w_4 A_4 = \rho w_5 A_5 \tag{18}$$

Having derived p_{str} from equation (17) and substituted (15) and (18), we obtain, known from literature, Borda-Carnot theorem:

$$p_{str} = \frac{\rho(w_4 - w_5)^2}{2} \tag{19}$$

Applying the equation of flow continuity (18), two corresponding notations can be obtained:

$$p_{str} = \left(1 - \frac{A_4}{A_5}\right)^2 \frac{\rho w_4^2}{2} \text{ or } p_{str} = \left(\frac{A_4}{A_5} - 1\right)^2 \frac{\rho w_5^2}{2} \tag{20}$$

As it is seen, the coefficients of local losses upon a sudden enlargement of the pneumatic channel cross-section (output from the pneumatic resistance) are:

$$\zeta_4 = \left(1 - \frac{A_4}{A_5}\right)^2 \text{ or } \zeta_5 = \left(\frac{A_4}{A_5} - 1\right)^2 \tag{21}$$

2.3. TOTAL LOSSES

Total losses, considering input and output losses due to pneumatic resistance, assuming that $w_3 = w_4$ and having omitted friction losses (low length of pneumatic resistance), can be calculated from the following formula:

$$\zeta_{1-5} = \frac{\zeta_{1-2}}{\mu^2} + \left(\frac{1}{\mu} - 1\right)^2 + \zeta_4 \tag{22}$$

or a simplified formula, assuming that $A_3 = A_4$:

$$\zeta_{1-5} = 0.5\left(1 - \frac{A_3}{A_1}\right) + \left(1 - \frac{A_3}{A_5}\right)^2 \tag{23}$$

If $A_1 = A_5$ (resistance shape compliant with the model given in Fig. 2), we obtain:

$$\zeta_{op} = \zeta_{1-5} = 1.5 - 2.5\frac{A_3}{A_1} + \frac{A_3^2}{A_1^2} \tag{24}$$

3. FLOW THROUGH THE DOUBLE NON-RETURN VALVE

The double non-return valve, connecting two stiff vessels (vessels 2 and 4 in Fig. 1) of the suspension system, has a relatively complex internal structure [2]. There occur a flow through the narrowing, flow around the sphere and the flow around the spring. Analytic modeling, even when based on simplified formulae, results in a very complex

model which would be almost inapplicable in practice. For that reason in that case, the properties identification method was applied based on experiments. The flow characteristics of this valve are strongly non-linear.

A special stand, which was a closed system based on the flow balance in the double vessel system with a valve, has been developed for this purpose.

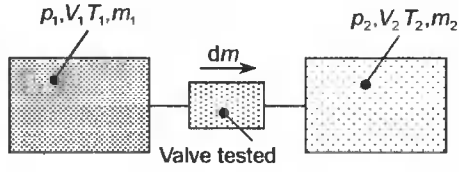

Fig. 4. Working diagram for theoretical analysis

The theoretical analysis of the system tested is based on the assumption that during examinations the system is hermetic and so the mass of the air contained in both pressure vessels, connecting pipes, and the valve is constant, which can be expressed with the following equation:

$$m_1 + m_2 = const \tag{25}$$

where: m_1 – the total mass of the air in the left vessel together with the accessories,

m_2 – the total mass of the air in the right vessel together with the accessories,

which after differentiating of both equation sides, becomes:

$$\mathrm{d}m_1 + \mathrm{d}m_2 = 0 \tag{26}$$

Equation (26) is, in fact, the law of conservation of mass in differential form, concerning the system examined.

Mass of the air $m_i \ \ (i = 1,\ 2)$, in the vessels is defined with the Clapeyron equation:

$$p_i V_i = m_i R_i' \mathrm{T}_i, \ \ i = 1,\ 2 \tag{27}$$

where: $p\ [\mathrm{Pa}]$ – pressure in the vessel, $V\left[\mathrm{m}^3\right]$ – vessel volume, $T\ [\mathrm{K}]$ temperature in the vessel, $R' = 287\ \mathrm{J/(kg \cdot K)}$ air gas constant.

In further analysis a simplified assumption was made that the values of thermodynamic properties V_i, R_i', T_i in both vessels are constant.

Hence

$$\mathrm{d}m_i = \frac{V_i}{R_i T_i}\mathrm{d}p_i, \ \ i = 1,\ 2 \tag{28}$$

After substituting equation (28) into equation (26), we obtain:

$$\frac{V_1}{R_1 T_1}\mathrm{d}p_1 = -\frac{V_2}{R_2 T_2}\mathrm{d}p_2 \tag{29}$$

Equation (29) proves that pressure changes in respective vessels are symmetrical.

If we consider time interval $\langle t_i, t_{i+1}\rangle$, then the ratio mass change Δm in a vessel to time interval Δt_i gives the mean flow rate Q_m:

$$Q_m = \frac{m_{i+1} - m_i}{t_{i+1} - t_i} \tag{30}$$

The vessel air mass is defined with:

$$m = \frac{V}{R'T}(p_i + p_{atm}) \tag{31}$$

With the spreadsheet, it is possible to define the characteristics in question.

Test stand

The test stand was developed based on two air vessels between which the component examined was placed. Each vessel can be supplied with the compressed air.

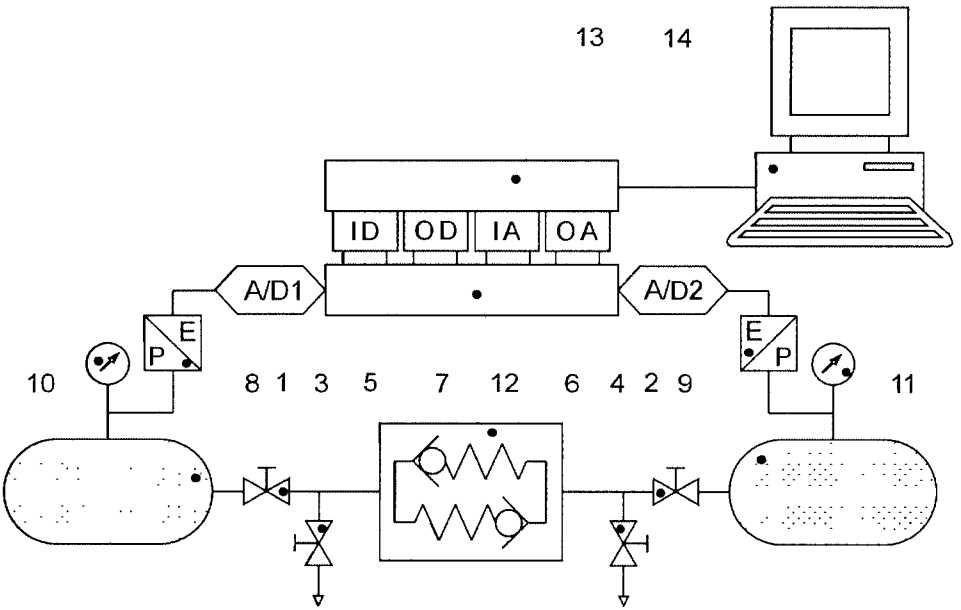

Fig. 5. Test stand diagram

1, 2 – pressure vessel, 0,24 m^3 each,
3, 4 – cut-off valve,
5, 6 – release valve,
7 – component examined, here double non-return valve,
8, 9 - pressure transducer,
10, 11 – precise measurement manometer,
Data acquisition equipment
12 – PCLD – 87 10 Terminal Wiring Board by Advantech
13 – PCI –1710 series 12/16 Multifunction CARD
14 – Personal computer with software Geni DAQ and Excel spreadsheet
ID - digital input, OD – digital output, IA – analogue input, OA – analogue output

Measurements results

The research concerned the double non-return valve given in Fig. 1, since the properties of rail-bus moving along the curved railway track and in case of uneven distribution of load depend on the valve parameters.

The pressure drops were measured in vessels for the flow from vessel no 1 to vessel no 2 (left chart in Fig. 6) and from 2 to 1 (right chart in Fig. 6).

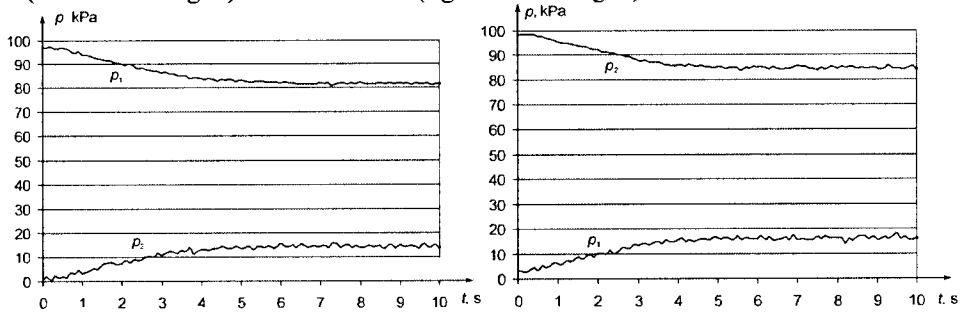

Fig. 6. Pressure in vessels during air flow measurements: left chart – from 1 to 2; right chart from 2 to 1

The results indicate that the equipment measured shows a considerable symmetry, although, as compared to the flow lock-pressure expected ($p_{lock} = 0.69$ kPa), it is too low, as it is about $p_{lock1} = 0.65$ kPa for the flow $1 \rightarrow 2$, and $p_{lock1} = 0.67$ kPa for the flow $2 \rightarrow 1$.

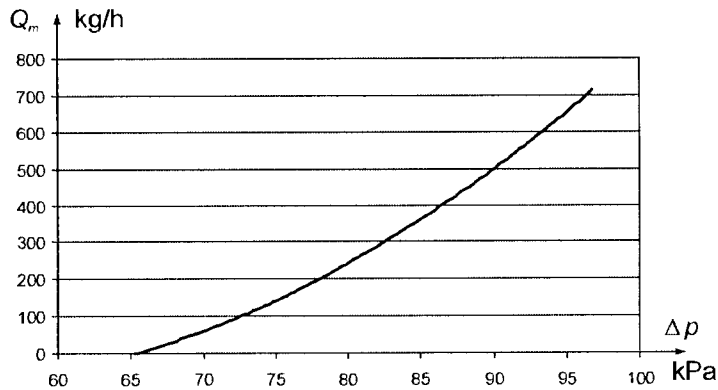

Fig. 7. Valve flow characteristic calculated based on the results given in Fig. 6

4. CONCLUSIONS

The two types of defining pneumatic resistance properties give approximate results, and they cannot compete with the models of defining characteristics known from literature, as far as the accuracy is concerned, however they are much more simple. They allow for a quick determination of properties at sufficient accuracy using analytical or experimental methods. Such an identification is sufficient in automatic control systems in which only the order of magnitude of model parameters is required.

Additionally there is need for the analysis of the third pneumatic resistance connected with the stiff vessel, supply valve, which will be non-linear characteristic with zone of insensitivity.

REFERENCES

[1] Grajner J., 1996. Podstawy teoretyczno-doświadczalne projektowania zawieszeń pneumatycznych. Oficyna Wydawnicza Politechniki Wrocławskiej Wrocław.
[2] Kuszyński Z., Peszyński K., 2005. Identyfikacja wybranych elementów pneumatycznego układu zawieszenia wagonu. Międzynarodowa konf. nauk. tech. Napędy i Sterowania Hydrauliczne i Pneumatyczne '2005, Wrocław, 358-365.
[3] Kuszyński Z., Peszyński K., 2005. Modelowanie i weryfikacja obiektu pneumatycznego trójzbiornikowego. IX seminarium nauk. Postępy w Konstrukcji i Sterowaniu, Bydgoszcz – Muszyna, Book of Extended Abstracts 7, 51-52 (pełen tekst załączony do zbioru streszczeń na CD ROM).
[4] Orzechowski Z., Prywer J., Zarzycki J., 1997. Mechanika płynów w inżynierii środowiska. WNT Warszawa.
[5] Tarnowski W., Bartkiewicz S., 2003. Modelowanie matematyczne i symulacja komputerowa dynamicznych procesów ciągłych. Wyd. Uczeln. Politechniki Koszalińskiej Koszalin.

Review by prof. Jerzy Iwaszko

University Press
University
of Technology
and Agriculture
in Bydgoszcz

DEVELOPMENTS IN MACHINERY DESIGN AND CONTROL
Vol. 4 (2005) 67 – 74
Scientific Journal

Bogdan Landowski[1], **Maciej Woropay**
University of Technology and Agriculture, Department of Machine Maintenance
ul. Prof. S. Kaliskiego 7, 85–791 Bydgoszcz, Poland

CONTROL OF THE RESERVE SUBSYSTEM BASED ON THE RESULTS FROM MODEL INVESTIGATIONS OF THE TECHNICAL OBJECTS RESERVE PROCESS

Abstract: The way to determine probabilities that the technical objects are available at a reserve subsystem at the certain time moment, presented in the paper, makes it possible to determine the indispensable number of the reserve objects for the adopted risk criterion of 'using up the reserve'. This enables to control the reserve subsystem based on the determined subsystem state prognosis. All the considerations are illustrated by means of municipal bus transport utilization and maintenance system. A calculation was carried out for the assumptions made and indispensable (as far as the adapted criterion is concerned) number of reserve subsystem elements was determined. The paper does not include economic aspects to keep the reserve subsystem.

Keywords: reservation process model, municipal bus transport system, reserve subsystem, homogenous Markov process

1. INTRODUCTION

For the complex systems of utilization and maintenance of the technical objects, where there is a necessity to ensure continuous execution of the system tasks (e.g. power supply systems, transport systems, etc.), it is indispensable to maintain a reserve subsystem including k of the reserve objects.

In some systems, in case a certain object gets damaged, it is required to substitute it immediately with a suitable, from technical point of view, object that is kept as a reserve. An example of such a system is municipal bus transport utilization and maintenance system. In order to ensure continuous execution of transport tasks, reserve vehicles are used and perform transport tasks when the primary vehicles got damaged.

A significant problem is to rationally control the subsystem of reserving the technical objects, and to specify an appropriate number of the reserve objects at the same time. Maintaining two numerous objects as reserve ones is uneconomical because of the expenses to purchase, keep, utilize and maintain the reserve objects.

This paper presents the way to evaluate (forecast) behavior of the reserve subsystem, assuming that the reservation process model is homogenous Markov process (birth and death process).

[1]Corresponding author. *Tel.:* +48-52-340-84-95; *fax:* +48-52-340-84-95
E-mail address: lbogdan@atr.bydgoszcz.pl (B. Landowski)

The presented way to determine probabilities that the technical objects are available at a reserve subsystem at the certain time moment makes it possible to determine the indispensable number of the reserve objects for the adopted risk criterion of 'using up the reserve'. This enables us to control the reserve subsystem, based on the determined subsystem state prognosis. All the considerations are illustrated by means of municipal bus transport utilization and maintenance system. A calculation was carried out for the assumptions made and indispensable (as far as the adapted criterion is concerned) number of reserve subsystem elements was determined. The paper does not include economic aspects to keep the reserve subsystem.

2. INVESTIGATION OBJECT

The investigation object, being the basis for the considerations presented in this paper is municipal bus transport utilization and maintenance system in a chosen urban agglomerate. The essential aim for the investigated system is to realize efficient and safe passenger transportation using the bus transportation means within the determined quantitative and territorial limits.

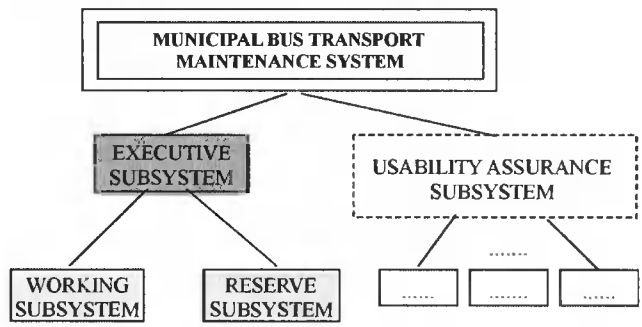

Fig. 1. Diagram of simplified structure of the analyzed municipal bus transport system

For this paper two main subsystems have been distinguished in the analyzed utilization and maintenance municipal bus transport system (Fig. 1):

- executive subsystem, composed of elementary subsystems (driver – bus), performing the main task of the system (passenger transportation);
- usability assurance subsystem, composed of its individual subsystems, in which diagnostic operations, servicing, repairs and the operations related to supplying elementary subsystems of the executive system are performed.

The executive subsystem comprises two subsystems:

- executive subsystem, including n elementary elements, being indispensable to perform the task,
- reserve subsystem, including k reserve elements.

The system tasks are directly realized by the executive subsystem comprising elementary subsystems of <H – TO> type (driver– bus), where a man is interlinked by serial structure with a technical object. Reliability of the utilized and maintained technical objects is kept at an appropriate level as a result of execution of the maintenance processes performed in the usability assurance subsystem.

A damaged bus, in the investigated utilization and maintenance system, is directed to the usability assurance subsystem, where it is a subject to the renovation (servicing) processes. If at a certain moment reserve vehicles are available in the reserve subsystem, then they are directed to the working subsystem, where they substitute the damaged vehicles. Because the buses got damaged at the random time moments, the service arrivals reach the usability assurance subsystem at the random time moments t_i. The service arrivals sequence (distributed in a determined way throughout the time) forms the so-called arrival stream. Having completed the servicing processes, the task-usable vehicle is directed to the executive subsystem (reserve or working one – if the number of the vehicles in the working subsystem is too small to execute completely the transportation tasks). The duration of vehicle servicing (time length when a vehicle stays in usability assurance system) is of a random nature. At a further stage of the investigations it was assumed that the objects utilized and maintained in the analyses system are homogenous (as far as the servicing process performed is concerned). The time needed to service a vehicle is a random variable (denoted with η symbol), distribution of which is equal for all the vehicles (service operations).

3. RESERVE PROCESS MODEL

If from the renovation point of view the only important factor is whether arrival occurs or not at the certain moment in time (it is assumed that all the arrivals are equal for the usability assurance subsystem), then we face homogenous event stream [3]. In such a case each arrival is characterized by moment t_i, $t_1 > 0$, $j = 1, 2, \ldots, k$ when it appears in the system, and the arrival stream is determined by the moment sequence $t_1, t_2, ,$ or by a formula describing the moment order t_j.

In order to describe the arrival random stream, it is enough to determine the combined (multidimensional) distribution of the random variables $t_1, t_2, t_3, \ldots, t_k, \ldots$ Instead of variables t_j time ranges ξ_j between consecutive arrivals may be investigated:

$$\begin{aligned} t_1 &= \xi_1 \\ t_2 &= \xi_1 + \xi_2 \\ t_3 &= \xi_1 + \xi_2 + \xi_3 \\ &\ldots\ldots\ldots\ldots \\ t_k &= \xi_1 + \xi_2 + \xi_3 + \ldots + \xi_k \\ &\ldots\ldots\ldots\ldots \end{aligned} \tag{1}$$

The distribution of the random variables ξ_j may be determined by means of the following cumulative distribution functions:

$$F(z_1, z_2, \ldots, z_k) = P(\xi_1 < z_1, \xi_2 < z_2, \ldots, \xi_k < z_k) \text{ for } k \geq 1 \tag{2}$$

It was assumed that the random variables ξ_j representing the time between the consecutive arrivals of the damaged technical objects that reach the usability assurance subsystem are continuous variables and they may be described by the frequency

functions $f(z_1, z_2, ..., z_k)$ in the investigated utilization and maintenance system model.

At the further stage of the paper it was assumed that the arrival stream is a stationary stream, which means that:

$$f_2(z) = f_3(z) = ... = f_k(z) = f(z) \tag{3}$$

as well as that the probability that two or more arrivals occur at the certain moment in time t is so small that it may be omitted (normal stream), that means that:

$$\lim_{\Delta t \to 0} \frac{v(t, \Delta t)}{\Delta t} = 0 \text{ for } t \in R \tag{4}$$

where:

$v(t, \Delta t)$ – probability that two or more arrivals occur within the time range $(t, t+\Delta t)$.

Expected value of the variable ξ_j:

$$E\xi_j = \int_0^\infty z f(z) dz = u, \quad j > 1 \tag{5}$$

where:

$f(z)$ – random variable frequency function ξ_j,

is an average value of the time range length between the consecutive arrivals, however the parameter:

$$\lambda = \frac{1}{u} \tag{6}$$

represents an average number of the arrivals that occur at a time unit and it is called stream intensity.

Based on the performed identification of the investigation object and on the analyses of the results from the performed utilization and maintenance examinations, the following assumptions were made:

$$f(z) = \lambda e^{-\lambda z} \tag{7}$$

$$f_1(z) = f(z) \tag{8}$$

That means that the analyzed arrival stream is a Poisson's stream.

In order to describe the reservation process model, it was assumed that the service arrival stream (through the usability assurance subsystem) is the Poisson's stream with parameter λ and that the random variable η denoting arrival service time (time length when a vehicle stays in usability assurance system) is of exponential distribution nature with parameter μ.

The reserve subsystem state is denoted with E_n, $n = 0, 1, 2, ...,$ where n represents the number of the objects being in the reserve subsystem (reserve buses).

It was assumed that state changes E_n of the reserve subsystem (number of the objects available in the reserve subsystem) are described by homogenous Markov process $\{X(t), t \geq 0\}$. If $X(t) = k$ $(k = 0, 1, 2, ..., n)$, then at the moment t

the reserve subsystem state equals E_k (exactly k reserve elements is available in this subsystem). The states k of the process $\{X(t),\ t \geq 0\}$ correspond to the states E_k of the reserve subsystem. Possible transitions between process states $\{X(t),\ t \geq 0\}$ are presented in Fig. 2.

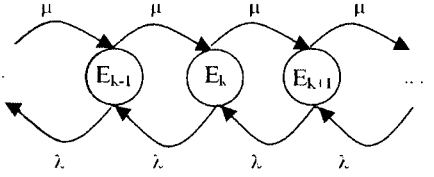

Fig. 2. Digraph representing the change process of the reserve subsystem state (of process $\{X(t),\ t \geq 0\}$)

In order to build transition intensity matrix between the process states $\{X(t),\ t \geq 0\}$ the change probabilities of the reserve subsystem state changes are analyzed. Assuming that exactly k objects are available in the reserve subsystem at the moment t (at the moment t the reserve subsystem state is state E_k) and that the reserve object immediately takes over the task of the damaged object of the working subsystem, the probability of reserve subsystem state change (within time length range Δt) from state E_k to state E_{k-1} may be described with the following formula:

$$P\{X(t+\Delta t) = k-1 \mid X(t) = k\} = \lambda \Delta t + o(\Delta t) \tag{9}$$

where:

λ – arrival stream intensity reaching usability assurance subsystem (intensity of 'leaving reserve state'),

$o(\Delta t)$ – any function that meets the condition $\lim_{\Delta t \to 0} \frac{o(\Delta t)}{\Delta t} = 0$.

State change of the reserve subsystem state E_k to state E_{k+1} (increasing the number of the objects in the reserve subsystem) may take place only if a technical object after completed renovation processes (of task usability state) is moved from usability assurance subsystem to the reserve subsystem. Probability of such an event is expressed by the following formula:

$$P\{X(t+\Delta t) = k+1 \mid X(t) = k\} = \mu \Delta t + o(\Delta t) \tag{10}$$

where:

μ - arrival stream intensity reaching usability assurance subsystem (intensity of 'entering reserve state'),

Moreover, the following assumptions were adopted:

$$P\{X(t+\Delta t) = k+i \mid X(t) = k\} = o(\Delta t) \quad \text{for } i \geq 0, \tag{11}$$

and

$$P\{X(t+\Delta t) = k-i \mid X(t) = k\} = o(\Delta t) \quad \text{for } i \geq 2 \tag{12}$$

The matrix of the process state change intensity $\{X(t), t \geq 0\}$ takes the following form:

$$\Lambda = \begin{bmatrix} -\mu & \mu & 0 & 0 & . & . & . \\ \lambda & -(\mu+\lambda) & \mu & 0 & . & & . \\ 0 & \lambda & -(\mu+\lambda) & \mu & . & & . \\ . & & & & & & . \\ . & & & & & & . \\ . & . & & & . & . & . \end{bmatrix} \tag{13}$$

The matrix form Λ allows us to state that the process $\{X(t),\ t \geq 0\}$ is a birth and death process [4, 5]. The parameter μ, in the model investigated (process), represents the intensity of birth (development), and λ represents intensity of death (vanishing).

In order to determine the probabilities that the process $\{X(t),\ t \geq 0\}$ at the certain moment in time t is in state k, building and solving Kolmogorov's system of differential equations based on matrix λ are needed.

By introducing the following symbols:

$$p_k(t) = P\{X(t) = k\}\ ,\quad k = 0,1,2,... \tag{14}$$

the Kolmogorov's differential equations take the following form:

$$\begin{aligned} p_0'(t) &= -\mu p_0(t) + \lambda p_1(t) \\ p_k'(t) &= \mu p_{k-1}(t) - (\lambda+\mu) p_k(t) + \lambda p_{k+1}(t) \text{ for } k = 1,2,3,... \end{aligned} \tag{15}$$

It is infinite system of differential equations. The system of equations (15) was solved when investigating service system of type M/M/1, and the way it had been solved was presented in the paper [2].

The solution of the system of equations (15) leads to the formulas that are expressed by generalized Bessel functions of I-st type. In order to get an unambiguous solution from the system of equations analyzed, initial conditions should be introduced, for instance:

$$p_k(0) = \begin{cases} 1, & \text{if } k = r \\ 0, & \text{if } k \neq r \end{cases}. \tag{16}$$

Then the solution of the system of equations (15) takes the following form:

$$p_k(t) = e^{-(\lambda+\mu)t}\left[\rho^{r-k} I_{k-r}(u) + \rho^{r-k+1} I_{k+r+1}(u) + \left(1 - \frac{1}{\rho^2}\right)\frac{1}{\rho^{2k}} \sum_{i=k+r+2}^{\infty} \rho^i I_i(u)\right] \tag{17}$$

where:

$$\rho = \sqrt{\frac{\lambda}{\mu}}$$

$$u = 2t\sqrt{\lambda\mu}$$

$I_s(u)$ is generalized Bessel function of the first type:

$$I_s(u) = \sum_{i=0}^{\infty} \frac{\left(\frac{u}{2}\right)^{s+2i}}{i!\Gamma(s+i+1)}. \tag{18}$$

In order to determine the indispensable number of the elements in the reserve subsystem, it was assumed that within the analyzed time range $t \in \langle 0, t_b \rangle$ the event probability that the reserve subsystem reaches state E_0 (number of the technical objects available in the reserve subsystem equals 0) must not exceed acceptable (by the decision makers of the utilization and maintenance system) risk level ε. Therefore, the risk criterion of 'using up the reserve' takes the following form:

$$p_o(t) < \varepsilon, \quad t \in \langle 0, t_b \rangle, \tag{19}$$

where:

ε – adopted risk level, $\varepsilon \geq 0$.

By solving the system of equations (15), it is possible to determine the indispensable number of the reserve elements for the adopted risk criterion. In order to solve the system of equations (15) a calculation algorithm was developed.

4. CALCULATION EXAMPLE

In order to illustrate the considerations, a calculation was made. It was assumed that the random variable η (time length when a vehicle stays in usability assurance system) is of exponential distribution nature with parameter μ. Based on the preliminary investigation results the values of the parameters μ $\mu = 0.658$ and λ $(\lambda = 0.725)$ were evaluated.

Assuming that the criterion of indispensable number of the reserve objects r is the inequality $p_0(t) \leq 0.05$ which is to be met for each moment in time t within the range $\langle 0, t_b \rangle$ (the time range of length 24 h, that means $t \in \langle 0, 24 \rangle$ is taken into consideration in the example), value r $(r = 10)$ has been determined for the adopted data.

One may state that for $r = 10$, the criterion analyzed is met. Fig. 3 shows the changes of the probability values $p_0(t)$ determined when assuming that at the initial moment $(t = 0)$ the number of the elements in the reserve subsystem equals $r = 10$.

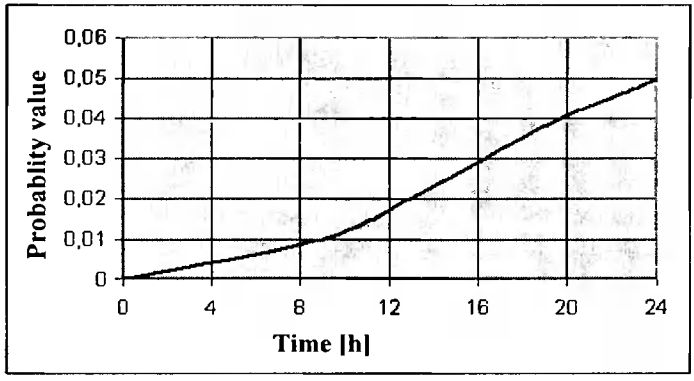

Fig. 3. Changes of the probability value p_0 in the time function for $r = 10$ $(\lambda = 0.725, \mu = 0.658)$

5. SUMMARY

A model was developed to give prognosis for the reserve subsystem state and to determine the number of the indispensable reserve objects (as far as the adopted risk level ε is concerned) to guarantee continuous execution of the tasks, assuming that in order to model technical object reservation process, the process of birth and death may be applied.

The paper determines temporary probabilities $p_k(t)$ representing probability of an event that k elements are available in the reserve subsystem.

It is needed to state that for the risk criterion of using up the reserve, adopted in the paper, evaluation of the limiting probabilities p_k^* ($p_k^* = \lim_{t\to\infty} p_k(t)$, $k = 0, 1, 2, \ldots$) does not allow us to determine the indispensable number of the reserve subsystem objects.

The investigation of the model presented in the paper allows us to obtain prognosis for the system behavior, which (for the real data obtained from the utilization and maintenance investigation results and after having verified the assumptions made) may be a significant piece of information for the decision-makers who control the analyzed utilization and maintenance system and the process executed within the system.

REFERENCES

[1] Bobrowski D., 1985. Modele i metody matematyczne teorii niezawodności w przykładach i zadaniach. WNT Warszawa.

[2] Bobrowski D., Maćkowiak-Łybacka K., 2001. Wybrane metody wnioskowania statystycznego. Wyd. V, Wyd. Politechniki Poznańskiej Poznań.

[3] Buslenko N., Kałasznikow W., Kowalenko I., 1979. Teoria systemów złożonych. PWN Warszawa.

[4] Knopik L., Landowski B., Perczyński D., 2002. Prognozowanie stanu systemu eksploatacji transformatorów rozdzielczych na podstawie badań modelowych. Zagadnienia Eksploatacji Maszyn 4(132), 163-175.

[5] Saaty T.L., 1971. Elementy teorii masowej obsługi i jej zastosowania. Sowietskoje Radio Moskwa.

[6] Sołowiew A.D., 1983. Analityczne metody w teorii niezawodności. WNT Warszawa.

Review by prof. Józef Żurek

University Press
University
of Technology
and Agriculture
in Bydgoszcz

DEVELOPMENTS IN MACHINERY DESIGN AND CONTROL
Vol. 4 (2005) 75 – 82
Scientific Journal

Tomasz Piątkowski[a)1], **Janusz Sempruch**[b)]

University of Technology and Agriculture
[a)]*Department of Postal Technology,* [b)]*Department of Control and Machinery Design*
ul. Prof. S. Kaliskiego 7, 85–791 Bydgoszcz, Poland

INELASTIC IMPACT PROBLEM OF ROUGH BODIES IN SORTING PROCESS OF UNIT LOADS STREAM

Abstract: The paper concerns modelling problem of the collision process of inelastic bodies in automatic sorting process of the unit load stream. In analytic description of the dynamic interactions between the load and the working elements of the sorting machine, a method in which the impact process is treated as a continuous process is proposed.

Keywords: unit loads, sorting process, impact phenomenon

1. INTRODUCTION

In the automatic sorting process of the unit loads stream realised by means of the rotary fence from the conveyor belts, the source of intensive dynamic interactions is the impact phenomenon that appears between the load and the fence. It is difficult to model and, first of all, it can have a destructive influence on the loads, and the construction elements of the divider. A high level of these interactions (among other things) is the result of applying divider devices in which the fence together with the driving system is a very stiff construction having very big mass of inertia. In the sorting process, limiting the impact results can be achieved (apart from the fences designing with curve-linear geometry [5]) by introducing elements with the spring-damping properties into the divider driving systems (and also in the fence) which task is taking over and dissipation of the impact energy.

For the purpose of a competent choice of the construction features that ensure minimizing the dynamic interactions exerted on the sorting loads, and meeting the reliability condition of the sorting process, it is essential to work out a sorting process model in which one of the most important elements is a description of the impact phenomenon between the load and the fence.

Based on the research and analysis reported in the applicable literature, approaches to solving the impact body problem in relation to inelastic impact between the load and the flexible fence, the method that treats the process as a continuous one seems to be most effective. Traditional impact theory [8] treating the impact phenomenon as a discrete (timeless) process is totally useless in the application analysed. Assuming the impact body phenomenon as a continuous process makes it possible to follow the changes of

[1]Corresponding author. *Tel.:* +48-52-340-8145, *fax:* +48-52-340-8038
E-mail address: topiat@atr.bydgoszcz.pl (T. Piątkowski)

interactions between impacting bodies in the time function, i.e. describing the impact force course and its influence on deformations and the positions of the bodies.

During analytic research of the inelastic impact of the load against the fence, the non-linear spring-inelastic properties of the load are considered. Dynamic interactions which appear during the impact between the load and the fence are represented with a modified Kelvin model and spring-damping properties of the fence – with a traditional linear Kelvin model.

2. PROBLEM PRESENTATION

Commonly known design solutions of the dividers in driving systems are characterised by big stiffness – they do not have any elements that would be responsible for taking over and dissipation of the energy generated during the impact between the loads and the fence [5]. With such an approach driving system of the divider is modelled as a system that consists of non-deformable elements and the fence motion is realised according to an exactly described trajectory (in the case of the rocker of the four-bar mechanism resulting from the position of the crank in relation to the links) which is not sensitive to the dynamic interactions which appear while sorting the loads. So far in the formal description in the field of the manipulation process of the loads, the fence together with the driving system of the divider has been treated as a body with infinite mass value (and mass of inertia) whose motion parameters after striking against the load have not been changed (for example: [1], [2], [4], [5]). Introduction of elements softening the impact results into the dividers, 'frees' the fence and makes it possible for it to perform (during sorting of the loads) a motion around the balance position that is partially independent of the driving system constraints (Fig. 1).

In order to have an influence on the manipulator design, and to be able to predict the manipulated loads behaviours as a response to the exploitation parameters, it is necessary to work out a theoretical model of the sorting process. One of the most essential elements of this model is a description of the impact phenomenon.

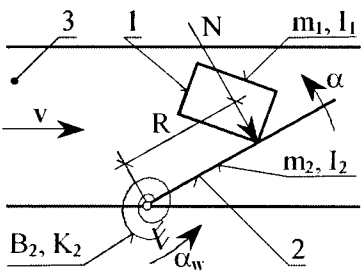

Fig. 1. Scheme of divider with the rotary fence (m_2, I_2) and with the spring-damping element (B_2, K_2); 1 – load, 2 – fence, 3 – conveyor belt, α_w – kinetic constraint

3. MODELS OF THE BODIES IMPACT PROCESS

Parameters of the load motion after the collision with the fence which has the infinite mass or with the fence being a free body (not connected with the divider's driving system) can be assigned based on a traditional impact theory for the rough bodies. This theory uses the stiff body model, and treats the impact phenomenon as instantaneous

(timeless, [3], [5], [8]) process. In this way it is not possible to estimate the quantity, the force or the time duration of the strike. However, in order to compare the load dynamic interactions in the sorting process (in instance applying the fence with the above mentioned motion freedom degree) with the permissible overloads specified by standards which usually refer to the dynamic overloads obtained during the free fall of the load from permissible height on the non-deformable plate, it is sufficient to know the impulse force created – determined in a traditional impact theory:

$$S_y = \frac{m_1 I_2 w_y(0)(1+e)}{m_1 R^2 + I_2} \tag{1}$$

where: R - distance between the point of impact and the axis of the fence rotation,
e – coefficient of restitution,
I_2 – moment of inertia.

The problem appears when we want to carry out research into the impact process eliminating the stiff divider design and using divider that is designed to dissipate impact energy. The fence has then finite mass and it is not a free body – it is connected with the driving system of the divider by means of spring-damping elements. A traditional impact theory (as a discrete process) is totally useless. The problem may be solved if we treat the impact phenomenon as a continuous process. This interpretation takes into consideration the change of dynamic interactions between impacting bodes vs. time and can describe the impact force duration, the deformation and change of the bodies position.

However, not each model that treats impact phenomenon as a continuous impact process can meet the requirements of the application considered. For example, the linear Kelvin model [7], the most common in literature, is unreliable. It comes from the fact that in the case of inelastic impact between bodies (i.e. with the coefficient of restitution $e<1$, which characterises loads in the sorting process analysed), the impact force duration described by the equation:

$$N = b_1 \dot{x} + k_1 x \tag{2}$$

where: x and $\dot{x}$ – deformation and velocity deformation of the loads,
b_1 and k_1 – coefficient of damping and stiffness,

is not consistent with the physical nature of the impact process [3]. The impact force at the impact initiation time ($t = 0$) reaches nonzero value (0a) and maximum value of this force is not sensitive to the fence construction change, 0b. Therefore based on the linear Kelvin's model, it cannot be estimated how the spring-damping properties (or even unconstrained fence, 0b(3)) introduced into the driving system limit the dynamic interactions. Independently of the fence property (with parameters B_2 and K_2), the maximum value of the impact force is the same as when the fence has infinite mass - 0b(1). Only the impact force course changes immediately after the impact initiation ($t > 0$) but the achieved result is not readable enough to describe the advantages of the modifications introduced into the driver design. Kelvin's model limits the impact process analysis when the bodies deformation does not increase the contact area between the bodies.

Considering the connections between the deformation of the impacting bodies and their area of contact, in equations describing impact force there appears non-linearity. This property includes Hertz's theory but its application is limited only to the elastic deformations. The model of the impact process of the load against the fence should

consider a big degree of inelastic property of the manipulated loads, for example the postal packages during the free fall tests on the non-deformable ground give the restitution coefficient equal about e = 0.2.

The proper model for our analysis of the impact process of the load against the fence is the non-linear model, for example, a modified Kelvin's model [9] with the form similar to the Hertz's model whose normal impact force which appears between bodies is described by the following equation:

$$N = q(m_1 k_1)^{0.5} x_1^{0.25} \dot{x}_1 + k_1 x_1^{1.5} \tag{3}$$

where: m_1 – load mass,
q – damping coefficient that is related to the coefficient of restitution.

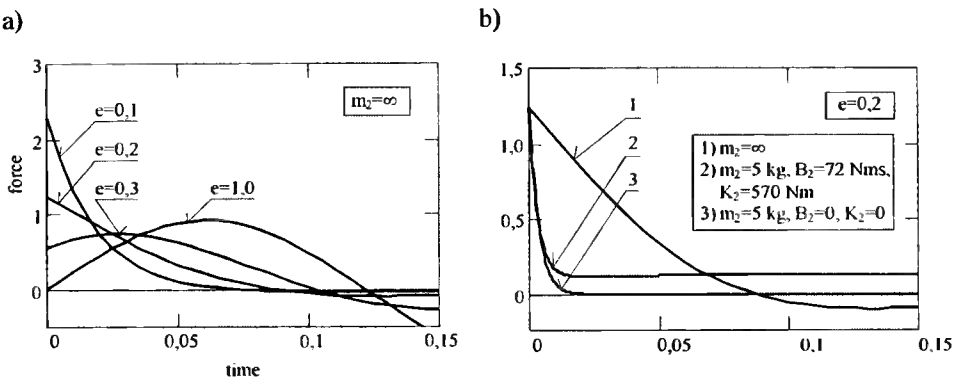

Fig. 2. Plot of the impact forces between the load and the fence, impact process is modelled as a linear Kelvin model – notations according to Fig. 1: a) fence with infinite mass $m_2 = \infty$ and the loads with different coefficient of restitution, b) fence with the infinite mass (1), fence as a body coupled with the driving system through spring-damping element (parameters B_2 and K_2 – (2)) and the fence as unconstrained body (3); coefficient of restitution of the body e = 0.2

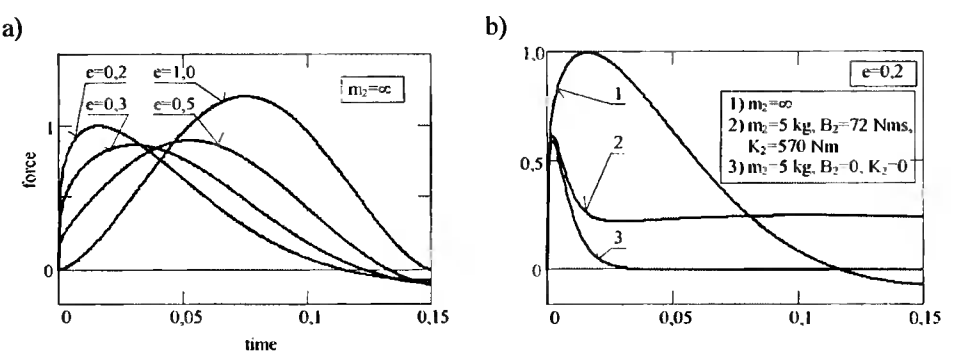

Fig. 3. Charts of the impact forces between the load and the fence, impact process is modelled as a modified Kelvin model: a) fence with the infinite mass $m_2 = \infty$ and the loads with different coefficient of restitution, b) fence with infinite mass (1), fence as a body linkaged with the driving system through spring-damping element (parameters B_2 and K_2 – (2)) and fence as unconstrained body (3)

The elasticity force in this model is proportional to the bodies deformation, whereas the damping force is proportional to the deformation as well as to the velocity deformation. Such a presentation of the dissipation phenomenon of the impact energy makes it possible for the damping force to increase from zero at the time of impact initiation (t=0), regardless of the damping property of the body (Fig. 3a). This impact model has been conceptualised as a system of concentric parings of springs and dashpots in parallel, as shown in Fig. 4. This model includes real dependences between elastic end inelastic deformations – it imitates the local impact model more exactly than the traditional linear Kelvin's model. During impact duration in the phase of compression when the impact force between the bodies increases, the bodies deformation together with the contact area increase too and the region of inelastic deformation becomes bigger and bigger.

Using the modified Kelvin's model, it is possible to estimate the influence change of the spring-damping fence properties on the maximum impact force against the load (Fig. 3b).

Stiffness k_1 and damping coefficient q that appear in equation (3) are estimated during simulation of the impact process through the interactive selection of value k_1 and q. A choice of the parameters value is continued till the coefficient of restitution obtained and the load deformation are comparable with the results of experimental impact body tests.

4. ESTIMATION OF THE INFLUENCE OF THE SPRING-DAMPING PROPERTIES ON THE MAXIMUM IMPACT FORCE

The biggest dynamic interaction, that appears during impact of the load against the fence (on undeformable ground) appears when the mass centre of the load C_s lies on the perpendicular of the impact (Fig. 4), then the force that appears during the impact assumes the same value as during mass point impact against an obstacle. It is so due to the lack of possibility of taking over the impact energy by a potential rotary motion of the load.

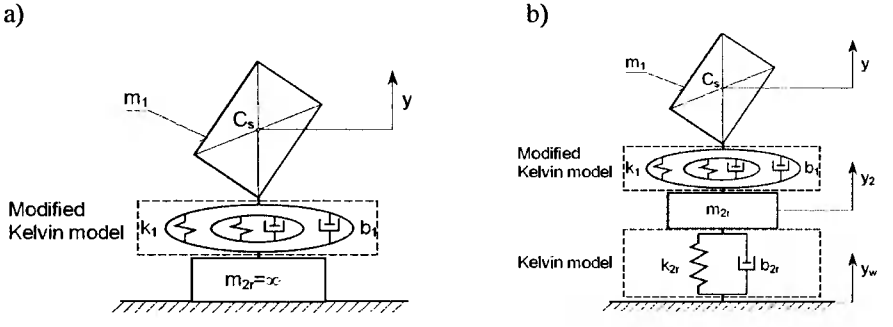

Fig. 4. Model of the spring-damping properties of the load and the sorting device in representation of the translatory motion: a) scheme of the impact between the load and the fence where the fence together with the driving system composes the infinite mass, b) scheme of the impacting bodies where the fence has finite mass and it is transformed to the translatory motion; m_{2r}, k_{2r}, b_{2r} – equivalent mass, coefficient of stiffness and damping

It is convenient to present the impact process configuration between the load and active rotary fence in the translatory motion (Fig. 4).

Using these arrangements, Fig. 5b shows the quotient of the maximum force value that appears during the impact between the load (treated as a mass point) and the fence if the fence has an infinite mass, and if its moment of inertia is a mass function ($I_2=m_2l^2/3$, l=1.2 m – fence length) and when the fence can be an unconstrained body ($B_2=0$, $K_2=0$) during the impact process. The fence moment of inertia has a big influence on the dynamic overloads achieved by manipulated loads. Designing the fence, it is important to give it possibly the smallest mass.

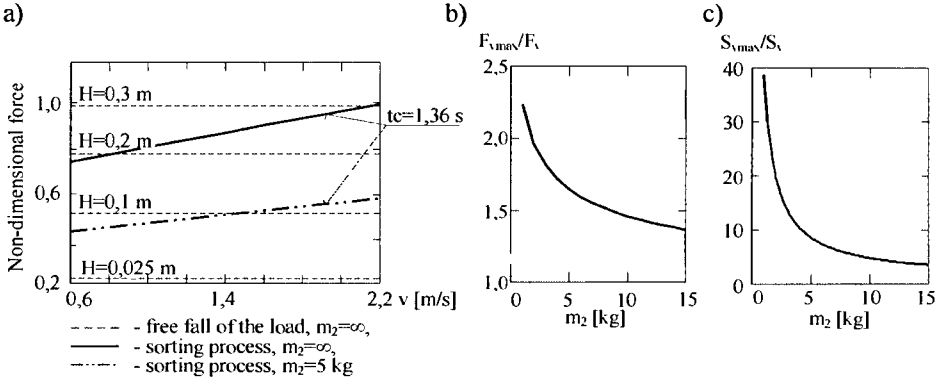

Fig. 5. Dynamic interactions exerted on the load: a) non-dimensional impact force, b) quotient of the maximum forces F_{ymax} ($I_2=\infty$) and F_y ($I_2=f(m_2)$), c) quotient of the maximum impulse force S_{ymax} ($I_2=\infty$) and S_y ($I_2=f(m_2)$)

For example, the fence mass $m_2=5$ kg can cause an about 1.7-time reduction of the dynamic interactions of the load (if an extreme case of the sorting load conditions is assumed, i.e. $m_1=15$ kg, R = 1,2 m, $t_c=1.36$ s, v = 2 m/s). It means that it is possible to decrease the dynamic overload level (for the sorting parameters range examined: working time cycle t_c, velocity of the conveyor belt v) to the dynamic overload obtained during a free fall from the height of H = 0.1 m. These results refer to the 'idealised' case of the impact against the unconstrained (free) fence. The fence linkage with the driving system through spring-damping element takes away motion freedom from the fence causing an increase in the dynamic interactions that are dependent on the restraint degree of the fence motion by damping coefficient B_2 and stiffness K_2.

In the case of the similar analysis, when we use a discrete model of the impacting bodies from the comparison of the dynamic interactions achieved during striking, the load against the fence having infinite mass ($I_2=\infty$) with the impact against the unconstrained fence ($I_2=f(m_2)$), the quotient of the impact impulse force (Fig. 5c) is considerably bigger than the one presented previously in Fig. 5b. According to the discrete impact model, the unconstrained fence with finite mass $m_2=5$ kg should reduce a dynamic interaction exerted on the load above 8 times, whereas according to the continuous impact model presented earlier – about 1.7 times. The rightness of the analytic research results obtained can be estimated only during experimental research of the loads sorting process.

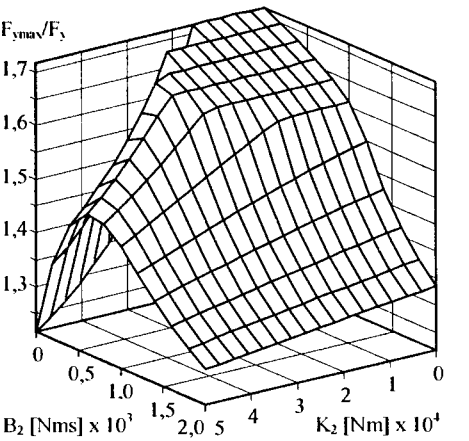

Fig. 6. Influence of the spring-damping property (B_2 and K_2) on the maximum impact force

Fig. 6 shows a chart according to which the parameters influence B_2, K_2 (that limit the motion fence freedom) limiting the dynamic interactions exerted on the manipulated loads can be estimated. The chart is worked out by means of the modified Kelvin's model, according to a discrete impact model such analysis cannot be carried out. On the basis of the initial research, the proposed optimal parameters of the spring-damping element are: $B_2 = 72$ Nms and $K_2 = 570$ Nm. In comparison with the strike against the unconstrained fence these parameters (in Fig. 3b the parameters are referred to in curve (2)) only slight increase the maximum dynamic interaction that appears during impacting bodies.

Using the modified Kelvin's model during analysis of the impact process, we can estimate the spring-damping properties of the fence affecting the maximum impact force, and if the design changes introduced into divider can limit the dynamic interactions of the manipulated loads.

5. CONCLUSIONS

- On the basis of carried out literature survey it can be seen that in the description of inelastic impact phenomenon of the bodies appear two fundamental model groups:
  - o discreet (timeless),
  - o continuous.
- Application of a given model results from the method of the tested mechanical system identification:
  - o impact phenomenon treated as a discreet process is suitable for impact analysis of undeformable and unconstrained bodies or analysis of these bodies colliding with motionless and undeformable obstacle; during calculation the basic algebraic operations are performed,
  - o impact phenomenon treated as a continuous process is suitable for impact analysis of deformable bodies that could be constrained or unconstrained bodies; during calculation solving differential equations of motion are needed.

- In the model group treating the impact phenomenon as a continuous process the most complete information about dynamic force course is provided by models whose description of impact energy dissipation is a function of body strain and strain velocity in the contact point.
- Modified nonlinear Kelvin model presented in the paper shows all the above mentioned properties. The model effectiveness was verified during simulation of the unit load impact against the flexible working element of the sorting manipulator. By means of the model the flexibility of the machine working element can be consciously formed. The aim of flexibility forming is achievement of minimal dynamic reactions.

REFERENCES

[1] Akella S., Huang W.H., Lynch K.M., Mason M.T., 2000. Parts feeding on a conveyor with a one joint robot. Algorithmica 26, 313-344.
[2] Berretty R.P., Overmars M.H., Stappen A.F., 2002. Orienting polyhedral parts by pushing. Computational Geometry 21, 21-38.
[3] Gilardi G., Sharf I., 2002. Literature survey of contact dynamics modelling. Mechanism and Machine Theory 37, 1213-1239.
[4] Mason M.T., 1986. Mechanics and planning of manipulator pushing operations. The International Journal of Robotics Research 5, 53-71.
[5] Piątkowski T., Sempruch J., 2002. Bezier's curve in modelling of scraper's arm geometry. [In:] Polyoptimisation and computer aided design, W. Tarnowski, T. Kiczkowiak (eds), WNT Warszawa, 183-190,
[6] Piątkowski T., Sempruch J., 2002. Sorting process of load units – dynamic model of scraping process. The Archive of Mechanical Engineering 49, 23-46.
[7] Rajalingham C., Rakheja S., 2000. Analysis of impact force variation during collision of two bodies using a single-degree-of-freedom system model. Journal of Sound and Vibration 229(4), 823-835.
[8] Stronge W.J., 1991. Unravelling paradoxical theories for rigid body collisions. ASME Journal of Applied Mechanics 58, 1049-1055.
[9] Zhang D., Whiten W.J., 1996. The calculation of contact forces between particles using spring and damping models. Powder Technology 5, 59-64.

Review by prof. Wojciech Tarnowski

University Press
University
of Technology
and Agriculture
in Bydgoszcz

DEVELOPMENTS IN MACHINERY DESIGN AND CONTROL
Vol. 4 (2005) 83 – 94
Scientific Journal

Tomasz Piątkowski[a)1], **Janusz Sempruch**[b)]

University of Technology and Agriculture
[a)]*Department of Postal Technology,* [b)]*Department of Control and Machinery Design*
ul. Prof. S. Kaliskiego 7, 85–791 Bydgoszcz, Poland

DYNAMIC INTERACTIONS OF IMPACT PROCESS BETWEEN THE OBJECT AND SPRING-DAMPING ACTIVE FENCE

Abstract: In the paper the simulation research results of the impact process between the object (rectangular box-shaped package) transported on the conveyor belt and the spring-damping active rotary fence are presented. A theoretical model has been worked out in which spring-damping properties of the object are described by means of the modified Kelvin's model and the fence arm is treated as the Timoshenko beam. One beam end is fixed to the rotation axis and it is set into a rotary motion by means of a kinetic constrained motion of the fence driving system. The impact process analysis is considered as a plane motion in the plane of the conveyor belt. The fence and the object motion equations were derived based on the Finite Element Method (FEM).

Keywords: unit loads, sorting process, bodies impact

1. INTRODUCTION

One of the methods limiting the dynamic interactions exerted on the objects during handling is to design manipulators whose executive elements with properly matched spring-damping properties. Actuators getting the object into contact should take over and dissipate the energy released during the impact process, minimize the overloads created and simultaneously meet the conditions of reliability, assumed capacity and precision of the executed activities.

The present paper deals with the problem of limiting the dynamic interactions which occur during objects sorting (transported in streams on the conveyors) by means of a nonadhesive manipulator equipped with an active rotary fence [8]. A stiff actuator and the articulated mechanism (main driving system of the manipulator) were linked by a linear spring-damping element (Kelvin-Voigt element). In the paper [7] the possibility of using the pneumatic driving system for the manipulator drive was considered, i.e. driving system, showing a natural compliance resulting from compressed air properties. The examples does not include all the possible concepts that may prevent the objects handled from damage. In the present work an effort was made to use the compliance active fence with properly matched structural stiffness and internal damping in the unit loads sorting process.

[1]Corresponding author. *Tel.:* +48-52-340-8145, *fax:* +48-52-340-8038
E-mail address: topiat@atr.bydgoszcz.pl (T. Piątkowski)

2. PROBLEM PRESENTATION

The structural fence stiffness and the internal damping of the manipulator fence may be depicted as an spring-damping beam with one end fixed to the rotation axis and set into the rotary motion (above the conveyor surface) by means of the kinetic constrained motion. The main problem in the sorting process modelling is the fence dynamic property description and its interactions with the object.

The solution of the system presented, first of all, depends on the proportion between the beam mass and the handled object mass [9]:

- if the beam mass is much smaller than the object mass, then the beam mass may be omitted and the beam treated as a weightless deformable body having one degree of freedom. In the system the beam is regarded as a deformable spring element whose effect on the body is reduced to the spring reaction force.
- if the regarded beam does not get into interactions with the object or if this object has small mass in relation to the beam mass then the beam presents mechanical system with an unlimited number of freedom degrees.
- in certain cases, if the beam mass is small but its influence on the object motion may be considerable, the beam may be reduced to the system with one degree of freedom and its reduced mass attached to the object mass.
- if the beam mass and the mass of the object cooperating with it are of the same order, the system should treat the beam as a continuous body and the object as a body with concentrated mass.

Taking into consideration the proportion between the beam mass and the handled object mass (supposing here the orders are the same) means that during the beam dynamic property modelling the beam should be treated as a continuous body.

The equation of motion the continuous beam has a form of a partial differential equation.

An analytic solution of such an equation exists only for special cases of the load and the beam mounts, i.e. freely supported beam and loaded by transverse force concentrated with constant value moving along the beam with constant velocity [6]. Despite a big practical significance (modelling vehicle motion on the railway tracks and bridges), the solution cannot be adopted for our needs. First of all, it results from characteristics of the force loading the beam (arising between the object and the fence) and its changeable velocity motion along the fence.

To determine the interaction between the spring-damping fence and the object manipulated on the conveyor, an approximate method is needed. Such methods involve a digitalisation of continuous systems and converting the mathematical model from the partial differential equations to ordinary equations solved numerically.

Out of the approximate methods available (i.e. Finite Element Method, Finite Difference Method, Boundary Element Method and their combination) the Stiff Finite Element Method (SFEM) was selected as it can be easily implemented in the Matlab programming environment.

3. THE SFEM METHOD DESCRIPTION BASIS

The Stiff Finite Element Method (SFEM) represents the group of the Finite Element Methods (FEM). Apart from the deformable finite element method (DFEM), it is the core of the FEM methods. The SFEM method was created to analyze the ship structure vibration (torsional, longitudinal and bending vibrations of the drive shafts, device

vibration on the spring washers, bending vibrations of the hull ships). Due to its simplicity the method was found the be applicable in the beam system vibrations analysis and, particularly, in the systems with solids that may be treated as undeformable. The SFEM may be linked with the DFEM [1].

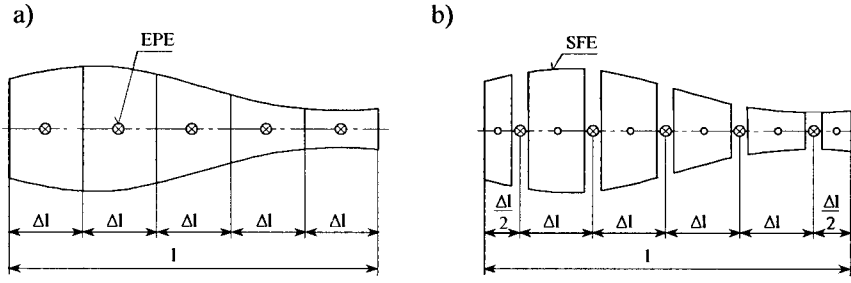

Fig. 1. Continuous beam division [1]: a) stage I, b) stage II

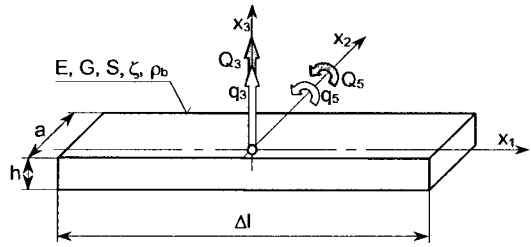

Fig. 2. Stiff finite element (SFE). in the fence arm: q_3, q_5 – generalised coordinates (two degrees of freedom: translation and rotation), Q_3, Q_5 – generalised forces, E – Young's modulus, G – Kirchhoff's modulus, S – cross-section area, ζ – internal damping, ρ_b – density

The beam modelling (by means of the SFEM) takes place at two stages [1]. At the first stage (Fig. 1a) the beam is divided into sections with the Δl lengths. It is assumed that each of these sections is prismatic and in the centre of each of them spring-damping properties are concentrated, creating a weightless spring-damping element (EPE). At the second stage (Fig. 1b) between points where EPE are placed, it is assumed that the beam sections create solids with mass $m_{(i)}$ and moment of inertia $I_{(i,1)}$, $I_{(i,2)}$, $I_{(i,3)}$. These solids are stiff finite elements (SFE). Mathematic formulas describing EPE (stiffness and damping coefficients) can be received on the basis of elementary strength of materials comparing the individual beam section deformations with the EPE deformations. Assuming that the beam (after adaptation into a fence arm) is subjected to the shear and bending stress, the formulas assume the following form [2]:

- shear load in the direction of axis x_3 (Fig. 2):

$$k_3 = \left(\frac{\kappa \Delta l}{GS} + \frac{\Delta l^3}{12 E I_3} \right)^{-1}, \quad b_3 = \frac{\zeta A}{\kappa \Delta l} \tag{1}$$

- bending load in relation to axis x_2 (Fig. 2):

$$k_5 = \frac{E I_2}{\Delta l}, \quad b_5 = \frac{\zeta I_2}{\Delta l} \tag{2}$$

where:

I_2, I_3 – geometrical moment of inertia of the beam cross-section (in relation to the axis x_2, x_3 – Fig. 2),

ζ – internal damping coefficient,

κ – shape coefficient of the beam cross-section regarding the irregular distribution of the tangent stress ($\kappa = 1.2$ – rectangular cross section).

Such a discreet beam model corresponds to Timoshenko's continuous beam model.

4. MODEL OF OBLIQUE IMPACT BETWEEN THE OBJECT AND THE FENCE

In the impact process the analytic equations describing the object and fence motion are derived on the basis of the forces and moments balance principle (d'Alembert principle). The physical model (Fig. 3, Fig. 4) has three reference systems: rectangular (motionless) Ox_oy_o connected with the manipulator frame, rectangular (local) $Ox_{3(i)}x_{1(i)}$ connected with the given SFE and the polar one with the radius-vector r and the polar angle α_p. It is also assumed that:

- the positive motion direction is an anticlockwise direction,
- the impact process is regarded as the plane motion in the belt conveyor plane,
- the object spring-damping properties are modelled by means of the modified nonlinear Kelvin model [3],
- the load is (in the belt conveyor plane projection) rectangular in shape,
- the fence is treated as cantilever Timoshenko beam with the fixed end that is set into the rotary motion with the help of kinetic constrained motion; the beam is modelled following the Stiff Finite Element Method (SFEM); each discreet fence element has two degrees of freedom (Fig. 2),

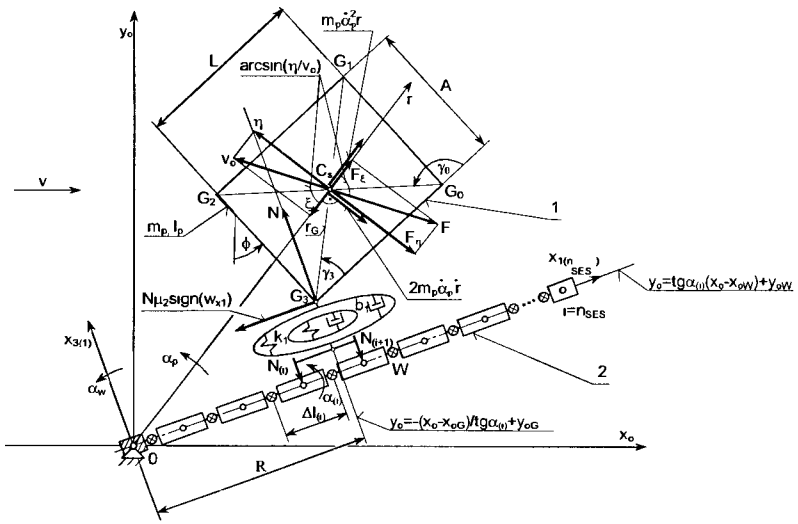

Fig. 3. Scheme of the forces acting on the cuboidal object: 1 – object, 2 – fence

- the friction forces are modelled according to Coulomb law; in the plane motion the resultant friction force and friction moment are determined according to [4],

- the object density distribution is homogeneous; the object, the fence and conveyor belt friction properties are also homogeneous.

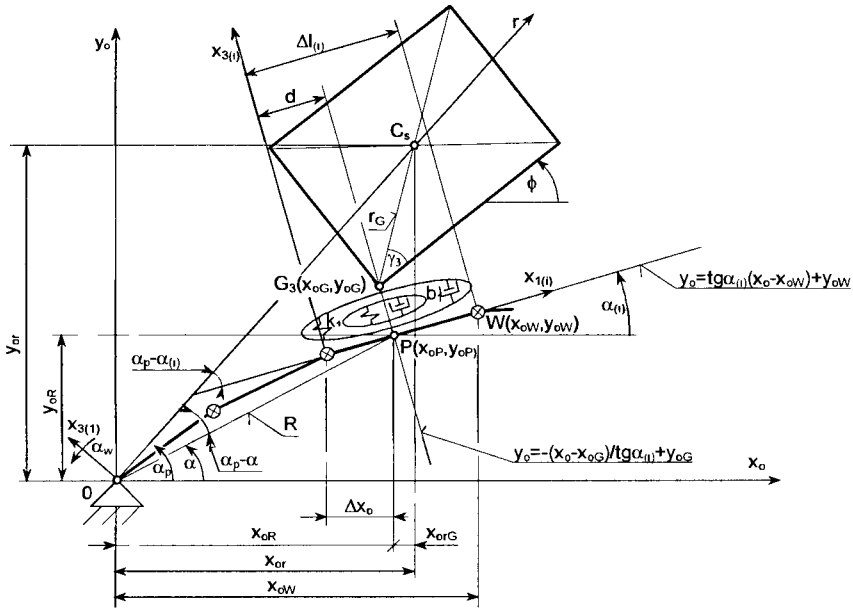

Fig. 4. Geometric relationships between the object and the Stiff Fence Elements (SFE)

Inelastic impact model between the load and the fence treated as a continuous process enables us to estimate the force occurring between the impacting constrained bodies, and makes it possible to describe the object and the fence motion from the impact beginning until a disappearance of forces between them. This model allows for a simulation of the object rotation around the corner sliding against the fence and placing the object along the fence.

Taking into consideration the above established assumptions, the object and the fence motion may be described with equations (according to Fig. 3):

$$\begin{cases} M\ddot{q} + B\dot{q} + Kq = Q \\ m_p\ddot{r} = F_\xi - N\left(\mu_2 \text{sign}(w_{xj})\cos(\alpha_p - \alpha_i) - \sin(\alpha_p - \alpha_i)\right) + m_p\dot{\alpha}_p^2 r \\ m_p r\ddot{\alpha}_p = N\left(\mu_2 \text{sign}(w_{xj})\sin(\alpha_p - \alpha_i) + \cos(\alpha_p - \alpha_i)\right) - F_\eta - 2m_p\dot{\alpha}_p\dot{r} \\ I_p\ddot{\varphi} = -r_G N\left[\cos(\gamma_j - \alpha_i + \varphi) + \mu_2 \text{sign}(w_{xj})\sin(\gamma_j - \alpha_i + \varphi)\right] - M\,\text{sign}(\dot{\varphi}) \end{cases} \quad (3)$$

where:

$j = 0,1,2,3$ – number of the object corners having contact with the fence,
M, B, K – inertia, damping and stiffness matrixes of the discreet fence model,
q – generalised dislocation vector of the size n,
Q – generalised forces vector, constraining fence motion, of the size n,
$n = 2n_{SES}$ – degree of freedom of the discreet fence model,
n_{SES} – amount of the stiff fence elements (SFE).

Taking into account the fence boundary conditions, the first equation in the system (3) should be ordered: according to unconstrained generalised co-ordinates (u – co-ordinates) and according to constrained generalised co-ordinates (w – co-ordinates,

where n = u+w). After the boundary conditions consideration, the equation of fence motion the form:

$$\begin{bmatrix} M_{11}^{uxu} & M_{12}^{uxw} \\ M_{21}^{wxu} & M_{22}^{wxw} \end{bmatrix} \times \begin{bmatrix} \ddot{q}_1^{ux1} \\ \ddot{q}_2^{wx1} \end{bmatrix} + \begin{bmatrix} B_{11}^{uxu} & B_{12}^{uxw} \\ B_{21}^{wxu} & B_{22}^{wxw} \end{bmatrix} \times \begin{bmatrix} \dot{q}_1^{ux1} \\ \dot{q}_2^{wx1} \end{bmatrix} + \begin{bmatrix} K_{11}^{uxu} & K_{12}^{uxw} \\ K_{21}^{wxu} & K_{22}^{wxw} \end{bmatrix} \times \begin{bmatrix} q_1^{ux1} \\ q_2^{wx1} \end{bmatrix} = \begin{bmatrix} Q_1^{ux1} \\ Q_2^{wx1} \end{bmatrix} \quad (4)$$

In the normal impact direction the interaction of forces between the object and the fence (appearing in the equation system (3)) is a sum of the spring and damping forces of the object:

$$N=b_1(m_1k_1)^{0.5}(D)^{0.25}(\dot{D})+b_1(D)^{1.5} \quad (5)$$

where:

b_1 – dimensionless damping coefficient,

k_1 – stiffness coefficient.

In the contact point G_j the object deformation D appearing in the equation (5) expresses the shortest distance between the fence arm and the object corner (Fig. 4). This distance is determined by the line segment linking two points: G_j and P:

$$D=\sqrt{(x_{oG}-x_{oP})^2+(y_{oG}-y_{oP})^2} \quad (6)$$

The point P is an intersection point between two lines:

- the line parallel to the i-th SFE element and crossing the point $W(x_{ow},y_{ow})$:

$$y_o=tg\alpha_{(i)}(x_o-x_{oW})+y_{oW} \quad (7)$$

- the normal to the i-th element SFE and crossing the point $G_j(x_{oG},y_{oG})$:

$$y_o=-(x_o-x_{oG})/tg\alpha_{(i)}+y_{oG} \quad (8)$$

The object deformation velocity is expressed with the following equation:

$$\dot{D}=\frac{d}{dt}(D) \quad (9)$$

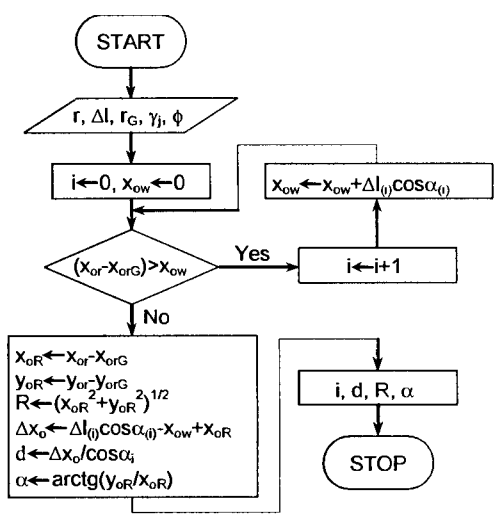

Fig. 5. Diagram describing the object position in relation to the i-th stiff fence element (SFE)

The object position in relation to the fence (i-th SFE determination that is in the contact with the object, vector R, angle α and length d) is determined during the impact process simulation according to Fig. 5. The input data are: r, Δl, r_G, γ_j, ϕ.

Depending on which of the object corners is in contact G_j with the fence, the angle γ_j can be described as:

$$\gamma_j = \begin{cases} \operatorname{arctg}\dfrac{L}{A} & j = 1, 3 \\ \pi - \operatorname{arctg}\dfrac{L}{A} & \text{when otherwise} \end{cases} \tag{10}$$

Radius r_G linking the corner G_j with the object gravity centre C_s is a half of the object diagonal.

The friction component forces F_ξ and F_η between the object and the conveyor belt and the friction moment M in the plane motion appearing in the equation system (3) may be described on the basis of [4]:

$$F_\xi = \frac{\xi F}{v_o\sqrt{1+\left(\dfrac{M_{max}\dot{\varphi}}{F_{max}v_o}\right)^2}}, \quad F_\eta = \frac{\eta F}{v_o\sqrt{1+\left(\dfrac{M_{max}\dot{\varphi}}{F_{max}v_o}\right)^2}}, \quad M = \frac{M_{max}}{\sqrt{1+\left(\dfrac{F_{max}v_o}{M_{max}\dot{\varphi}}\right)^2}} \tag{11}$$

where:

$$F = \begin{cases} m_1 g\mu_{1k} & |v_o| > 0 \\ N \quad m_1 g\mu_{1s} > |N| & |v_o| \le 0 \\ m_1 g\mu_{1s}\operatorname{sign}(N) \quad m_1 g\mu_{1s} \le |N| & \end{cases}$$ – the friction force appearing in the case of the pure translatory object motion,

$$M_{max} = \begin{cases} p\mu_{1k}\operatorname{sign}(\dot{\varphi})\displaystyle\int_{s_p} r_e\, ds & |\dot{\varphi}| > 0 \\ M_{zew} \quad p\mu_{1s}\displaystyle\int_{s_p} r_e\, ds > |M_{zew}| & |\dot{\varphi}| \le 0 \\ p\mu_{1s}\operatorname{sign}(M_{zew})\displaystyle\int_{s_p}\rho\, ds \quad p\mu_{1s}\displaystyle\int_{s_p} r_e\, ds \le |M_{zew}| & \end{cases}$$ – the friction moment appearing in the case of the pure rotary object motion,

g – gravitational acceleration,

μ_{1k}, μ_{1s} – static and kinetic coefficient of friction between the object and the conveyor belt,

μ_2 – kinetic coefficient of friction between the object and the fence,

s_p – area of the contact between the object and the conveyor belt,

p – unit pressure between the object and the conveyor belt,

r_e – vector linking the object rotary axis with the elementary friction area ds,

$\xi = v\cos\alpha_p - \dot{r}$, $\eta = v\sin\alpha_p + r\dot{\alpha}_p$ – components of the slide velocity between the object and the conveyor belt,

moreover:

$w_{xj} = \dot{r}\cos(\alpha_p - \alpha_i) + r_G\dot{\varphi}\sin(\gamma_j - \alpha_i + \varphi)$ – the slide velocity between the object corner and the fence.

In order to maintain the continuous and even load N transferring between the object and the fence, it is assumed that the neighbouring couples of SFE are loaded by properly reduced generalised forces N_i and N_{i+1} according to the below presented proportions:

$$N_i = N\left(1 - \frac{2d_N}{\Delta l_i + \Delta l_{i+1}}\right) \quad N_{i+1} = N\frac{2d_N}{\Delta l_i + \Delta l_{i+1}} \quad i = 2,4\ldots 2n_{SES} \tag{12}$$

This reduction is carried out on the basis of the forces and moments balance principle – Fig. 6.

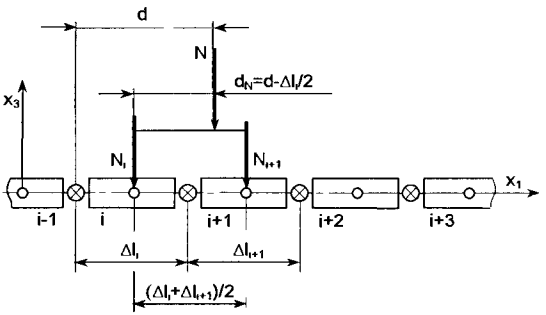

Fig. 6. Force interactions between the object and the fence

5. ELEMENTS OF NUMERIC VERIFICATION

The dynamic processes appearing during the impact between the object and the manipulator fence are given in Fig. 7 and Fig. 8. Numeric research was carried out assuming the homogenous rectangular prism fence made of two hypothetical construction materials: steel (Fig. 7) and polyamide (Fig. 8). In the charts (Fig. 7, Fig. 8) point 1 refers to the impact initiation moment and point 2 – to the impact end.

The impact process was arranged to generate maximal dynamic interactions. Before the impact the object was placed on the conveyor in the position to achieve the contact with the fence end and to locate the object centre of gravity C_s on the impact normal. When the object centre of gravity lies on the impact normal the maximum impact force assumes the same mathematic form like during the impact between the material point and the motionless obstacle. Thus the object kinetic energy loss for rotary motion is avoided.

During the impact phenomenon research the maximum attention was focused on dynamic interactions (Fig. 7f, Fig. 8f) in order to refer them to the permitted overloads (achieved during the object free fall from the permitted height on the undeformable ground – $H_{dop} = 0.3$ m, [10]) and to estimate the effect of manipulator parameters as well as the influence of parameters of the sorting process on the overload level exerted on the objects handled.

The dimensions of the beam cross-section (made of steel and polyamide) are matched so as to achieve the most loading impact conditions during the impact ($v = 2$ m/s, $m_p = 15$ kg, $l = 1.2$ m, maximum constrain angular velocity $\dot{\alpha}_{w\ max} = 1.53$ rad/s – Fig. 7d, Fig. 8d) the fence end deflection up to 0.09 m (Fig. 7c, Fig. 8c).

Regardless of the kind of fence construction material during the impact simulation, the similar object behaviour was achieved:

- the object achieved a comparable maximum slide velocity (in relation to the conveyor belt – Fig. 7i, Fig. 8i) and a comparable dislocation (Fig. 7a, Fig. 8a),
- comparable dynamic overloads were registered (Fig. 7f, Fig. 8f) which were nearly double lower than during the object impact against a stiff fence,
- the object revealed single-time tendency to the loss of contact with the fence (minimum in the impact force course – Fig. 7f, Fig. 8f) but a higher contact loss probability was in the case of the steel fence,
- at the impact initiation moment there was observed immediate 'break' of the static friction between the object and the conveyor belt after which there was realized undisturbed (for example by stick-slip phenomenon) kinetic friction (Fig. 7g,h, Fig. 8g,h).

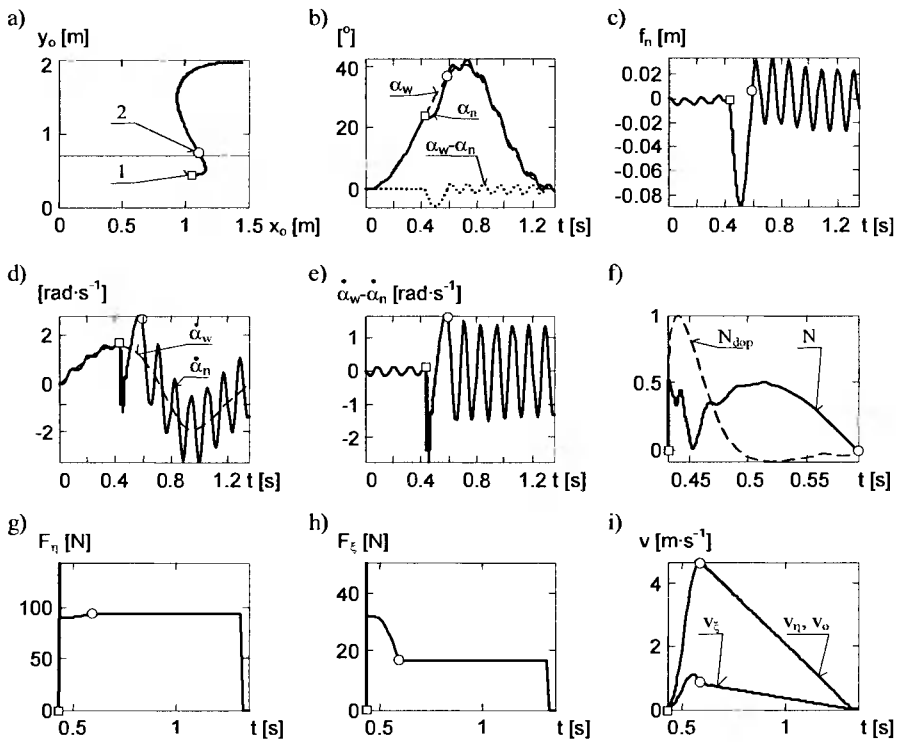

Fig. 7. Impact process simulation results, the fence made of steel (1, 2 – start and end of the impact process): a) motion path of the object centre of gravity, b) motion path of the constrain α_w, the fence end α_n and α_w-α_n, c) deflection on the fence end, d) angular velocity of the constrain $\dot{\alpha}_w$ and the fence end $\dot{\alpha}_n$, e) angular velocity of the fence end according to the balance position, f) impact force duration in relation to the body impact with the undeformable ground with the permitted height (H_{dop} = 0.3 m – [10]), g) and h) friction force components, i) slide velocity between the object and the conveyor belt; process parameters: the beam cross-section a·h = 0.1·0.015 m, $E_s = 2 \cdot 10^5$ MPa, $G_s = 8 \cdot 10^4$ MPa, $\zeta_{ss} = 2 \cdot 10^6$ N·m^{-2}, n = 20, $b_1 = 1.5$, $k_1 = 10^5$ N·m$^{-1,5}$, v = 2 m·s^{-1}, m_p = 15 kg, l = 1.2 m, $\mu_{1k} = 0.65$, $\mu_{1s} = 0.85$, $\mu_2 = 0.35$

In relation to the fences made of different construction materials, the fundamental difference in the object impact process course concerns the occurrence of weakly fading oscillatory vibrations resulting from the low internal damping (in the case of steel fence). This feature worsens the fence work conditions. After the fence working cycle realization and its returning to the starting position the fence end oscillates around the balance position with the deflection amplitude up to 0.02 m (Fig. 7c). These deflections may disturb the next working cycles and the objects flow to the further manipulators placed along the conveyor.

Fig. 9 refers to the estimation of the softening effectiveness of the dynamic effects between the object and the spring-damping fence Z_{spr_pl} and the stiff unconstrained fence Z_{swob} (in the thickness function of the beam cross-section h and the beam mass). On the basis of these charts the fence that is designed with respect to the construction stiffness should give greater benefits for softening the impact results (for the regions marked in the charts, Fig. 9) than in the case of application of the stiff fence linked with the complianed driving system ([7, 8]).

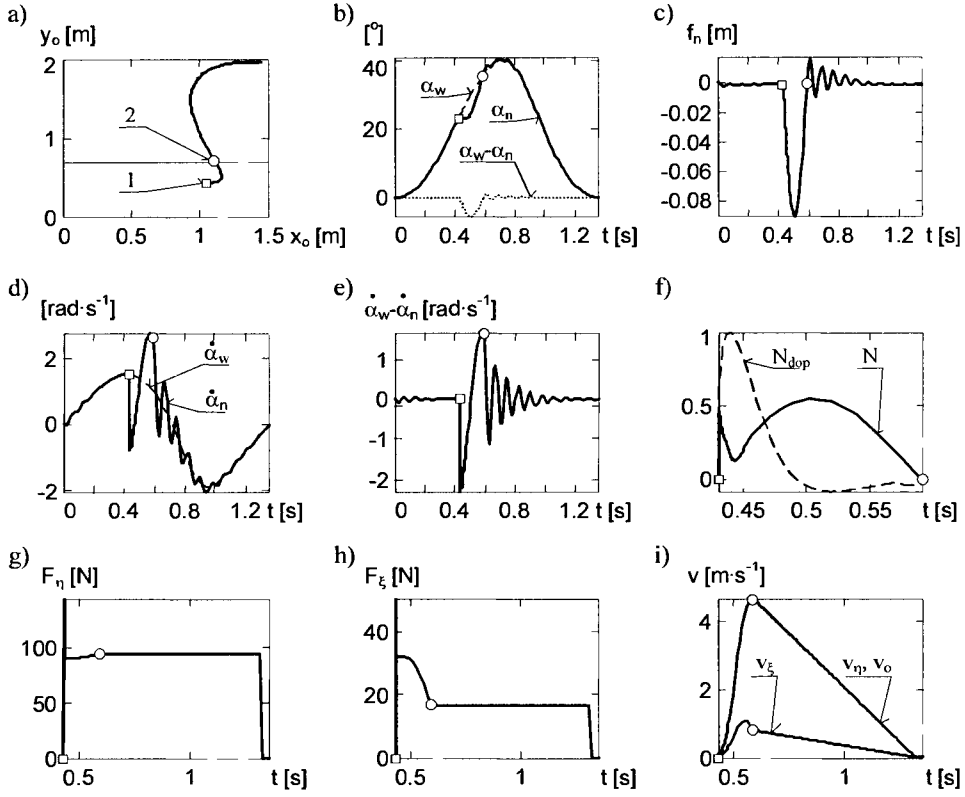

Fig. 8. Impact process simulation results, the fence made of polyamide; the beam cross-section a·h = 0,1·0.04 m, $E_p = 10^4$ MPa, $G_p = 4 \cdot 10^3$ MPa, $\zeta_p = 7 \cdot 10^7$ N·m^{-2}; remaining symbols given in Fig. 7

6. CONCLUSIONS

The paper presents the modelling proposal of the impact process between the object (in the form of the package of the rectangular box shape) transported on the conveyor belt and the spring-damping active rotary fence. The fence dynamic properties are described using the Stiff Finite Element Method (SFEM) and the impact phenomenon – by means of nonlinear modified Kelvin model.

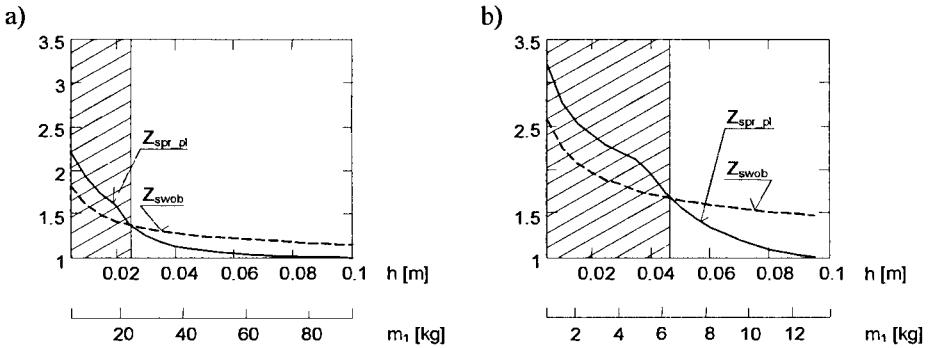

Fig. 9. Softening effectiveness of the dynamic overloads occurring between the object and the spring-damping fence $Z_{spr\text{-}pl}$ and the stiff unconstrained fence Z_{swob}: a) the steel fence, b) the polyamide fence

The inelastic impact model makes it possible to examine the influence of the fence geometric-material features on:

- value of forces occurring between impacting bodies,
- the object and the fence motion path from the impact beginning to the impact force disappearance.

The preliminary research shows that:

- the compliance fence design (which takes into consideration construction stiffness) should bring bigger benefits in softening the impact results than the stiff fence linked with the compliance driving system,
- the compliance fence made of homogenous construction material with the small internal damping performs weakly fading oscillatory vibrations after the working cycle,
- excessive oscillatory fence vibration may be softened by an introduction of damping structure or/and selection of constructional materials with high internal damping to the fence.

REFERENCES

[1] Kleiber M., 1995. Komputerowe metody mechaniki ciał stałych. WNT Warszawa.
[2] Kruszewski J., Wittbrodt E., Walczyk Z., 1993. Drgania układów mechanicznych w ujęciu komputerowym. T. II. Zagadnienia wybrane. WNT Warszawa.
[3] Zhang D., Whiten W. J., 1996. The calculation of contact forces between particles using spring and damping models. Powder Technology 5, 59-64.
[4] Goyal S., Ruina A., Papadopoulos J., 1991. Planar sliding with dry friction. Part 1. Limit surface and moment function. Wear.

[5] Jalili N., Esmailzadeh E., 2002. Dynamic interaction of vehicles moving on uniform bridges. Multi-body Dynamics. IMechE London.
[6] Szcześniak W., Ataman M., Kozyra Z. 2003. Rozwiązanie problemu ruchomej siły na belce Eulera we współrzędnych ruchomych. Transport 1(17), 145-169.
[7] Piątkowski T., 2004. Aktywna zastawa obrotowa z napędem pneumatycznym. Pneumatyka 4(47), 24-27.
[8] Piątkowski T., Sempruch J., 2002. Analiza procesu manipulowania ładunków jednostkowych. Mechanics and Mechanical Engineering, special issue: Problems of Working Machines Development 6, 187-194.
[9] Osiński Z. 1980. Teoria drgań. WNT Warszawa.
[10] PN-O-79100/02, 1992. Opakowania transportowe z zawartością, dane liczbowe.

Review by prof. Franciszek Siemieniako

University Press
University
of Technology
and Agriculture
in Bydgoszcz

DEVELOPMENTS IN MACHINERY DESIGN AND CONTROL
Vol. 4 (2005) 95 – 101
Scientific Journal

Janusz Sempruch[1], Jakub Maciejewski

University of Technology and Agriculture, Department of Control and Machinery Design
ul. Prof. S. Kaliskiego 7, 85–791 Bydgoszcz, Poland

GEOMETRY AND INITIAL VERIFICATION OF A FATIGUE TESTING STAND EXPOSED TO ROTARY BENDING

Abstract: The paper presents a design and verification of the basic assumptions made for a fatigue testing stand exposed to rotary bending. The verification includes the modelling of numeric stand zone in which the sample is fixed. Numerical analyses of stress distribution are made on the measurement part of the sample using FEM software.

Keywords: fatigue, rotary bending, numerical analysis

1. INTRODUCTION

The aim of the present paper is mainly a presentation of the designing process preformed for fatigue testing stand exposed to rotary bending. To perform this process, the following design assumptions were made: stress distribution homogeneity along the sample measurement length, a development of the design, despite author's character, should refer as much as possible to research methods treated as standard in fatigue testing when exposed to bending, a source of load input is pneumatic cylinder. Another essential assumption for the solution presented is a possibility of performing tests under different load conditions (constant and variable amplitudes). The paper also presents the verification of the assumption about the stress distribution homogeneity along the sample measurement length for the fixing and load method used, which will be applied with the stand model developed with FEM software.

2. STAND CONCEPT AND SELECTED SOLUTION

Futher in the paper three concepts of the stand will be presented. This stand will allow for performing fatigue testing exposed to rotary bending. The concepts were developed with the information given in [1], (Fig. 1, Fig. 3, Fig. 5). For the purpose of the sample fixing and load given in [1], kinematic testing stands geometries were developed which constituted a field of possible solutions.

Figure 1 presents the method of fixing and load of single-sided fixed sample. When applying this method, the sample is exposed to bending moment of a linear-variable value. To limit the effect of this variation, there was determined a part of the measurement sample of a lower stiffness for which, according to Fig. 1, the distribution

[1]Corresponding author. *Tel.:* +48-52-340-8223; *fax:* +48-52-340-8245
E-mail address: semjan@atr.bydgoszcz.pl (J. Sempruch)

of bending moment M_b and normal nominal stress S show a slight variation. Figure 2 offers a proposal of a research stand geometry solution showing the idea given in Fig. 1. In Fig. 2. the left holder of the sample has one degree of freedom, that is a possibility of turning against its own axis, which makes it possible to introduce torque on the sample from the drive system given in diagram in Fig. 2. The right holder allows for turning the sample against the non-turning socket. The lever system refers to the assumption about the use of pneumatic cylinder and allows for, at the cost of greater dislocations, limiting the force impacting the sample load system. The right holder can perform dislocations U according to diagram given in Fig. 2.

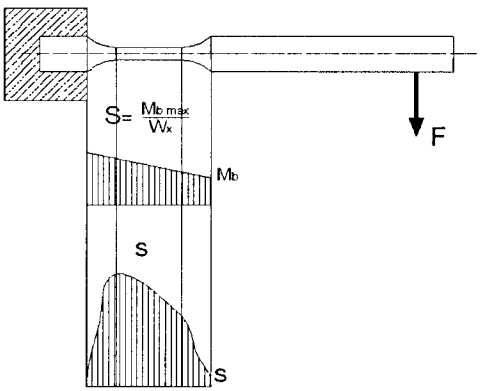

Fig. 1. Stress and bending moment distribution in the sample of the constant cross-section single-side loaded with the force, has been developed based on [1]

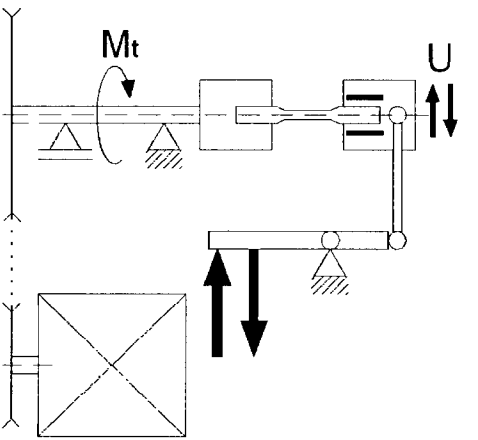

Fig. 2. Kinetic stand diagram – concept I

Figure 3. refers to, after [1], the idea of performing four-point bending. Two sample holders, two of which can turn together with the sample against their axis, were impacted by two couples of forces. Such a method of sample loading makes the bending moment constant along the sample length between the holders, thus ensuring the constants of nominal stresses along the sample measurement length.

According to kinematic and geometry diagram (Fig. 4), each sample holder is a two-support beam which allows for turning against the fixed load impact system. One couple of forces is performed as a coupling rod system connected with the load source (pneumatic cylinder) – active forces. The second couple of forces is obtained in a form of reactive forces on rotary supports A B.

The third stand concept has been developed with the idea given in Fig. 5. It is a logical connection of earlier discussed methods of sample loading. The left side of the sample is fixed in the holder, adequately for the one-sided-fixed sample, while the right side of the sample is impacted with a couple of forces. As a result, partially we obtain advantages characteristic for one-sided-fixed sample – simplicity of the testing stand and four-point load, namely the homogeneity, which is the constancy of distribution of bending moment and nominal stresses which come from it on the measurement part of the sample. Figure 6 presents a geometry concept of the stand, the left sample holder is made the same as in concept I given in Fig. 2, while the right sample holder is much

compliant with concept II, Fig. 4. The dislocation of the impact point of the active force is dependent on the practical reasons only.

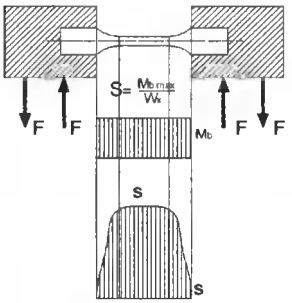

Fig. 3. Stress distribution for four-point sample load of the constant cross-section, has been developed based on [1]

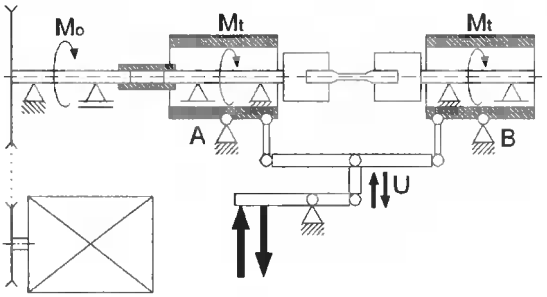

Fig. 4. Kinetic stand diagram – concept II

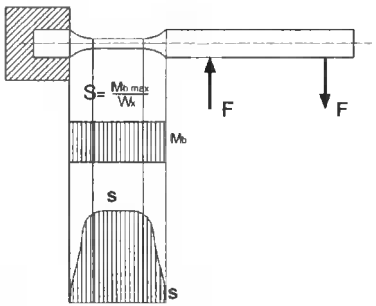

Fig. 5. Stress distribution for bending of sample of the constant cross-section, one-side-loaded with a couple of forces, has been developed based on [1]

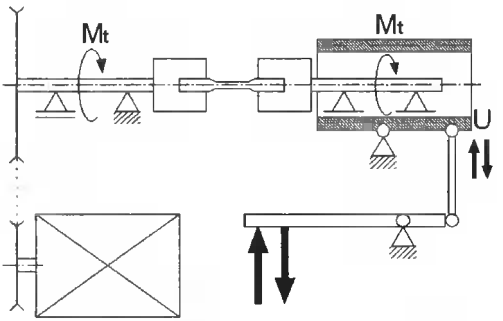

Fig. 6. Kinetic stand diagram – concept III

Selecting the concept, it was most important to ensure homogeneous stress distribution in the measurement part of the sample. Additionally there was considered a number of motion connections. Concepts II and III were found to meet such criteria.

3. MODEL OF SAMPLE LOAD SYSTEM AND VERIFYING STRESS DISTRIBUTION

The idea given in chapter 2, in Fig. 3, and concept II, connected with it, is well known and has been adapted in practice many times in real-life stands for fatigue testing. It showed a homogenous and completely satisfactory stress values distributions along the sample measurement length. Here we will limit our considerations to presenting FEM sample model (Fig. 7a) and the obtained distribution of stress values along the sample measurement part length (Fig. 7b). The finite elements grid and sample loading method were modeled using ANSYS Workbench version 9.

The sample was supported on both sides; on the left side with the fixed support and on the right side – on the mobile support. The supports were placed on the front surfaces of the sample, and the load with the bending moment (static load) was impacted to its cylinder surface in the holding parts.

The sample was modeled as non-regular prisms elements, the grid division parameters were: number of elements 2132 – number of nodes 10178. The analysis was made for elastic strains (adequately for the planed testing stand purpose, which is high cycle fatigue life).

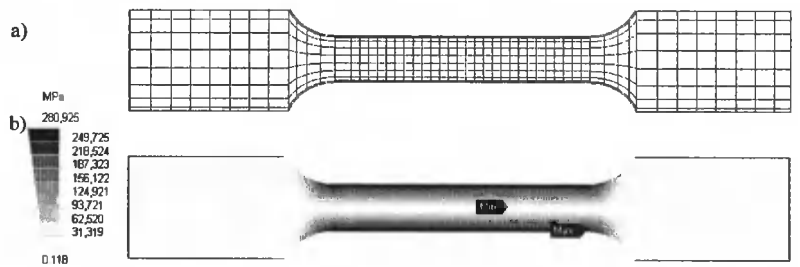

Fig. 7. Division into finite elements and stress distribution in the sample

The stress distribution given in Fig. 7b meets the expectations.

The testing stand concept which gives the idea in Fig. 5, concept III, is much less popular and in literature it is difficult to find properly-made testing stands connected with it. For that reason for the purpose of verifying this idea in the process of modeling, it was necessary to carry out, besides the static analyses, also the analysis for the full cycle of fatigue load which corresponds to a single turn of the sample. For practical reasons with such a range of analyses for stand modeling in FEM environment, MSC Visual Nastran was used. In this environment the measurement and holding sample parts and parts of holders and shafts applying torque and bending moment were modeled.

Then concept III was verified, the 3D model made was transferred to MSC Visual Nastran. The model was limited to the holding part of the sample and simplified shafts sections transferring the drive and input load (Fig. 8).

The verification was made at two stages, first numerical static analysis were made to be compared with expected analytic calculations and in reference to earlier determined stress values for testing stand concept II.

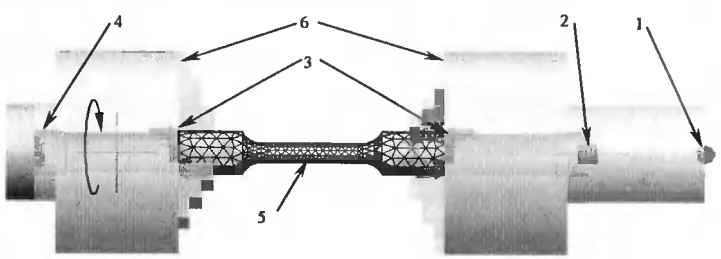

Fig. 8. View of the stand model analyzed: 1 – deflectable support, 2 – traveling support, 3 – stiff support, 4 – torque drive on the fixed support, 5 – sample, 6 – holders

In the model presented the sample was supported in holder (6) to allow for adequate sample and holders fronts transferring the mutual load. Rotary motion was applied to one of the holders (4) carried by the sample (5) to the next holder. On the right side the holder was fixed in traveling support (2) on deflectable arm (center turn 1) to which concentrated force was applied. Below, Fig. 9 presents the method of applying concentrated force. The situational view refers to concept III, Fig. 6.

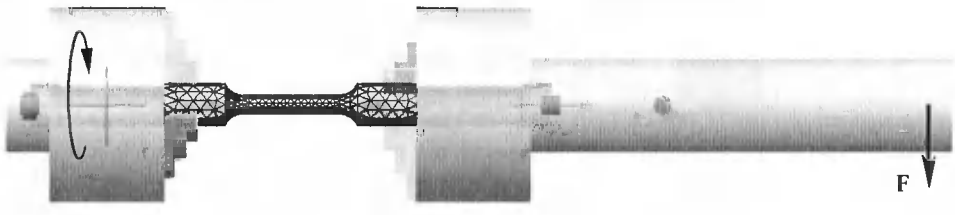

Fig. 9. Situation view of the simulation made

Preliminary static calculations were made without applying torque. The sample calculated was divided into tetragonal laments, grid parameters were: maximum grid angle 25°; number of elements 2097; number of nodes 3768. The analysis was made like in the previous case for elastic strains. Figure 10 indicates the stress distribution of the sample obtained in such a way.

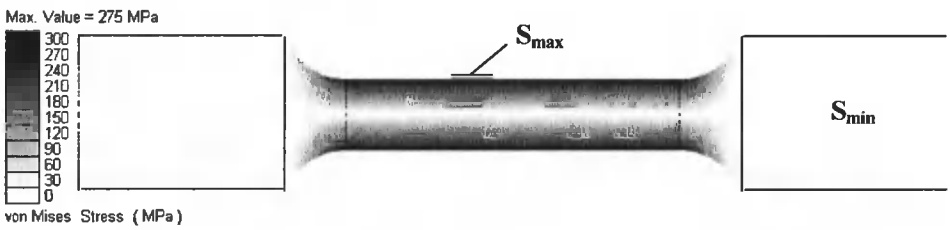

Fig. 10. Stress distribution along the sample length disregarding gravity

The stress distribution meets the expectations (Fig. 5). The values obtained do not differ much from the values calculated analytically and the values determined for numeric model in concept II.

In the further part of the analysis a simulation was made for a one-full cycle of load, namely 1 full sample turn exposed to a constant force. The simulation showed at the constant rotational speed for 1 full turn, the stress values in the sample changed in the range 12 MPa.

4. PRESENTATION OF THE GEOMETRY SOLUTION AND THE ANALYSIS OF LOADS FOR THE TESTING STAND

Figure 11 presents the visualization of the geometry solution developed for the stand to test fatigue when exposed to rotary bending according to concept III. The figure shows: 1 – sample tested, 2a and 2b – respectively left and right sample holder (the holders were made of self-centering three-jaw chuck, left support which only allows the sample for the turn against its axis of symmetry, 4 – test stand drive which is represented in the diagram only with one element of belt transmission, 5 – right support which ensures the sample turn against its axis of geometry and deflectability against axis 6, 7 – pneumatic

cylinder. The right support, according to the kinematic diagram given in Fig 6, allows longitudinal travel of holder 2b against the deflectable support body.

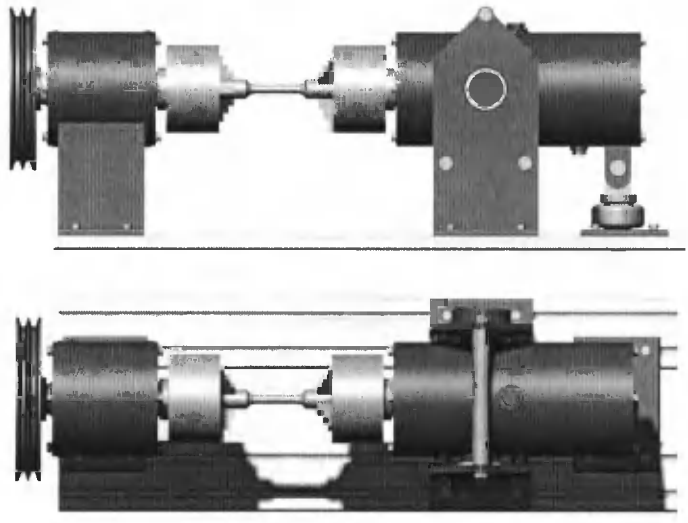

Fig. 11. Testing stand projections

Figure 12 presents feasible values of variable stresses recorded on the external surfaces of the sample. Figure 12a shows the feasible distribution of the stress values when the pneumatic cylinder acts with constant force. Stress value variation, as far as frequency is concerned, depends on the rotational speed in wheel 4 of belt transmission of the stand given in Fig. 11. Changing periodically the value of the force realized by the pneumatic cylinder, we will obtain the variation of stress values reflecting the experiments with the so called programmable load (service load model).

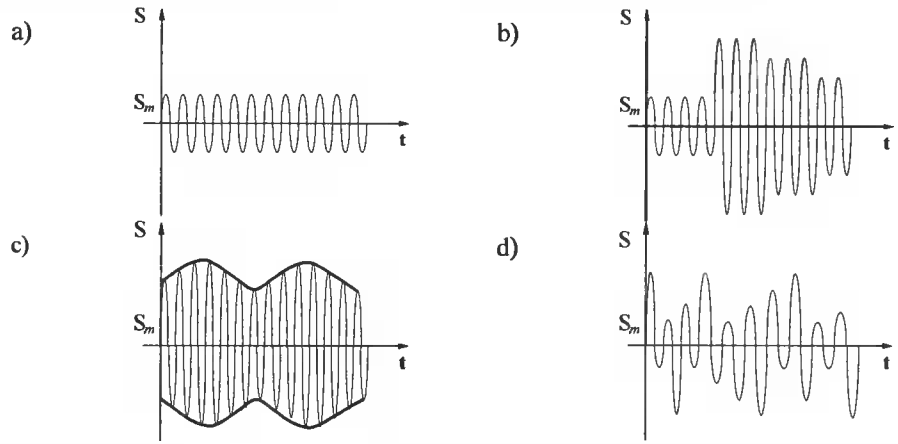

Fig. 12. Stress distribution at: a) constant force, b) discrete variable, c) polyharmonic variable, d) random variable

When the variation in the effect of pneumatic cylinder is harmonic amplitude, we will obtain, as a result, polyharmonic amplitude of stress on the sample surface.

Adjusting the frequency of the changes in the load performed on the pneumatic cylinder to the frequency of stress changes as a result of rotational speed of the sample, we can obtain random variable load of a narrow spectrum.

The expected load methods can be applied for an adequately designed control system which is synchronized with the rotational frequency.

5. CONCLUSIONS

The paper presents a fatigue testing stand exposed to rotary bending developed by the authors. The design follows the standard methodology proposed by [1]. What is unique in the solution offered is the homogeneity of stress distribution along the measurement length of the sample (characteristics for four-pint bending), with a limited number of nodes which occur in the load dislocation system. The application of the pneumatic cylinder makes it possible to decrease the testing stand manufacturing costs substantially. The stand, as given in Fig. 12, allows fatigue testing in a very wide range, which refers to the load model applied.

REFERENCES

[1] PN-76/H-04326 Badanie metali na zmęczenie. Próba zginania.

Review by prof. Tadeusz Łagoda

University Press
University
of Technology
and Agriculture
in Bydgoszcz

DEVELOPMENTS IN MACHINERY DESIGN AND CONTROL
Vol. 4 (2005) 103 – 116
Scientific Journal

Václav Tesař[1]
University of Sheffield, Department of Chemical and Process Engineering
Sheffield, S1 3JD, United Kingdom

NUMERICAL COMPUTATIONS OF AERODYNAMIC PERFORMANCE OF WIND TURBINE ROTOR SECTIONS – USING GENERAL PURPOSE SOFTWARE

Abstract: Paper summarises experience with computing aerodynamic performance of wind turbine rotor airfoils derived from popular NACA 63-418. Effects of shape changes necessitated by manufacturing aspects on the section polar diagram were evaluated by numerical flowfield computations using standard commercially available FLUENT package. The task is not easy for this typical general purpose CFD software, mainly because of the decisive influence of the laminar boundary layer and its transition into turbulence. Especially the section drag is affected by these effects, not so important in typical engineering problems for which FLUENT is optimised. While lift and its dependence on attack angle were computed with excellent accuracy, results for drag are less successful. Fortunately, no absolute precision was asked for in the present computations, which were to provide a comparison between the basic section and the modified alternatives. For this purpose the solutions performed under the same conditions provided reasonably reliable conclusions.

Keywords: wind turbine rotors; CFD solutions, NACA 63-418, polar diagram

1. INTRODUCTION

Wind turbine rotor sections in current use profit from the extensive and painstaking research of aircraft wing sections performed mainly in the first half of the last century. High popularity among the rotor designers is attributed to the families of airfoil shapes developed in 1930-1945 at NACA [1]. While earlier design of airfoils up to 1930 was rather arbitrary, guided only by experience with known shapes and experimentation with modifications, NACA airfoil shapes were generated using analytical specification of geometry. Extensive airfoil families were set up, backed by exceptionally reliable experiments in the world's best wind tunnels – especially for the laminar flow airfoils, low turbulence tunnels were built with large area contraction upstream from the test section, making such tunnels large and expensive.

A dramatic change in the character of Fluid Mechanics in general – and aeronautical aerodynamics in particular – came with the availability of computers and CFD software. Ideally, they should make it now possible to compute the performance without recourse to experiments. However, despite the tremendous progress, general

[1]Corresponding author. *Tel.:* +420-2-6605-3282; *fax:* +420-2-8658-4695
E-mail address: v.tesar@sheffield.ac.uk (V. Tesař)

advice is to consider the computation an excellent tool for interpolation between available experimental data at which the numerical solution is adjusted for agreement. Even extrapolation outside the range of available experimental results should be viewed upon with caution.

Two fundamental problems have led to this unsatisfactory state of the art: computational limits on one hand and fundamental insolvability of turbulence and its origin on the other hand. The computing power limits the number of discretisation elements in the flowfield. About ten years ago, the typical number of discretisation elements into which the computed domain could be divided were of the order of 1 000. This is a number usually too small for resolving details of thin shear layers. This limitation was due to the capacity of the computer memory. Even until about five years ago, with all the phenomenal progress in available computer memory capacity, the largest number of discretisation elements in the flowfield had been rarely above the order of 10 000. The limiting factor then was the computation speed. A larger number of mesh elements was possible but would result in the computations being agonisingly slow. There were supercomputers with large number of parallel processors, available, however, only in specialised institutions for special tasks. A common user has obtained an access to high performance computers, enabling him to chose number of the element larger than 100 000, only very recently.

The other problem area is due to the fact that most practical flows encountered by engineers are turbulent and there are no exact solutions of turbulence [2]. All what can be done is modelling the turbulence. A whole hierarchy of models is available, none of them the 'best' one: different flow configuration call for different complexity of the model. Advanced models are, of course, better – but they generally require simultaneous solution of a large number of transport equations for turbulence parameters, slowing down the solution progress. Only experience – a thick portfolio of computed cases – can lead to a reliable guidance as to which turbulence model is suitable for a particular problem.

Shear flows [2] – such as the flow in the boundary layers on airfoil surfaces – present a particularly difficult task. The steep transverse velocity gradient in the boundary layer at the wall calls for an extremely fine discretisation mesh, often with the number of mesh elements at the very limits posed by the available computation facility. In addition, as the wall is approached, the size of the turbulent eddies of importance for momentum transport decreases. The Reynolds number of turbulence becomes small. In the immediate vicinity of the wall, in the viscous sub-layer, the flow (though not completely devoid of vortical motions) behaves as if it were laminar. The basic models of turbulence are usually set up under an assumption of fully developed turbulence, ceasing to be valid at and near the wall. The software authors were forced to by-pass the problem by introducing approximate dependences, the wall functions. These are usually based upon known turbulent boundary layer solutions on flat plates. The first of the discretisation node, the one nearest to the wall, is placed at a distance large enough for it being outside the sub-layer. Even then the models of turbulence have to be modified to handle the low Reynolds number turbulence [2]. Quite a number of such modifications are known (about ~10 of them are in current use), unfortunately again all being just approximations with uncertain applicability for a particular problem. On the usual, most often curved, airfoil surfaces the application of the flat-plate wall functions with a modified turbulence model may provide a reasonable result as often as not.

2. THE TASK: COMPUTATION OF FLOW PAST AIRFOIL NACA 63-418 AND ITS MODIFICATION

The author was approached by one of the world's leading wind turbine rotor manufacturers and asked to perform at a short notice numerical computations for sections derived from the currently popular [3, 4] turbine rotor section NACA 63-418. The modifications, an example of which is shown in Fig.1, were necessitated by manufacturing aspects. Only very short time was available, making experimental investigations or even acquiring a specialized software out of question. The author possessed at that time no experience with this type of computation tasks (all his previous computations were of the internal flow tasks).

The basic airfoil belongs into the 6-Series section family, developed at the National Advisory Committee for Aeronautics (NACA) in the USA during early 1940's. It was designed by a method specifying prescribed pressure distribution and employing an early airfoil theory [5], [6] to derive the required geometrical shape. The goal was to maximise the region over which the boundary layer remains laminar. Aerodynamic properties of the section family were verified by measurements in NACA Langley Research Center two-dimensional low-turbulence variable density tunnel (TDT), built in 1941 [7]. The extremely low turbulence level in this tunnel test section was between 0.0002 and 0.001 (increasing with flow speed). The second digit, 3, in the airfoil identification (NACA 63-418) indicates [1] the location of the minimum pressure in tenths of chord c (- i.e. minimum at 0.3 c). The design lift coefficient is specified by the first digit after the dash in tenths – in the present case the digit is 4 and the design lift coefficient is $c_L = 0.4$. The final two digits specify the thickness in percentage of chord, in the present case the thickness is 18%.

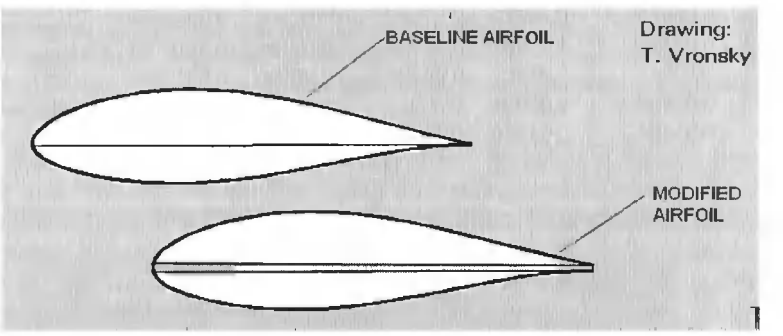

Fig. 1. Modification the consequences of which are discussed in detail in the present paper consists basically of inserting a wedge-shaped filling band between the two airfoil halves

The computations were to be performed as two-dimensional, neglecting the problems of induced drag and end vortices. This simplifies the computations. For the requested comparison purposes, the fact that the resultant drag is just the section drag was quite irrelevant. On the other hand, a rather unpleasant requirement from the computational point of view was the request to cover the complete polar diagram between angles of attack 0 and 20 deg with 2.5 deg steps. It is much easier to cover a given range of Reynolds numbers by changing only the upstream velocity boundary condition for each run. In the present case it was the chord Reynolds number value $Re_c = 3.00E+06$ that remained constant, but it was necessary to set up a new computation domain with

painstakingly constructed discretisation grid for each of the runs. Of course, the huge numbers of the elements in the currently used meshes (of the order of 100 000) made any idea of manual distribution of the discretisation elements around the airfoil surface impractical. The discretisation was generated by pre-processing software GAMBIT version 2.1.2, supplied by FLUENT Inc.

Table I. Geometry data for the basic airfoil

1	0
0.95032	0.00978
0.90069	0.02017
0.85099	0.0313
0.80119	0.0428
0.75128	0.05438
0.70125	0.06564
0.6511	0.07626
0.60083	0.08596
0.55046	0.09446
0.5	0.10148
0.44946	0.10672
0.39886	0.10986
0.34823	0.11058
0.2976	0.10854
0.24699	0.10385
0.19645	0.09632
0.14602	0.0856
0.09577	0.07087
0.07007	0.06139
0.04593	0.04975
0.0214	0.03455
0.00945	0.0241
0.00487	0.01833
0.00267	0.01484
0	0
0	0
0.00733	-0.01284
0.01013	-0.01553
0.01555	-0.01982
0.0286	-0.02711
0.05407	-0.03711
0.07923	-0.04443
0.10423	-0.05019
0.15398	-0.05868
0.20355	-0.06448
0.25301	-0.06805
0.3024	-0.06966
0.35177	-0.06938
0.40114	-0.06702
0.45054	-0.06292
0.5	-0.05736
0.54954	-0.05066
0.59917	-0.04312
0.6489	-0.03506
0.69875	-0.02676
0.74872	-0.01858
0.79881	-0.01096
0.84901	-0.00438
0.89931	0.00051
0.94968	0.00286
1	0

Table II. Geometry of modified airfoil

1	0.0038703
0.95032	0.0136503
0.90069	0.0240403
0.85099	0.0351703
0.80119	0.0466703
0.75128	0.0582503
0.70125	0.0695103
0.6511	0.0801303
0.60083	0.0898303
0.55046	0.0983303
0.5	0.1053503
0.44946	0.1105903
0.39886	0.1137303
0.34823	0.1144503
0.2976	0.1124103
0.24699	0.1077203
0.19645	0.1001903
0.14602	0.0894703
0.09577	0.0747403
0.07007	0.0652603
0.04593	0.0536203
0.0214	0.0384203
0.00945	0.0279703
0.00487	0.0222003
0.00267	0.0187103
0	0.0038703
0	0
0	-0.0024381
0.00733	-0.0152781
0.00733	-0.0152781
0.01013	-0.0179001
0.01555	-0.0222581
0.0286	-0.0295481
0.05407	-0.0395481
0.07923	-0.0468681
0.10423	-0.0526201
0.15398	-0.0611181
0.20355	-0.0669181
0.25301	-0.0704881
0.3024	-0.0720981
0.35177	-0.0710101
0.40114	-0.0694581
0.45054	-0.0653581
0.5	-0.0597981
0.54954	-0.0530981
0.59917	-0.0455001
0.6489	-0.0374961
0.69875	-0.0291961
0.74872	-0.0210181
0.79881	-0.0133981
0.84901	-0.0066101
0.89931	-0.0019281
0.94968	0.0004219
1	-0.0024381

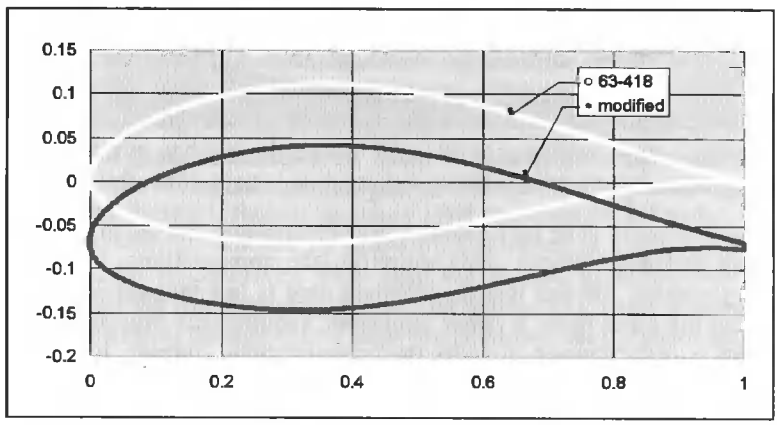

Fig. 2. Surface points obtained by smoothing of the data from Tab. I and Tab. II

The geometry of the evaluated airfoils was provided in the form of data point tables, reproduced here as Tab. I (for the basic shape) and Tab. II (for one of the modifications). The number of the data points in the tables is small (only 24 per surface in Tab. I). Using these data directly as the definition of the computational domain geometry would produce an unsuitably discontinuous broken line. The first step in the preparation of the domain geometry had to be an interpolation smoothing. The procedure used was 4th order curve fit. The resultant surface data table contained a much larger number, 994 data points. In the modified airfoil case of Tab. II, the smoothing was done separately for the upper half and the bottom half of the profile, avoiding the leading-edge as well as the trailing-edge segments at the locations where the geometry had to retain the discontinuities of the surface line. The resultant geometry of the surfaces is best seen in Fig. 2, which is actually a plot of the positions of the 994 data points. The distances between them are so small that in Fig. 2 the result seems to be a continuous line.

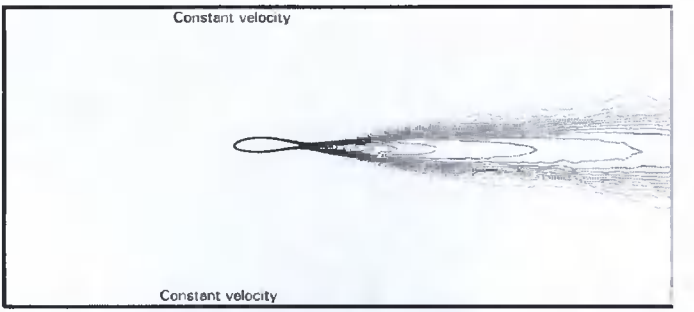

Fig. 3. Boundary conditions used in the computations. Constant velocity is specified on the dark boundary at the left-hand side inlet and also on top and bottom boundaries. The constant pressure condition is specified on the right-hand side exit. This is a case of the modified airfoil at zero angle of attack. The lines in the wake represents the constant values of turbulent viscosity

The smoothed airfoil sections were then placed into rectangular domain boundaries in which the grid was later set up. The author's inexperience has initially led to wasting time by computations with improperly chosen conditions before finding that to simulate the wind tunnel test section, the constant pressure condition has to be applied only at the exit (Fig. 3) with velocity conditions elsewhere. To suppress the problems often stemming from imperfect simulation of the boundary conditions at the domain boundaries, the domain size was chosen very large. The scale picture Fig. 3 gives an idea about the relatively small size of the airfoil placed in the domain 9 chord lengths long (in the streamwise direction) and 4 chord lengths high.

The grid chosen for the computations was an unstructured triangular grid – based upon the author's earlier positive experience. This grid may perhaps lead to less accurate results than ordered grids when compared on element vs. element basis for elements of comparable size, but this is more than offset in the used software FLUENT by the capability of adaption: a gradual refinement in the course of the solution so that the grid elements become smaller in the regions where the flow is more sophisticated. The availability of the Sheffield White Rose High Performance Computer Grid was made use of for working with really large number of mesh elements enabling much higher resolution than achievable just several years ago.

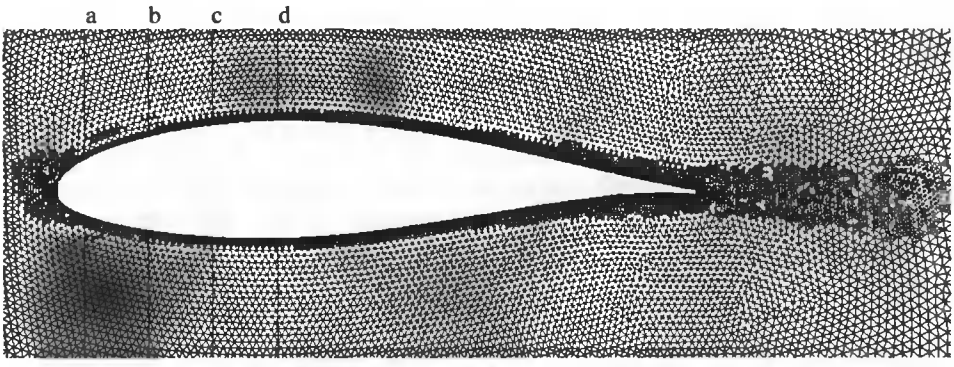

Fig. 4. Typical example of a detail of the computation mesh in the vicinity of the airfoil – in this case the modified airfoil of Tab. II at zero angle of attack. The four lines a, b, c, and d were used to evaluate velocity profiles

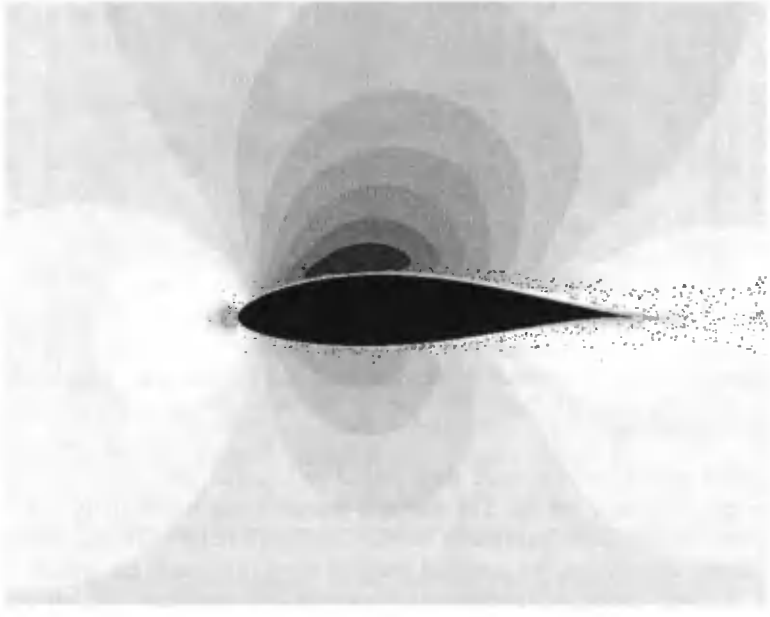

Fig. 5. An example of the computed absolute velocity distribution in the vicinity of the airfoil – in this case the baseline NACA 63-418 at zero angle of attack. The velocity was originally colour coded (here reproduced as grey shades): large changes of grey shades in a small spatial region are indicative of large velocity gradient locations, where the computation has to be performed with higher accuracy than elsewhere

The number of mesh elements varied between individual runs because of the different results of the refinement adaptation procedure in each case. To give a specific example, the grid used to compute the baseline section at 0 deg angle of attack had finally 130 436 triangular cells, 205 255 faces and 74 819 nodes. Other grids used were of very similar size.

The upstream condition of constant velocity (Fig. 3) is obvious. The requirement was to perform the computation for the chord Reynolds number value

Re_c = 3.00E+06 and to ease the geometric conversions, the section chord length was chosen to be simply c = 1 m. For air specific volume v = 0.816326 $m^3 \cdot kg^{-1}$ (the value inserted automatically by FLUENT for what is considered the standard conditions) and the air kinematic viscosity ν = 1.460735 E-05 $m^2 \cdot s^{-1}$, the constant velocity at the left-hand side (upstream) domain boundary was 43.822 $m^2 \cdot s^{-1}$.

3. COMPUTATION RUNS

The solution of the flowfield equations was performed with the standard software FLUENT based on the finite volume discretisation of the computation domain. The used solver was the Segregated Implicit – steady version with cell-based absolute velocity formulation. The version used was the latest FLUENT 6.1.22, supplied by FLUENT Inc.. This is a general purpose software and as such it expects the computed boundary layers to be turbulent – as it is in the absolute majority of cases in engineering tasks. Neither it nor GAMBIT used to generate the mesh expect the laminar character. GAMBIT, therefore, does not distribute the discretisation nodes accordingly at and near the leading edge. In the present computation, this problem was circumvented to a degree by using the adaption procedure, with the software automatically refining the computation mesh during the solution run in the regions of higher velocity gradient. Subsequent analysis of the results has unfortunately shown that too much hope was pinned on the refinement procedure. The remedy achieved is far from perfect and cannot eliminate completely the consequence of the initial distribution unsuitable for this special case. Sorely needed mesh nodal points in the laminar boundary layer region were missing. Nevertheless, this was not immediately apparent during the computations and this is an area for possible future improvement of the presented results.

Initially, the author used the k-ε turbulence model [2] with rng modification for low turbulence Reynolds numbers. This model was found reliable in internal flow problems solved earlier. Unfortunately, later comparisons with known experimental data has shown a considerable discrepancy: too high drag, obviously caused by improper handling of turbulence. Although this was later found to be to a large degree caused not by the model itself but by a turbulence inadvertently introduced into the incoming flow, an improvement was sought in using another turbulence model. In published literature on analogous airfoil computations [4], preference was given to the k-ω turbulence model due to Menter [8] and it was also used for all the present computation runs. The standard version (non-SST) was used with the shear flow corrections as provided by FLUENT. The set of the model constants was not adapted, either. It was taken over as provided by the software supplier: α^*_{inf} = 1.0 α_{inf} = 0.52, β^*_{inf} =0.09, β_i = 0.072, R_β = 8, ζ^* = 1.5. The value of the Prandtl number for diffusion transport of fluctuation energy had value (surprisingly large) 2.0. Computations were run with very small convergence criterion value 1E-05 for relative continuity residual and larger (but still small by usual standards) 1E-04 residual for the relative fluctuation energy. Dynamic adaption of the grid was run automatically at each 20th interval, with the velocity magnitude refinement threshold 0.0006 using the curvature method.

Due to lack of experience with laminar airfoils as a specific type of flowfield computation task, the author's progress has been slowed by several wrong starts,

resulting in wasted time and effort. The problems with the boundary conditions and the turbulence model were already mentioned. Another unforeseen problem was caused by the turbulence in the incoming flow, a small value of which is automatically inserted by FLUENT as the boundary condition in turbulent flow computations. The reason for this step is that the solved transport equations do not start easily from a zero initial value on one hand – and, on the other hand, users of the software usually do not possess any information about the turbulence at their inlet locations. The small value enables the computation process to start smoothly and the value of the inserted numerical boundary value is usually insignificant because the solution converges quite rapidly – after a short distance downstream – to the proper local values. The author has been using this feature for a long time, did not expect a problem, and initially did not eliminate this feature. The turbulence, however, did not die out in the nominally "potential" outer flow. Although the computations with the incoming turbulence were made unintentionally, the effort spent on them is not lost. The results provide an important warning if the airfoil designed for operation in undisturbed atmosphere is used in a turbulent environment. This is not just a theoretical possibility if used for wind electricity generator rotors, where the airfoil may be expected to work inside the Earth's atmospheric boundary layer, which – especially over a complex terrain – may exhibit large turbulence levels [9] and the results derived for aeronautical applications under the assumption of unperturbed air may be quite misleading.

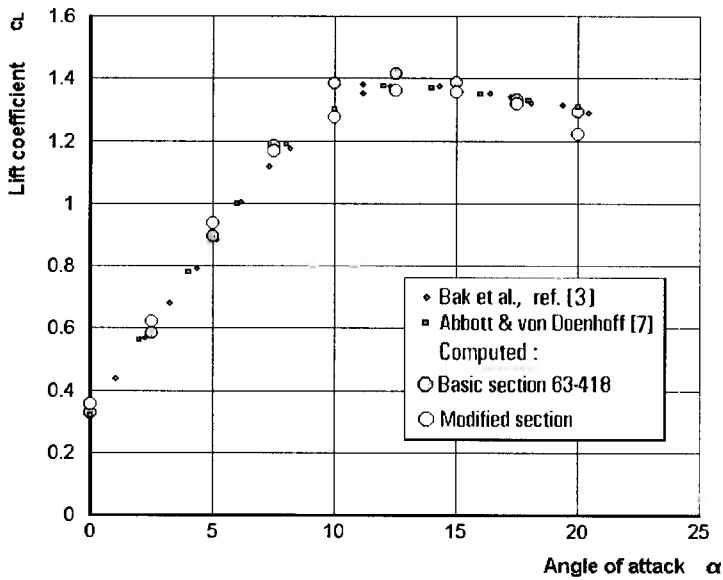

Fig. 6. Computed section lift coefficient for both baseline and modified airfoils, compared with values from literature [3, 4] documents an excellent agreement. Quite surprisingly, in view of the expected deterioration of performance by the modification, the computed values for the modified airfoil show an improvement – small but systematic increase in the lift coefficient values

In classical 'hand' computations, the drag D and lift L used to be evaluated separately, by different approaches. Lift is essentially determined by the configuration

of the streamlines in the flowfield outside of the boundary layer. For unseparated flow, at small attack angles, it may be evaluated with quite good precision by computing simply the external potential flow, neglecting the boundary layer completely (the contribution of which, through transverse component of friction force is insignificant). Only when the boundary layer separates its properties (by determining the location of the separation point) influence in a significant measure the evaluated lift. On the other hand, the potential flow solution is known to lead to the zero drag D'Alembert paradox. Drag is essentially determined by the boundary layer. Its value for laminar airfoils is small, by roughly two decimal orders smaller than that of the lift force. Computing such a small effect accurately side by side with the large lift force is difficult – the errors are comparable, but represent a large percentage of the drag while being just a small percentage of the lift.

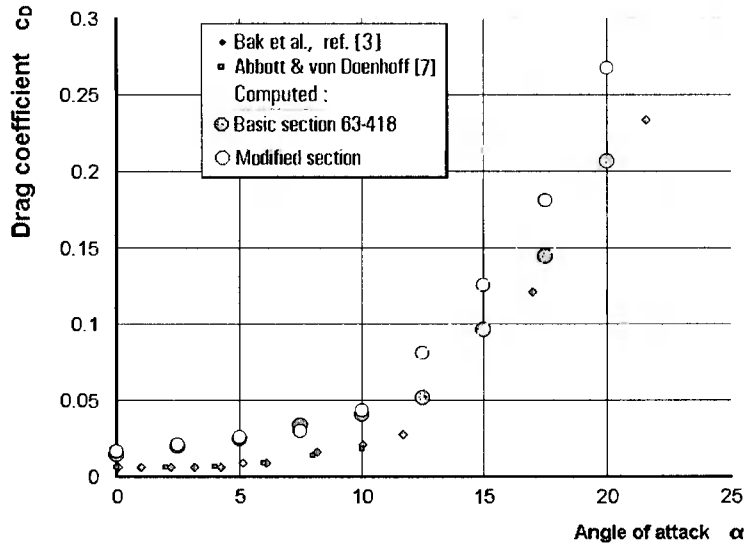

Fig. 7. Computed section drag coefficient values as a function of the angle of attack. Predictably, comparison with experimental data from [3], [4] presents a much pleasant picture: computed values are roughly twice as high

The comparison of the computed values with available experimental data for NACA 63-418 from references [3] and [7] is in Fig. 6 for the drag coefficient and in Fig. 7 for the lift. As expected, the agreement in the case of the lift is better than that for the drag. The agreement of lift data lift may be described as excellent. On the other hand, the computed drag values are roughly twice as high as the experimental ones at small angles of attack, where the latter is determined by the conditions in the boundary layer.

The computations of the flow past the modified airfoil given by Tab. II differ from the baseline airfoil runs only in different number and different distribution of the discretisation elements resulting from the adoption refinement. The mutual comparison of the two shapes is therefore quite reliable. The modification was expected to result in deterioration of the aerodynamic performance, drag rise and lift decrease – perhaps a considerable deterioration considering the well known sensitivity of the laminar sections to deviations of their geometry. It came as a surprise that the lift and drag

results of the two geometries actually differed only insignificantly. In fact, at small attack angles Fig.7 actually shows a surprising small but systematic increase in the generated lift. The drag the at small attack angles α is slightly higher as expected – but this trend is reversed as the separation is approached and at 10 deg the drag is actually lower. This value of α is the same at which lift becomes worse – and by the largest difference. The most significant deterioration due to the modification is seen to be in Fig. 7 the separation at a smaller – roughly by 2 deg – angle of attack.

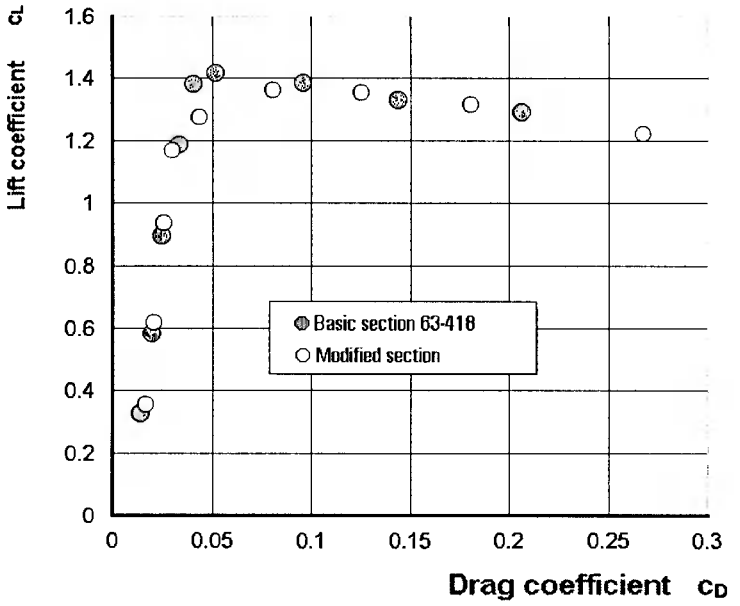

Fig. 8. Superimposed polars of the two airfoils given by Tabs. I and II. The change caused by the modification may be interpreted mainly as an increase in the effective value of the angle of attack. Both cases look remarkably similar. The only significant difference is only in the location of the maximum achievable lift – which seems to be smaller for the modified airfoil

The small differences in generated aerodynamic forces are the more surprising that the computed flowfield actually exhibits a visible change due to the modification. Since the modification by the insertion of the band between the two halves of the original airfoil influences mostly the shape near the leading as well as trailing edge, most changes were expected to take place there. very little was expected to happen above and below the modified airfoil, in contact with the surfaces that were not changed. Surprisingly, there was a visible change in the shape of isotachs above as well as below the airfoil and little if any change in shapes front and aft.

The unexpected changes of the generate lift at small angles of attack due to the modification lead to interesting result when plotted in the form of the section polar diagram. This is done in the next Fig. 8 and provides an surprisingly simple explanation of the observed variations. The data points for both investigated airfoil cases are found to lie on an essentially identical polar curve. The small deviation found at zero attack angle may be significant – we can expect a smaller minimum drag for the thinner of the

two airfoils – but there are not enough data there to support this conjecture. Otherwise the modified airfoil behaves in a more or less identical manner as the original baseline airfoil. What the modification mainly does is an increase in the effective value of the angle of attack – in accordance with the wedge shape of the inserted band.

Another perhaps significant (but again difficult to claim due to the scarcity of data) difference is observed near the maximum lift location, where the separation of the boundary layer from the airfoil surface begins. The immediately observable earlier separation in Fig. 7 may be also explained as a consequence of the increase in the effective value of the angle of attack. At the top of the polar diagram, however, there are differences that (provided they are real and not just a result of data scatter) may be significant: the thicker modified airfoil does not reach the maximum lift provided by the original section.

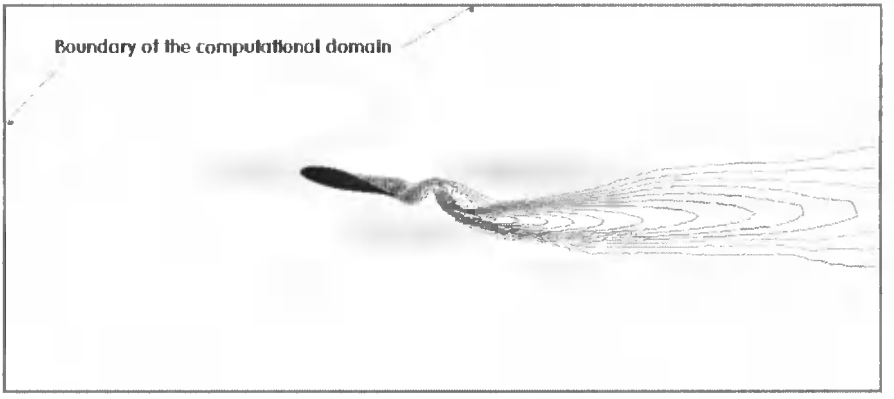

Fig. 9. An example of the computations for large attach angle – in this case the modified profile at $\alpha = 15$ deg. The instability of flow in the separated region causes problems with convergence of the numerical solution. Shown here are the lines of the constant value of turbulent viscosity. They seem to generate an impression of an unsteady flow with vortex shedding. This, of course, cannot be true – the flow is computed as steady. The problem is, however, with a change in the character of the flow to which the flow pattern tends to converge: before a convergence is achieved, a change occurs and the flow tends to converge to a different configuration

The separated flows proved to be the most difficult to compute. This is due to numerical instability – which, no doubt, reflects the physical hydrodynamic instability of the flowfield. Instead of the simple monotonous convergence to a converged steady state, the solution tends to oscillate between different states towards which it has a tendency to settle. Before a full settling occurs, even small changes caused by events in the computation process suddenly change the course of the progress. The solution begins to converge to a different flowfield – Fig.9. When the residuals (differences between the two sides of the solved equations, which ideally should be equal to zero for the particular equation being fulfilled) are plotted as a function of the iteration number, the diagram shows strong oscillations. Relaxation can help, but to be effective it has to be much larger than usual resulting in much slower convergence. At any rate, the values obtained from the solutions computed for the separated flow conditions are less reliable.

4. DISCUSSION

The much larger error obtained for the drag coefficient at the small attack angle values did not come as a surprise. Firstly, the computed drag is small and therefore more prone to be influenced by errors. The solved equations are nonlinear and the errors therefore need not be distributed symmetrically relative to the correct value. However, a more important factor in the shift of the solution results towards higher values is the improper handling of the transition into turbulence. Another related reason is quite a probable improper handling of low Reynolds number turbulence, which is notoriously difficult to model properly and is responsible for rendering the behaviour of the boundary layer immediately after its transition to turbulence. These three possible reasons for the error are inherent to the used computation model and a user has little or no opportunity for correcting them: toying with some constants of the model, which is tedious and uncertain.

What may also be one of the causes of the discrepancies and yet provides some chances for improvement is resolution of the flow in the boundary layer – especially, of course, in the laminar boundary layer formed on the front part of the airfoil. The adaption refinement process was relied upon to ensure proper number of the finite volumes and their placement. The results show, however, that results still depend upon the starting configuration – the initial distribution of the nodal points created by GAMBIT software. Since the software is built for another (more typical) sort of solved problems (turbulent shear flows), the effectiveness of the element distribution it generates may be questioned.

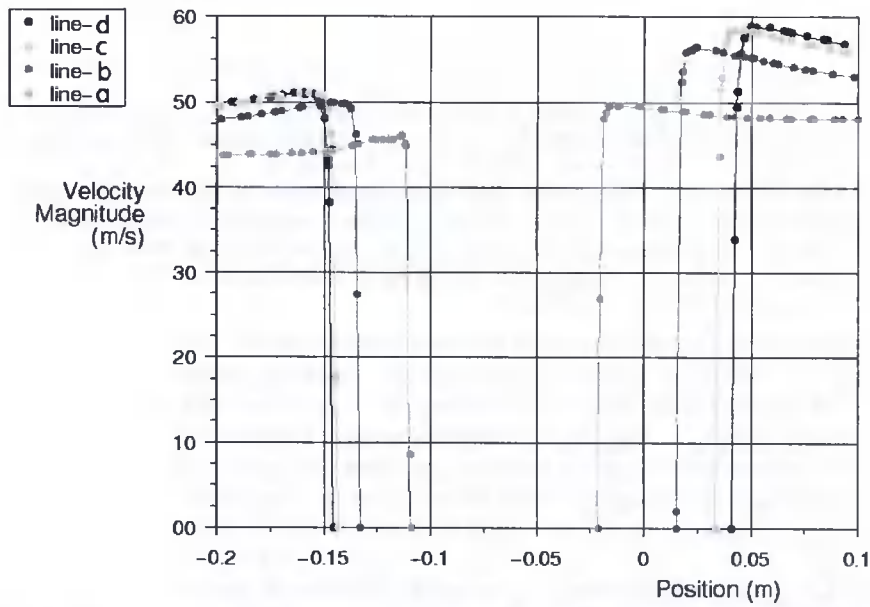

Fig. 10. Enlarged central part of the profiles of absolute velocity magnitude along the four lines a, b, c, and d shown in Fig.4. Despite the very dense distribution of the nodal points further away from the airfoil surface, this detail of the boundary layers shows that the points are quite scarce in the most important locations inside the boundary layer

To obtain some information about the actual density of the nodal points in the boundary layer in the performed computations, profiles of absolute velocity magnitude in the computed flowfield for the case of zero attack angle flow past the modified airfoil were evaluated along the four vertical lines a, b, c, and d perpendicular to the overall horizontal flow direction, as shown in Fig. 4. As for the profiles shown in Fig. 10, it should be noted that only the central part of the computational domain, in the very vicinity of the investigated airfoil is shown (the domain width is 4 metres). The points in the diagram Fig. 10 represent the vertices of the discretisation triangles. It is evident that the distribution of these nodes is extremely dense in the outer parts of the flowfield, outside the boundary layer. The points there are so densely located that they form practically a continuous line. Nevertheless inside the boundary layer itself the distribution is visibly worse. It immediately shows that the number of the data points inside the boundary layer is too small. The resolution of the conditions inside the boundary layer is poor. Considering this poor resolution, it seems surprising that the computed friction on the wall, which determines the drag in this part of the airfoil, is evaluated at all with some accuracy.

The conclusion from the analysis of the conditions in the most important region inside the boundary layer is that the used procedures for placement and refinement of the discretisation element did not do their job as expected. It was probably designed for different conditions. In the approach used a sufficient number of the nodal points inside the layer could be obtained only by many times more repeated refinement procedure – but this would produce too many points outside the boundary layer so that the computations would be unacceptably slow.

5. CONCLUSIONS

1. The objective of the computations was attained: it was possible to compare the aerodynamic performance of the baseline section NACA 63-418 and its modified versions.
2. Both section shapes behave in much more similar manner that could be expected on the basis of their considerable difference (larger thickness of the modified airfoil) and distinguishable differences of the flowfield. They, in fact, tend to follow what seems to be identical polar diagram curve. The main difference caused by the modification tends to be the increased effective angle of attack. However, the modified profile does not attain the same maximum lift and is more prone to flow separation, but the differences are rather small.
3. Computations can show how the aerodynamic performance of both airfoils may be substantially influenced by turbulence in the incoming flow.
4. The used computational resources were operated near their practical limits regarding e.g. the number of the used discretisation elements. The size of the computational domain was chosen perhaps too generously large.
5. The used general purpose CFD software computed almost exactly the generated lift – to an error less than 3% at small angles of attack. On the other hand, the computed drag is much higher than experimental data in this region. It was computed with less than desirable accuracy, the error reaching typically 100% of the experimental value (or 50% of the computed value). At larger attack angles and especially for the separated flow, the drag is computed better – but the computations there are more

difficult, most probably due to the conditions reflecting the physical, hydrodynamic instability of the flow.

6. The information available does not permit estimating the influence of the generally recognised weakest spot of the numerical airfoil performance computations: the questionable reproducing of the laminar/turbulent transition and low Reynolds number turbulence. Regretfully, another source of disagreement could be identified: poor working of the discretisation refinement procedure which was expected to provide the desirable high resolution. It is obviously tuned to different flow conditions, more typical for general engineering. It certainly added unnecessarily discretisation elements outside the boundary layer while the resolution inside the layer, remained rather poor. This is an area where an improvement of accuracy in future computations is possible.

ACKNOWLEDGEMENT

Support of NEG Micon Rotors Ltd. and permission to publish the results are gratefully acknowledged.

REFERENCES

[1] Tesař V., 1990. Mechanika tekutin pro 4-leté studijní obory. Textbook for mechanical engineering students, CVUT Praha, Czech Republic.

[2] Tesař V., 1991. Mezní vrstvy a turbulence. Textbook for mechanical engineering students, CVUT Praha, Czech Republic.

[3] Bak C. et al., 1999. Airfoil Characteristics for Wind Turbines. Riso National Laboratory, Roskilde, Denmark.

[4] Bertagnolio F. et al., 2001. Wind Turbine Airfoil Catalogue. Riso National Laboratory, Roskilde, Denmark.

[5] Theordorsen T., 1931. Theory of Wing Sections of Arbitrary Shape. NACA Report 411.

[6] Abbott I.H., von Doenhoff A.E., 1959. Theory of Airfoil Sections. Dover.

[7] Abbott I.H., von Doenhoff A.E., Stivers L.S., 1945. Summary of Airfoil Data. NACA Report 824.

[8] Menter F.R., 1993. Zonal Two-Equations k-ω Turbulence Models for Aerodynamic Flows. AIAA Paper 93-2906.

[9] Garratt J.R., 1994. The Atmospheric Boundary Layer. Cambridge Univ. Press.

[10] Čarnogurská M., Peszyński K., 2004. Numeryczne modelowanie naprężeń łopatki turbiny wiatrowej. Międzynarodowa konferencja procesorów energii ECO – EURO – ENERGIA, Bydgoszcz, Poland, 333-340.

Review by prof. Józef Flizikowski

University Press
University
of Technology
and Agriculture
in Bydgoszcz

DEVELOPMENTS IN MACHINERY DESIGN AND CONTROL
Vol. 4 (2005) 117 – 126
Scientific Journal

Zdeněk Trávníček[a)1], Jan Hrubý[a)], Jiří Vogel[b)]
[a)] *Institute of Thermomechanics, Academy of Sciences of the Czech Republic*
Dolejškova 5, 182 00 Prague 8, Czech Republic
[b)] *Czech Technical University in Prague*
Technická 4, 166 07 Prague 6; Czech Republic

STABILITY AND CONTROL POSSIBILITY OF COAXIAL JETS

Abstract: Confined coaxial jets were investigated experimentally and numerically, the visualization was made in the air and the numerical simulation used software FLUENT. The study focuses on the limiting coaxial geometry when the outer diameter of the annular jet is identical with that of the confining round duct. A series of laminar flow patterns is presented. The patterns observed are comparable with a classification known from available literature. Certain differences in scenarios of the patterns were observed such as three-dimensional structures and helical modes. To portrayal these structures, a stereoscopic technique was employed. The passing frequency of several modes was evaluated stroboscopically. The results are considered important for basic research as well as for many applications.

Keywords: jets, stability, visualization, numerical simulation, flow control.

1. INTRODUCTION

Fig. 1 shows the investigated task, namely the confined coaxial fluid jets at the limiting geometry when the outer diameter of the annular jet is identical with that of the confining round duct. The coordinate system is shown in Fig 1 as well. The arrangement is sometimes referred to in literature as the merging flow in coaxial cylindrical pipes (Blyth & Mestel, 2001) or the laminar Craya-Curvet jets (Revuelta *et al.* 2004). Although problems of flow stability downstream the trailing edge of the inner pipe seem to be very interesting from both the fundamental and engineering application point of view, the available literature exhibits a great lack of information. A rare example is the conference paper (Gore & Crowe, 1988) discussing the behavior of the laminar flow field near the stability loss. Eight distinct flow regimes were identified by visualization experiments. The present paper describes a new investigation based on experimental and numerical approaches.

Flow field regimes. The flow field is classified by three parameters (Gore & Crowe, 1988): d/D, U_i/U_o and Re_i; where d and D are the inner and outer diameters (see Fig. 1), respectively. Further, U_i and U_o are the average velocities in the inner (round) and outer (annular) jets, respectively, and the Reynolds number is defined from the

[1]Corresponding author. *Tel.:* +420-2-6605-3302; *fax:* +420-2-8658-4695
E-mail address: tr@cas.cz (Z. Trávníček)

inner pipe flow $Re_i = U_i d/\nu$. Fig. 2 shows a map of parameters related to the flow regimes I to VIII.

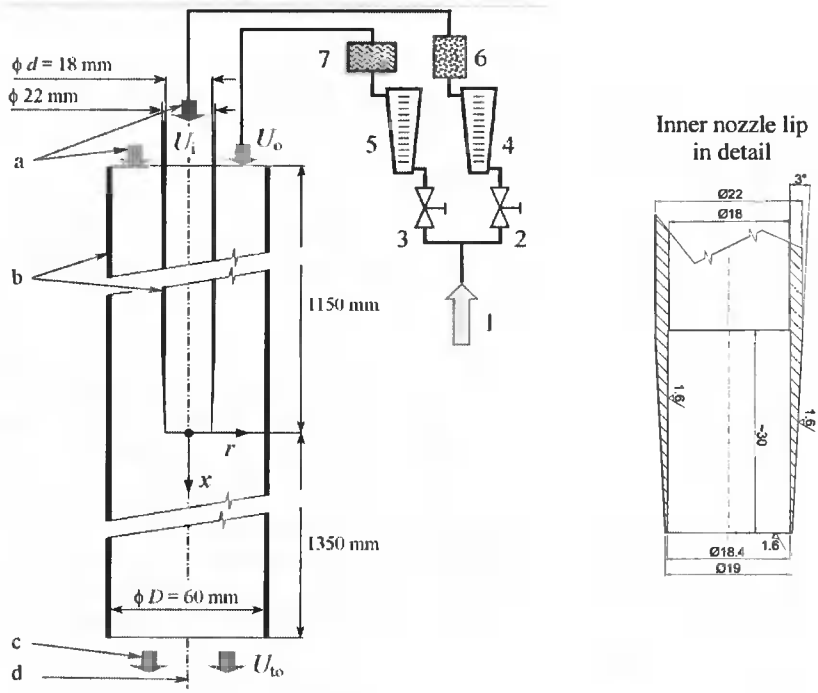

Fig. 1. Confined coaxial jet: 1 – air supply, 2 – throttle valve of the inner airflow, 3 – throttle valve of the outer airflow, 4, 5 – rotameters, 6 – fog/smoke generator, 7 – humidifier; U_i and U_o are the average velocities in the inner (round) and outer (annular) jets. The prescribed boundary conditions of the numerical simulation: a – inlets, uniform velocity profiles with velocities U_i and U_o; b – walls (no-slip boundary condition), c – outlet, d – axis

The qualitative classification according to (Gore & Crowe, 1988) is the following:

I Flow becomes turbulent shortly after leaving the inner jet.

II An appreciable laminar section before the onset of turbulent flow.

III A short laminar section before transition occurs, the flow initially *curves inward.*

IV Initially laminar flow rapidly becomes turbulent dispersing the tracer quickly; the faster outer fluid forms characteristic *long fingers* of the inner (slower) fluid pointing outward and in the downstream direction.

V Pseudo-turbulent flow; large eddies are formed *without rapid* (turbulent) *mixing.*

VI Long laminar section preceding transition to turbulent flow – similarly as II, but the tracer expands more rapidly.

VII Very similar to regions VI, except *a very slight back-flow* (visualized by the tracer) *along the duct wall.* After short time (~minutes) the entire volume near the wall is filled with tracer.

VIII Complete laminar flow and very little mixing.

The dotted curve $Re_{to} = 2300$ in Fig. 2 shows the critical Reynolds number of turbulence transition in the developed pipe flow, after mixing both inner and outer flows

(a well known value of 2300 is considered here). This curve can be derived from the continuity equation and from the definitions of both Reynolds numbers $Re_i = U_i d/\nu$ and $Re_{to} = U_{to} d/\nu$, where U_{to} is the (total) average velocity in the outlet (see Fig. 1):

$$Re_i = Re_{to} \frac{1}{\left(\frac{d}{D}\right)\left(\frac{U_i}{U_o}\right) + \frac{D}{d} - \frac{d}{D}} \tag{1}$$

Further, points in Fig. 2 show parameters of the present experiments, which will be discussed below.

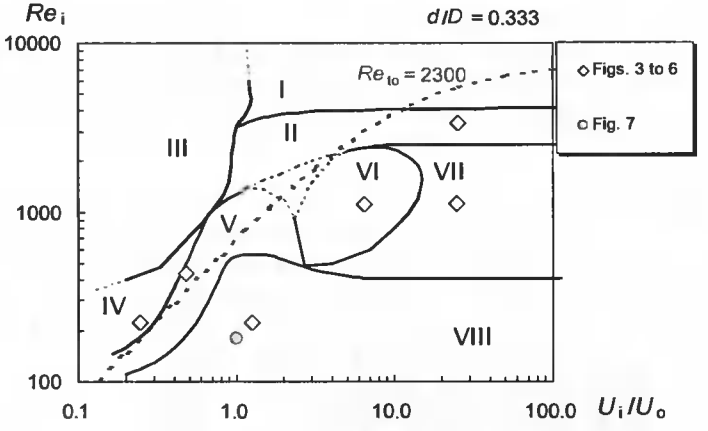

Fig. 2. Map of parameters related to the flow regimes I to VIII (Gore & Crowe, 1988); points denote experiments discussed in this paper

Motivation. At some atmospheric conditions, bursts of new aerosol particles (the so-called secondary aerosol) have been observed (*e.g.* Mäkela *et al.*, 1997). This phenomenon is important especially because of the influence of the atmospheric aerosols on the global climate evolution. The mechanism of the formation (nucleation) of the secondary aerosol particles is unknown. Traditional hypothesis is that the nucleation is due to the interaction of (mainly) water and sulfuric acid vapors. Sulfuric acid forms in the atmosphere by consecutive photo-oxidation of sulfur, which enters the atmosphere in volcanic eruptions or as a product of burning of fossil fuels. Understanding the process of water-sulfuric acid nucleation appears to be a great challenge to both experimentalists (Wyslouzil *et al.*, 1991) and theorists (Noppel *et al.*, 2002). We develop a new experimental method, based on laminar mixing (by molecular diffusion) of two vapor-saturated airflows. The inner flow is saturated with sulfuric acid vapor, and the outer flow is saturated with water vapor. Because of the strongly non-ideal thermodynamic behavior of the two components, the system becomes supersaturated after mixing, and new particles are formed by binary homogeneous nucleation. In the laminar flow field, the concentration profiles can be computed with good accuracy. By measuring the integral rates of particle production and by reconstructing the concentration (humidity and acidity) fields using numerical simulation (studied in this work), the dependence of the nucleation rate on the humidity, acidity, and temperature can be determined. Such knowledge is needed for assessing the relevance of the water-sulfuric acid nucleation for environmental application. To make the

laminar flow model correspond with the reality, the flow must be stable. The existence of the trailing edge at the end of the inner tube makes the question of flow stability highly nontrivial. Therefore, a large part of this work is devoted to this problem.

2. EXPERIMENTAL METHODS

Fig. 1 shows a schematic view on the present experimental setup. The entire facility is situated vertically and connected to pressurized air supply (1) through two flow branches. The inner and outer airflow rates are controlled by the throttle valves (2, 3) and measured by rotameters (4, 5) respectively. The average velocities U_i and U_o are calculated from the airflow rates.

The present flow visualization was made by a home-made fog/smoke generator 6. Optionally, either water fog or cigarette smoke were employed. Further, the outer jet supply was equipped width a home-made humidifier 7 to investigate an influence of air humidity gradient on the shear layer stability. Typical air temperature and humidity were, respectively, 25°C and 35% without the humidification, or 23°C and (75-85)% with the humidification.

An illumination was made by a flashlight. Contrasting white streaklines on black background were observed and photographed with a digital camera (OLYMPUS 2500). To investigate three-dimensional effects, a stereoscopic technique was employed: a pair of identical digital cameras were located at azimuthal angle 90° one towards the other. Since both camera shutters were open for a relatively long time (0.25s), the single flashlight guaranteed a synchronization of both photographs.

3. NUMERICAL SIMULATION

The fluid flow is assumed to be incompressible, isothermal, laminar, and stationary. The fluid properties (density and viscosity) are assumed to be constant. With these simplifications, two equations govern the mean velocity flow field: continuity and momentum (Navier–Stokes) equations. Moreover, to model mass transfer of multicomponent and multiphase flow including a condensation, mass transport equations of contaminant h (water vapor in the annular jet) and a (acid coming through the inner jet) were solved, too.

The flow field is computed with the commercial finite-volume code FLUENT, in implicit formulation, in absolute velocities. Continuity and momentum equation are coupled by the SIMPLE algorithm, which works in predictor–corrector steps, (Patankar, 1980). The segregated solver applied has been traditionally used for incompressible and mildly compressible flows. A standard scheme is used for the pressure discretisation, and first order upwind is used in the momentum. The multi-grid method to accelerate the convergence, and iterative technique with under-relax predictions of the velocity and pressure are applied. Default under–relaxation factors of the solver were used, which were 0.3 and 0.7 for the pressure and momentum, respectively. The results of iterations were evaluated by means of convergence criteria based on residual evolutions. The solution was considered to be converged when the sum of normalized residuals was less then $1 \cdot 10^{-3}$ with the exception of the water vapor and the acid where residuals have been less then $1\ 10^{-5}$. The present computations were performed using the common PC multiprocessor Silicon Graphic computer, and usually took from half an hour to one hour per a task.

The domain, grid, boundary conditions, and input data. The geometry of the computational domain was used basically the same as at experiments (see Fig. 1). The unstructured axi-symmetrical grid of mixed cells had 3717 volumes and 39702 nodes. The prescribed boundary conditions (a–d) are plotted in Fig. 1, and are as follows:

a) inlets. Since the tube length was set to be long enough (64*d*), the velocity profiles at the inlets were set as uniform (velocities U_i, U_o). Three tasks with different ratio of inner/outer jet velocities were simulated: (A) $U_i/U_o = 0.5$, (B) $U_i/U_o = 1.0$, and (C) $U_i/U_o = 2.0$. The values U_i, U_o were given to satisfy approximately a condition $U_{to} = 0.03$ m/s, it means Re_{to}– value was approximately 120.
b) walls: A no-slip boundary condition, i.e., all velocity components are zero.
c) outlet: A static pressure was prescribed as reference value, 101325 Pa.
d) nozzle axis: standard symmetry conditions were employed.

Fluid properties of working fluid (nitrogen): fluid density, fluid density as incompressible ideal gas; dynamic viscosity, $\mu = 1.72\text{x } 10^{-5}$ kg·m^{-1}·s^{-1}).

4. VISUALIZATION EXPERIMENTS – RESULTS AND DISCUSSIONS

Fig. 3 shows typical flow patterns II, IV to VI (regimes I and III were out of possibilities of the present facility). These flow patterns are comparable with a classification given by (Gore & Crowe, 1988). The following paragraphs focus on four phenomena which have not been referred in the available literature yet (in relation to the confined coaxial jets).

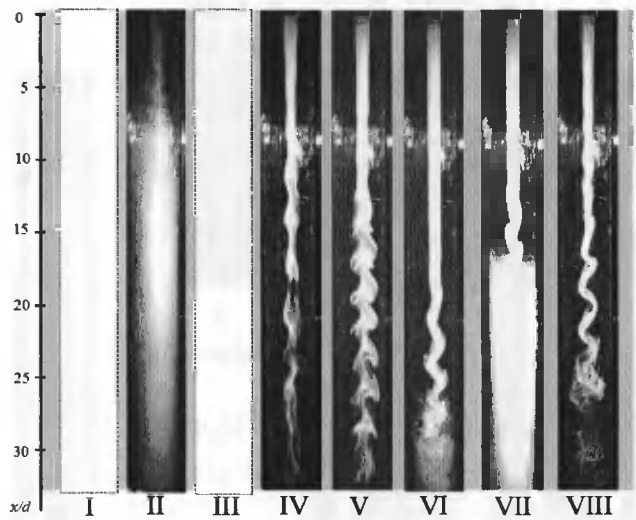

Regime	I	II	III	IV	V	VI	VII	VIII
U_i/U_o	---	25.5	---	0.24	0.48	6.43	24.6	1.25
Re_i	---	3380	---	224	436	1130	1130	224

Fig. 3. Visualisation of flow field in the denoted regimes

Three-dimensional effects versus two-dimensional 'polarization' of fluid columns. Figs. 4 and 5 demonstrate the effect of the two-dimensional 'polarization' of the inner fluid jet during its stability losses. These pairs of synchronized photographs were made

with a pair of identical cameras (L, R), under identical parameters. Figs. 5 L, R were made a few minutes after Figs. 4 L, R. The instability of the jet columns is developed mainly in a specific plane (e.g., Fig. 4 R), however, a slow (or irregular) circumvolution of this plane occurs. After few minutes, the pattern is turned approximately by azimuthal angle 90°, as it is demonstrated by a comparison of Figs. 4 and 5.

Helical mode of the patterns. Figs. 6 L, R demonstrate a helical mode of the flow pattern, or the typical 'corkscrew' face of this mode. It was frequently observed in regime V, and it was very rare at the other regimes.

Vortex passing frequency. It is a well known fact that the Strouhal number of the fundamental frequencies of unconfined axisymmetric jets vary from 0.3 to 0.6, and that the value of 0.3 is in tune with the most preferred mode (i.e. the most amplified mode obtained by an artificial external excitation) – see e.g. Crow & Champagne (1971). The passing frequency of the present task was evaluated stroboscopically, and the resultant values of Strouhal number ($St = f\ d/U_i$) ranged from 0.4 to 1.2 for $Re_i < 700$, in agreement with the expectation.

Effect of air humidity gradient on the shear layer stability. Four sets of experiments were made, which varied in the inner/outer jet fluid: (a) dry air with cigarette smoke/dry air, (b) water fog in practically saturated air/dry air, (c) dry air with cigarette smoke/humidified air, (d) water fog in practically saturated air/humidified air. Repeatedly, a stability of these combinations follow the mentioned order 1 – 4, e.g., the dry air jet was more stable than of the humidified one, and the coaxial jets humidification evidently decreases the stability of the pattern. This effect was demonstrated at $Re_i = 144$ and 180 with the same results, Fig. 7 shows typical results for $Re_i = 180$, at $U_i/U_o = 1.01$, i.e. in regime VIII.

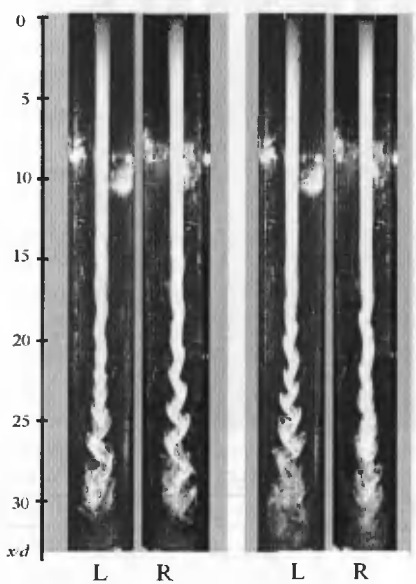

Fig. 4. Stereoscopic visualization

Fig. 5. Stereoscopic visualization

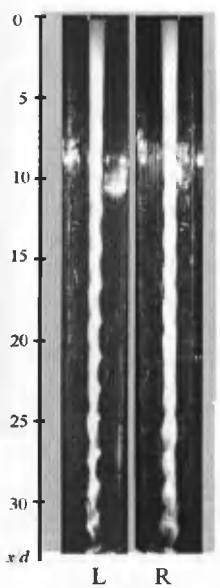

Fig. 6. Helical (or 'corkscrew') mode of regime V ($Re_i = 436$, $U_i/U_o = 0.64$)

The reason of the effect of destabilization by humidity can be linked either with density or enthalpy changes. Although the density decrease caused by air humidification seems to be rather small (about 0.5% in the present experiments), it can cause these effects as a result of great receptivity of flow fields near stability losses. On the other hand, the enthalpy increase may be even more significant, because the humidification technique causes quite a big increase in enthalpy from 42 kJ/(kg of dry air) to 65–75 kJ/(kg of dry air), i.e. by 55%–78% at the present experiments! It is fair to say here that an understanding of this effect is very far from complete, thus it remains an interesting challenge for the future.

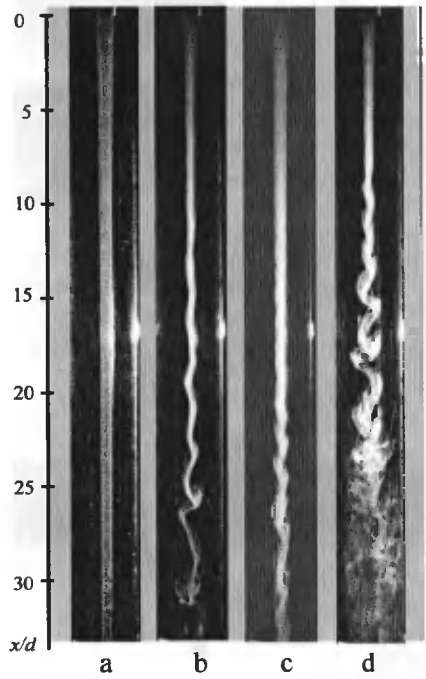

Fig. 7. Destabilization effect of air humidity

5. NUMERICAL SIMULATION – RESULTS AND DISCUSSIONS

Fig. 8 shows typical results as the flow field pathline for three simulated tasks A, B, and C. Fig. 9 shows concentration of the acid (coming from the inner jet) in a form of a distribution of the acidity in the mixture $Ra = p_a/p_{sa}$, where p_a is the actual partial pressure of acid, and $p_{sa}(T)$ is the saturated vapor pressure of acid at given temperature. Similarly, Fig. 10 shows the concentration of the water (coming from the annular jet) as the humidity of gas $Rh = p_h/p_{sh}$, where p_h is the actual partial pressure of water vapor, and $p_{sh}(T)$ is the saturated pressure of water vapor at a given temperature (only task B is shown here). The distribution of concentration of both fractions, h and a, results in the nucleation rate (e.g., Wyslouzil *et al.*, 1991), which is plotted in Fig. 11 for task B.

Fig. 12 shows computed velocity profiles for the tasks A, B, and C. Laminar mixing takes place predominantly at $x < 14d$, and the last two profiles $x = 14d$ and $44\ d$

are nearly the same (independently on the inlet boundary conditions, i.e., for all the three tasks. To illustrate this effect, Fig. 13 shows these velocity profiles in the spatial coordinates $r/d - x/d$.

Fig. 8. Computed pathlines at different ratios of inner/outer jet velocities

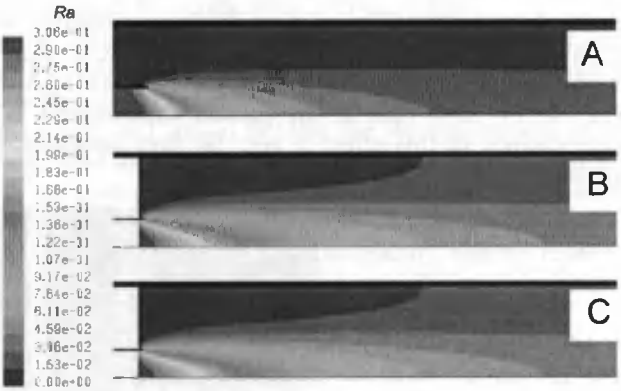

Fig. 9. Concentration of the acid: (A) $U_i/U_o = 0.5$, (B) $U_i/U_o = 1.0$, (C) $U_i/U_o = 2.0$

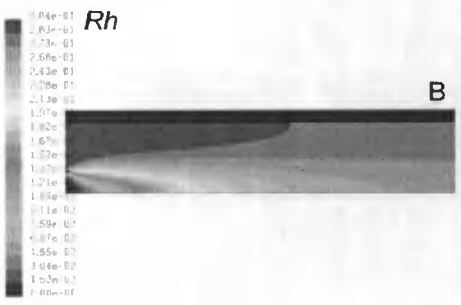

Fig. 10. Concentration of the water at (B) $U_i/U_o = 1.0$

Fig. 11. Nucleation rate at (B) $U_i/U_o = 1.0$

6. CONCLUSIONS

Flow visualization demonstrated a series of flow patterns, and the result is comparable with a classification known from available literature. Certain differences in scenarios of the patterns were observed such as three-dimensional structures (two-dimensional 'polarization' of fluid columns) and helical (or 'corkscrew') modes. The passing frequency was evaluated stroboscopically, and Strouhal number was evaluated from 0.4 to 1.2; in agreement with the expectation according to literature. Moreover, an effect of air humidity onto the stability was identified. The humidification causes a destabilization of the flow field. A possible explanation of this effect is supposed in relation to changes of fluid enthalpy, rather than simultaneous (and commonly referred to) influence of fluid density.

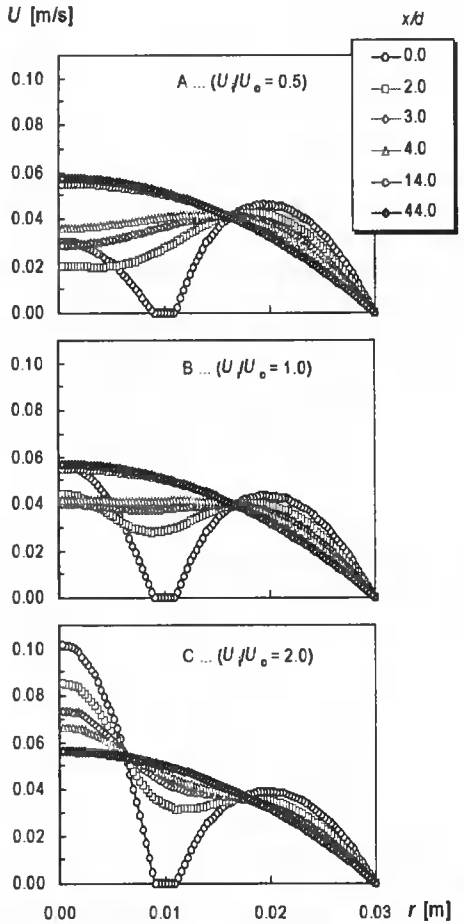

Fig. 12. Velocity profiles

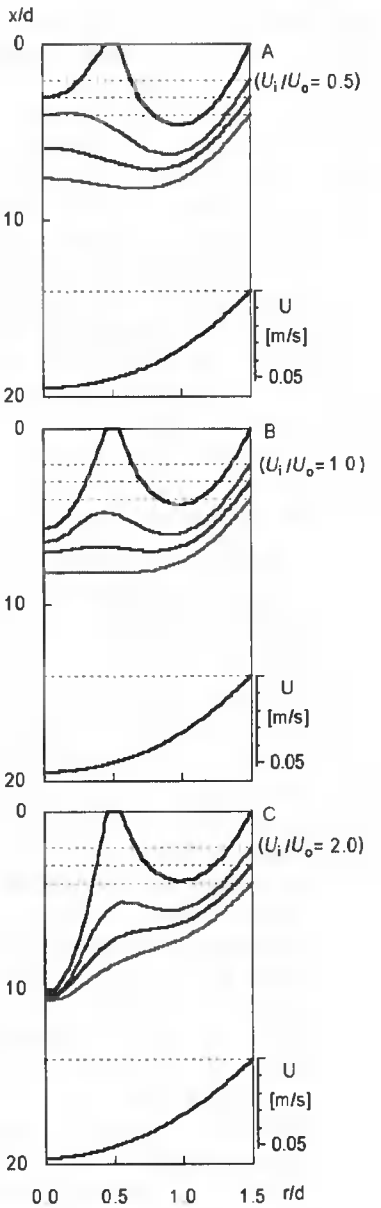

Fig. 13. Velocity profiles in the spatial coordinates

Numerical simulation focused on laminar mixing of both jets for three typical tasks differing in the ratio of inner/outer jet velocities. The flow fields were computed, and examples of pathlines and velocity profiles are presented here. Further, spatial distributions of concentration (acidity and humidity) and the nucleation rates were computed. The numerical simulation confirmed our prior conjecture (Hrubý, 2002) that nucleation occurs in a region resembling laminar flame. This situation is favorable for the purpose of the measurements. Visualization indicates that it is very difficult to find a regime, where the flow would be truly stable (without time-dependent component). In

some conditions, the laminar region extends far from the end of the inner tube. It is sufficient when the flow remains (practically) stable within the 'flame' area. The experiments indicate high susceptibility of the flow-field to minor disturbances. This fact will be respected in the design of the final experimental device for nucleation measurements.

The results are considered important for basic research as well as for many applications. The study is a step in development of a new method of basic investigation of aerosol formation out of gaseous precursors. The control of two–phase flow is essentially important in many applications such as in flow mixing, chemical reactors, and combustion processes. Apparently, periodic oscillations can potentially lead to enhancement of these processes. It should be helpful to correlate the natural frequency of flow (such as investigated passing frequency of large vortex structures) with a periodic external forcing. An efficient control can be achieved if a natural unsteady behavior of large–scale structures is in tune with a periodic external forcing. However, the present investigation deals with steady flows; a periodic forcing lies outside the scope of this study, thus it remains be a promising task for the future.

ACKNOWLEDGMENTS

We gratefully acknowledge the support by the Grant Agency of the Academy of Sciences of the Czech Republic (project No. A2076203).

REFERENCES

[1] Blyth M.G., Mestel A.J., 2001. Merging flow in co-axial cylindrical pipes. Q. J. Mech. Appl. Math. 54(4), 655-673.

[2] Crow S.C., Champagne F.H., 1971. Orderly structure in jet turbulence. J. Fluid Mech. 48, 547-591.

[3] Fluent User's Guide 6.1, 2002. Fluent 6.1 Documentation.

[4] Gore R.A., Crowe C.T., 1988. Observations on the flow in a confined coaxial jet. AIAA Paper 88-3591-CP, 940-945.

[5] Hrubý J., 2002. Laminar co-flow tube for measurement of nucleation rates in atmospherically relevant systems (Unpublished).

[6] Mäkelä J.M., Aalto P., Jokonen V., Pohja T., Nissinen A., Palmroth S., Markkanen T., Seitsonen K., Lihavainen H., Kulmala M., 1997. Observations of ultrafine aerosol particle formation and growth in boreal forest. Geophys. Res. Lett. 24, 1219-1222.

[7] Noppel M., Vehkamäki H., Kulmala M., 2002. An improved model for hydrate formation in sulfuric acid-water nucleation. J. Chem. Phys. 116, 218-228.

[8] Patankar S.V., 1980. Numerical Heat Transfer and Fluid Flow. Hemisphere Washington DC.

[9] Revuelta A., Martinez-Bazan C., Sanchez A., Linan A., 2004. Laminar Craya-Curvet Jets. Physics of Fluids 16(1), 208-211.

[10] Wyslouzil B.E., Seinfeld J.H., Flagan R.C., 1991. Binary nucleation in acid-water system. II. Sulfuric acid-water and a comparison with mehanesulfonic acid-water. J. Chem. Phys.,94, 6842-6850.

Review by prof. Jerzy Iwaszko

University Press
University
of Technology
and Agriculture
in Bydgoszcz

DEVELOPMENTS IN MACHINERY DESIGN AND CONTROL
Vol. 4 (2005) 127 – 132
Scientific Journal

Maciej Woropay, Bogdan Landowski[1], Daniel Perczyński
University of Technology and Agriculture, Department of Machine Maintenance
ul. Prof. S. Kaliskiego 7, 85–791 Bydgoszcz, Poland

AN APPLICATION OF THE MARKOV MODEL OF TECHNICAL OBJECTS MAINTENANCE PROCESS TO CONTROL THE SYSTEM IN WHICH THEY ARE UTILIZED AND MAINTAINED

Abstract: The paper analyzes the maintenance process of the system elements transforming electric energy in a chosen power supply system. Assuming that the homogenous Markov process X(t) is a model of the maintenance process of the transformer set, a state graph was built and possible transitions were determined based on the results from the maintenance investigations performed. Assuming that one of the process states is a consuming state, influence of controlling reserve element number value on the average system 'life time' was determined.

Keywords: homogenous Markov process, maintenance process of the distribution transformers

1. INTRODUCTION

The paper analyzes the maintenance process of the system elements transforming electric energy in a chosen power supply system (Fig. 1). The investigation object is mv/lv distribution transformers system, combined of five subsystems:

- working subsystem, comprising n, $n \geq 1$, elementary elements, being indispensable to perform the task E_1, E_2, ..., E_n,
- renovation subsystem situated at Power Supply Plant,
- renovation subsystem situated at an external Transformer Repair Plant,
- liquidation subsystem,
- reserve subsystem, comprising k, $k \geq 0$, reserve elements.

It was assumed that the homogenous Markov process X(t) is a model of the maintenance process of the transformer set. The process X(t) has finite phase space $S=\{1,2,3,4,5\}$, especially if:

$X(t) = 1$, then at the moment t a transformer is operating at a transformer station,
$X(t) = 2$, then at the moment t a transformer is at a repair stand SD,
$X(t) = 3$, then at the moment t renovation at a Transformer Repair Plant is being performed,
$X(t) = 4$, then at the moment t it is being liquidated,

[1]Corresponding author. *Tel.:* +48-52-340-84-95; *fax:* +48-52-340-84-95
E-mail address: lbogdan@atr.bydgoszcz.pl (B. Landowski)

X(t) = 5, then at the moment t a transformer is a reserve one.
Let $P_i(t) = P\{X(t)=i\}$ represent the probability that at the moment t the process X(t) is in state i. It is assumed that the initial state of the process is state S1, that means that the initial distribution assumes the following form:

$$P\{X(0) = 1\} = 1,\ P\{X(0) = i\} = 0 \text{ for } I = 2, 3, 4, 5.$$

The intensity of the transitions between the process states is included in the matrix Λ:

$$\Lambda = \begin{bmatrix} -(\lambda_1+\lambda_2+\lambda_3) & \lambda_1 & \lambda_2 & \lambda_3 & 0 \\ 0 & -\mu_1 & 0 & 0 & \mu_1 \\ 0 & 0 & -\mu_2 & 0 & \mu_2 \\ 0 & 0 & 0 & -\mu_3 & \mu_3 \\ \hat{\lambda} & 0 & 0 & 0 & -\hat{\lambda} \end{bmatrix}. \quad (1)$$

In order to simplify the notation, symbols $\lambda = \lambda_1 + \lambda_2 + \lambda_3$ were introduced.

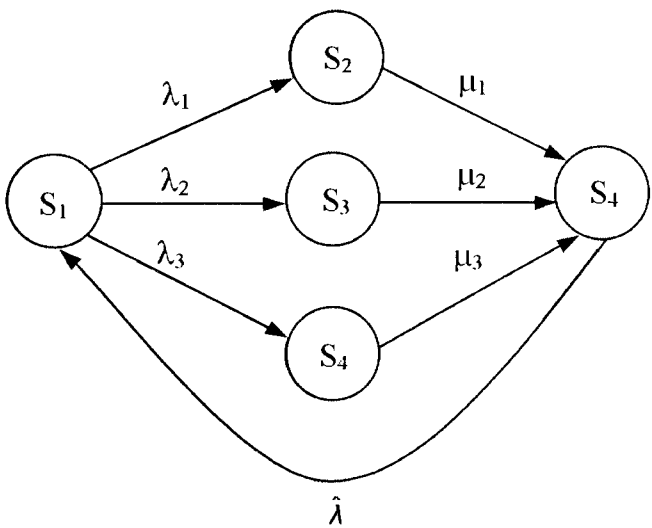

Fig.1. Digraph representing maintenance process of the distribution transformers

2. DETERMINING PROBABILITIES PI(T) BASED ON THE SYSTEM OF DIFFERENTIAL EQUATIONS BY A.N. KOLMOGOROV

The transition intensity matrix Λ allows us to build a system of differential equations of the following form:

$$\begin{aligned} P'_1(t) &= -\lambda P_1(t) + \hat{\lambda} P_5(t), \\ P'_2(t) &= \lambda_1 P_1(t) - \mu_1 P_2(t), \\ P'_3(t) &= \lambda_2 P_1(t) - \mu_2 P_3(t), \\ P'_4(t) &= \lambda_3 P_1(t) - \mu_3 P_2(t), \end{aligned} \quad (2)$$

$$P'_5(t) = \mu_1 P_2(t) + \mu_2 P_3(t) + \mu_3 P_4(t) - \hat{\lambda} P_5(t).$$

The system of differential equations (2) in the matrix notation takes the following form:

$$\begin{bmatrix} P'_1(t) \\ P'_2(t) \\ P'_3(t) \\ P'_4(t) \\ P'_5(t) \end{bmatrix} = \begin{bmatrix} -\lambda & 0 & 0 & 0 & \hat{\lambda} \\ \lambda_1 & -\mu_1 & 0 & 0 & 0 \\ \lambda_2 & 0 & -\mu_2 & 0 & 0 \\ \lambda_3 & 0 & 0 & -\mu_3 & 0 \\ 0 & \mu_1 & \mu_2 & \mu_3 & -\hat{\lambda} \end{bmatrix} \begin{bmatrix} P_1(t) \\ P_2(t) \\ P_3(t) \\ P_4(t) \\ P_5(t) \end{bmatrix}. \tag{3}$$

In order to obtain unambiguous solutions from the above mentioned system of equations, initial conditions should be adopted. Based on the initial distribution of the process X(t) it may be stated that:

$$P_1(0) = 1, \quad P_2(0) = P_3(0) = P_4(0) = P_5(0) = 0 \tag{4}$$

It is comfortable to solve the systems of linear differential equations by means of Laplace transforms which, when considering the initial condition (4), take the following form:

$$\begin{aligned} s\tilde{P}_1(s) - 1 &= -\lambda \tilde{P}_1(s) + \hat{\lambda} \tilde{P}_5(s), \\ s\tilde{P}_2(s) &= \lambda_1 \tilde{P}_1(s) - \mu_1 \tilde{P}_2(s), \\ s\tilde{P}_3(s) &= \lambda_2 \tilde{P}_1(s) - \mu_2 \tilde{P}_3(s), \\ s\tilde{P}_4(s) &= \lambda_3 \tilde{P}_1(s) - \mu_3 \tilde{P}_4(s), \\ s\tilde{P}_5(s) &= \mu_1 \tilde{P}_2(s) + \mu_2 \tilde{P}_3(s) + \mu_3 \tilde{P}_4(s) - \hat{\lambda} \tilde{P}_5(s). \end{aligned} \tag{5}$$

Taking into consideration denoting (1) the systems of equations (5) may be formulated as follows:

$$P'(t) = \Lambda^T P(t), \tag{6}$$

where:

$P'(t) = [P'_1(t), P'_2(t), P'_3(t), P'_4(t), P'_5(t)]^T$,

$P(t) = [P_1(t), P_2(t), P_3(t), P_4(t), P_5(t)]^T$.

The matrix presentation of the system of linear equations for the transform has the following form:

$$\begin{bmatrix} \lambda + s & 0 & 0 & 0 & -\hat{\lambda} \\ -\lambda_1 & \mu_1 + s & 0 & 0 & 0 \\ -\lambda_2 & 0 & \mu_2 + s & 0 & 0 \\ -\lambda_3 & 0 & 0 & \mu_3 + s & 0 \\ 0 & -\mu_1 & -\mu_2 & -\mu_3 & \hat{\lambda} + s \end{bmatrix} \begin{bmatrix} \tilde{P}_1(s) \\ \tilde{P}_2(s) \\ \tilde{P}_3(s) \\ \tilde{P}_4(s) \\ \tilde{P}_5(s) \end{bmatrix} = \begin{bmatrix} 1 \\ 0 \\ 0 \\ 0 \\ 0 \end{bmatrix}. \tag{7}$$

It is not difficult to solve the system of equations (7), however to perform reverse Laplace transform is impossible. Such a situation results from the fact that the main determinant of the system of equations (7) is a multinomial of the fifth degree related to variable s and it is difficult to distribute this multinomial into linear factors or quadratic ones for any values of the system parameters λ_1, λ_2, λ_3, μ_1, μ_2 and μ_3.

3. SIMPLIFIED MODEL ANALYSIS

Assuming that state S4 is consuming one that means $\mu_3 = 0$ (in practice it means that having liquidated a transformer, no new transformer is purchased), the system of differential equations takes the form of:

$$\begin{aligned} P'_1(t) &= -\lambda P_1(t) + \hat{\lambda} P_5(t), \\ P'_2(t) &= \lambda_1 P_1(t) - \mu_1 P_2(t), \\ P'_3(t) &= \lambda_2 P_1(t) - \mu_2 P_3(t), \\ P'_4(t) &= \lambda_3 P_1(t), \\ P'_5(t) &= \mu_1 P_2(t) + \mu_2 P_3(t) - \hat{\lambda} P_5(t). \end{aligned} \tag{8}$$

The Laplace transform of the system of equations (8), when taking into consideration the initial conditions, has the following form:

$$\begin{aligned} s\tilde{P}_1(s) - 1 &= -\lambda \tilde{P}_1(s) + \hat{\lambda} \tilde{P}_5(s), \\ s\tilde{P}_2(s) &= \lambda_1 \tilde{P}_1(s) - \mu_1 \tilde{P}_2(s), \\ s\tilde{P}_3(s) &= \lambda_2 \tilde{P}_1(s) - \mu_2 \tilde{P}_3(s), \\ s\tilde{P}_4(s) &= \lambda_3 \tilde{P}_1(s), \\ s\tilde{P}_5(s) &= \mu_1 \tilde{P}_2(s) + \mu_2 \tilde{P}_3(s) - \hat{\lambda} \tilde{P}_5(s). \end{aligned} \tag{9}$$

The system of equations (9), in the matrix notation, may be formulated as below:

$$\begin{bmatrix} \lambda + s & 0 & 0 & 0 & -\hat{\lambda} \\ -\lambda_1 & \mu_1 + s & 0 & 0 & 0 \\ -\lambda_2 & 0 & \mu_2 + s & 0 & 0 \\ -\lambda_3 & 0 & 0 & s & 0 \\ 0 & -\mu_1 & -\mu_2 & 0 & \hat{\lambda} + s \end{bmatrix} \begin{bmatrix} \tilde{P}_1(s) \\ \tilde{P}_2(s) \\ \tilde{P}_3(s) \\ \tilde{P}_4(s) \\ \tilde{P}_5(s) \end{bmatrix} = \begin{bmatrix} 1 \\ 0 \\ 0 \\ 0 \\ 0 \end{bmatrix}. \tag{10}$$

The system of equations (10) has been solved using Cramer's method. The main determinant of the system of equations is:

$$W(s) = \begin{vmatrix} s+\lambda & 0 & 0 & 0 & -\hat{\lambda} \\ -\lambda_1 & s+\mu_1 & 0 & 0 & 0 \\ -\lambda_2 & & s+\mu_2 & 0 & 0 \\ -\lambda_3 & 0 & 0 & s & 0 \\ 0 & -\mu_1 & -\mu_2 & 0 & s+\hat{\lambda} \end{vmatrix}. \tag{11}$$

Having completed the successive extensions and having calculated the determinant of the third degree, the following formula has been obtained:

$$W(s) = s(s+\lambda)(s+\hat{\lambda})(s+\mu_1)(s+\mu_2) - s\hat{\lambda}[\lambda_1\mu_1(s+\mu_2) + \lambda_2\mu_2(s+\mu_1)]. \tag{12}$$

The determinants have been determined by analogy:

$$\begin{aligned} W_1(s) &= s(s+\hat{\lambda})(s+\mu_1)(s+\mu_2), \\ W_2(s) &= s\lambda_1(s+\mu_2)(s+\hat{\lambda}), \\ W_3(s) &= s\lambda_2(s+\mu_1)(s+\hat{\lambda}), \\ W_4(s) &= \lambda_3(s+\mu_1)(s+\mu_2)(s+\hat{\lambda}), \\ W_5(s) &= s[\lambda_1\mu_1(s+\mu_2) + \lambda_2\mu_2(s+\mu_1)]. \end{aligned}$$

An important rate of the system described by the process X(t) is an average system 'life time'. Without determining the reverse transforms, which makes it possible to determine the probabilities $P_i(t)$, where i = 1, 2, 3, 4, 5, it is possible to determine the average values of the times to stay in certain states. It is known [1] that

$$E(T_1 + T_2 + T_3 + T_5) = \lim_{s\to 0^+}\left[\frac{1}{s} - \tilde{P}_4(s)\right], \tag{13}$$

where T_i means an average time to stay in state i, and:

$$\tilde{P}_4(s) = \frac{W_4(s)}{W(s)} = \frac{\lambda_3(s+\mu_1)(s+\mu_2)(s+\hat{\lambda})}{s\left[(s+\lambda)(s+\hat{\lambda})(s+\mu_1)(s+\mu_2) - \hat{\lambda}\left[\lambda_1\mu_1(s+\mu_2) + \lambda_2\mu_2(s+\mu_1)\right]\right]} \tag{14}$$

Let W(s) = sM(s), then:

$$\frac{1}{s} - \tilde{P}_4(s) = \frac{1}{s} - \frac{W_4(s)}{sM(s)} = \frac{M(s) - W_4(s)}{sM(s)}. \tag{15}$$

Having determined the form of M(s) and $W_4(s)$ we get:

$$M(0) = \hat{\lambda}\lambda_3\mu_1\mu_2, \tag{16}$$

$$W_4(0) = \hat{\lambda}\lambda_3\mu_1\mu_2. \tag{17}$$

Limit

$$\lim_{s\to 0^+} \frac{M(s) - W_4(s)}{sM(s)} \tag{18}$$

is the one of type [0/0], where M(s) is a multinomial of the forth degree related to s, and $W_4(s)$ is a multinomial of the third degree. With s for M(s) the coefficient equals

$$\lambda\hat{\lambda}\mu_1 + \lambda\hat{\lambda}\mu_2 + (\lambda + \hat{\lambda})\mu_1\mu_2 - \hat{\lambda}\lambda_1\mu_1 - \hat{\lambda}\lambda_2\mu_2, \tag{19}$$

and for $W_4(s)$

$$\lambda_3(\mu_1\mu_2 + \hat{\lambda}\mu_1 + \hat{\lambda}\mu_2). \tag{20}$$

Therefore it is concluded that limit

$$\lim_{s\to 0^+}\left[\frac{1}{s} - \tilde{P}_4(s)\right] = \frac{\mu_1\mu_2(\lambda + \hat{\lambda} - \lambda_3) + \hat{\lambda}\lambda_2\mu_1 + \hat{\lambda}\lambda_1\mu_2}{\hat{\lambda}\lambda_3\mu_1\mu_2} \tag{21}$$

It is convenient to present the average value $ET=ET_1 + ET_2 + ET_3 + ET_5$ as

$$ET = \frac{\lambda + \hat{\lambda} - \lambda_3}{\hat{\lambda}\lambda_3} + \frac{\lambda_2}{\lambda_3\mu_2} + \frac{\lambda_1}{\lambda_3\mu_1}. \tag{22}$$

The dependence of ET in the intensity value function $\hat{\lambda}$ (the value depends on the reserve object number) is shown in Fig.2.

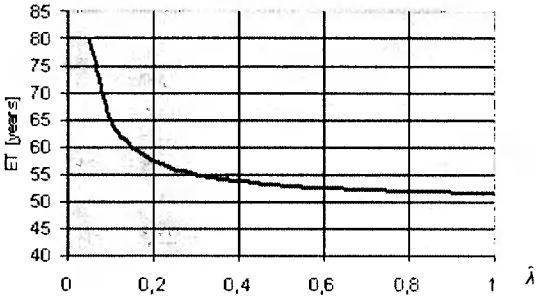

Fig.2. Dependence of average 'system life time' in the intensity function $\hat{\lambda}$, for constant values of the parameter $\lambda << \mu_2 < \mu_1$ equal to: $\lambda = 0.05$, $\mu_2 = 17.8$, $\mu_1 = 33.82$

CONCLUSIONS

The average system life time depends, in fact, on three parameters describing the system maintenance process model that is $\hat{\lambda}$, λ, λ_3. The relation between the average system life time and the value of parameter $\hat{\lambda}$ may be the basis to determine the required number of the reserve elements in order to achieve the average system life time required. Moreover, the analysis of the mv/lv distribution transformer maintenance process model presented in the paper may be generalized for more types of renovations.

REFERENCES

[1] Bobrowski D., 1985. Modele i metody matematyczne teorii niezawodności w przykładach i zadaniach. WNT Warszawa.
[2] Buslenko N., Kałasznikow W., Kowalenko I., 1979. Teoria systemów złożonych. PWN Warszawa.
[3] Sołowiew A.D., 1983. Analityczne metody w teorii niezawodności. WNT Warszawa.
[4] Perczyński D., 2000. Racjonalna gospodarka transformatorami. Minimalizacja potrzeb transformacji oraz kosztów eksploatacji transformatorów rozdzielczych. Wyd. Politechniki Poznańskiej Poznań.
[5] Perczyński D., Kolber P., 2001. Matematyczny model analizy niezawodności systemu wykonawczego transformującego energię elektryczną śN/nN. KONBIN'01, Szczyrk.
[6] Perczyński D., Knopik L., Landowski B., 2002. Prognozowanie stanu systemu eksploatacji transformatorów rozdzielczych na podstawie badań modelowych. Zagadnienia Eksploatacji Maszyn 3, 201-209.

Review by prof. Józef Żurek

ISBN 83-89334-82-8